University of California
Los Angeles

Planetesimals Around White Dwarfs

A dissertation submitted in partial satisfaction
of the requirements for the degree
Doctor of Philosophy in Astronomy

by

Siyi Xu

2014

© Copyright by
Siyi Xu
2014

Abstract of the Dissertation

Planetesimals Around White Dwarfs

by

Siyi Xu

Doctor of Philosophy in Astronomy

University of California, Los Angeles, 2014

Professor Michael A. Jura, Chair

Evidence is convincing that a big fraction of extrasolar planetesimals can survive the red giant stage of a star and persist into the white dwarf phase. We argue that eventually, some of them do get perturbed into the tidal radius of the white dwarf and disrupted, creating a dusk disk and polluting the star's pure hydrogen or helium atmosphere at the same time. I have been performing multi-wavelength observations to study these intriguing systems. With Spitzer/IRAC, I find a depletion of dust disk around cool white dwarfs relative to the warmer sample, possibly due to accretion from cometary objects. With the Cosmic Origins Spectrograph (COS) onboard the Hubble Space Telescope and the High-Resolution Echelle Spectrometer (HIRES) on Keck, I find that to zeroth order, the elemental compositions of extrasolar planetesimals very much resemble that of bulk Earth. A more detailed comparison with the solar system meteorites shows that post-nebular processing is common among extrasolar planetesimals. Overall, the bulk composition of Earth is normal compared to the current sample of extrasolar planetesimals.

The dissertation of Siyi Xu is approved.

Kevin D. McKeegan

Benjamin M. Zuckerman

Michael A. Jura, Committee Chair

University of California, Los Angeles

2014

To my parents.

Table of Contents

List of Figures

List of Tables

Acknowledgments

I remember vividly about five years ago, my friends warned me,"If you want to enjoy life, do not ever go to graduate school." I am glad that I did not listen to them, otherwise I probably would not be here. More importantly, that is when I started to realize that life is all about what you make out of it.

I grew up in Kunshan, a small town very close to Shanghai in China. If I had listened to everybody around me, I would never choose astronomy as my career path. I probably would go to business school or computer science instead, which seem to be popular majors everywhere in the globe. I am very grateful for my parents for their unconditional love and support. Unlike most Asian parents who tend to order their kids around, they gave me a lot of freedom and taught me to be responsible for my own decisions.

Coming to UCLA for graduate school was one of the hardest choices for me but it is also one of the best decisions in my life. Not only because Los Angeles is such an interesting place with a diverse culture. It is never hard to find authentic Chinese food; there are numerous restaurants with good happy hour menu in Westwood; literally, I can go skiing and surfing in the same day. It is also about all the awesome people I meet along the way. Astronomy is a small division along with physics but together we are like a big family.

I am most grateful for my thesis advisor, Mike Jura. He is a great scientist and an inspiring teacher. Everyday is a brand new adventure and there are always cool things happening in the universe, waiting to be discovered. His wisdom has taught me to think like a scientist and also shaped my way of viewing the world. I remember one time, I made a very dumb mistake. We ended up losing some precious observing time on the Keck telescope. I was very upset. But Mike said to me, "The only person that makes no mistakes is a dead person". Soon I became cheerful again. I feel extremely lucky to be in the right place at the right time working with the right professor to have access to all worlds' best telescopes and looking at part of the sky nobody has ever seen before.

I have gained tremendous knowledge through the collaboration at UCLA. I thank Professor Ben Zuckerman for teaching me how to think outside of box. I appreciate learning from Beth Klein about data reduction and critical thinking. I acknowledge Detlev Koester (University of Kiel) for computing white dwarf spectra and patiently explaining the model.

I also want to thank all my friends at UCLA, particularly Julia Fang, Fred Davies, Zhiyuan Li, Alexis Popkow, David Rodriguez, Greg Mace, Betsy Mills, Eric Takasugi, Jing Li, Xuan Ji, Tracy Zhang, Muhuan Huang, Nate Ross, Kathy Kornei, Richael Smith, and Sylvana Yelda. Also thanks to all friends at China, especially Qingzhu Shi.

Chapter 2 is a version of Xu & Jura (2012) and is reproduced by permission of AAS. I thank Jay Farihi for useful email exchanges on Spitzer data reduction, Huan Meng and David Rodriguez for helpful suggestions and discussions.

Chapter 3 is a version of Xu et al. (2013a) and is reproduced by permission of AAS.

Chapter 4 is a version of Xu et al. (2014) and is reproduced by permission of AAS. I thank Greg Mace for helping with the NIRSPEC observing run and useful discussions about data reduction procedures, Carl Melis for helping with HIRES observing runs in 2008, and Brad Holden for useful email exchanges regarding the MAKEE software.

Chapter 5 is a version of Xu et al. (2013b) and is reproduced by permission of AAS. Some of the data presented herein were obtained at the W.M. Keck Observatory, which is operated as a scientific partnership among the California Institute of Technology, the University of California and the National Aeronautics and Space Administration. The Observatory was made possible by the generous financial support of the W.M. Keck Foundation. We recognize and acknowledge the very significant cultural role and reverence that the summit of Mauna Kea has always had within the indigenous Hawaiian community. We are most fortunate to have the opportunity to conduct observations from this mountain.

This work was supported by grants from the NSF and NASA to UCLA.

Vita

2010 B.S. (Astronomy), Nanjing University, China.

2012 M.S. (Astronomy), University of California, Los Angeles.

Publications

Xu, S., Jura, M., Koester, B., Klein, B., & Zuckerman, B., *Elemental Compositions of Two Extrasolar Rocky Planetesimals*, 2014, ApJ, 783, 79

Jura, M., Xu, S., & Young, E. D., ^{26}*Al in the Early Solar System: Not so Unusual After All*, 2013, ApJ, 755, L41

Xu, S., Jura, M., Klein, B., Koester B., & Zuckerman, B., *Two Beyond-Primitive Extrasolar Planetesimals*, 2013, ApJ, 766, 132

Jura, M., Xu, S., Koester, B., Klein, B., & Zuckerman, B., *Discovery of Molecular Hydrogen in White Dwarf Atmospheres*, 2013, ApJ, 766, L18

Zuckerman B., Xu, S., Klein, B., & Jura, M, *The Hyades Cluster: Identification of a Planetary System and Escaping White Dwarfs*, 2013, ApJ, 770, 140

Jura, M., & Xu, S., *Extrasolar Refractory-Dominated Planetesimals: an Assessment*, 2013, AJ, 145, 30

Xu, S., Jura, M., B., Klein, Koester, B., & Zuckerman, B., *Two Extrasolar Asteroids with Low Volatile-element Mass Fractions*, 2012, ApJ, 750, 69

Jura, M., & Xu, S., *Water Fractions in Extrasolar Planetesimals*, 2012, AJ, 143, 6

Xu, S. & Jura, M., *Spitzer Observations of White Dwarfs: the Missing Planetary Debris Around DZ stars*, 2012, ApJ, 175, 88

Jura, M., & Xu, S., *The Survival of Water within Extrasolar Minor Planets*, 2010, AJ, 140, 1129

CHAPTER 1

Introduction

"The earth is a very small stage in a vast cosmic arena" as Carl Sagan puts it. The question of *who we are* and *where we come from* has been the central of interest since the beginning of mankind. We live in a great era that enables us to explore answers to these unknowns; there are unprecedented missions (e.g. Curiosity, Messenger, Cassini) to study planets in the Solar system as well as ground and space based telescopes (e.g. Keck, Hubble, Spitzer) to study planets in the cosmos – extrasolar planets. These ultimate questions can only be answered by finding clues in both our own solar system and extrasolar planetary systems. My way of tackling this program is to follow the chemical elements in extrasolar environments and compare with their distributions in the solar system.

When observed with the Keck Telescope, 25% single white dwarfs are found to be polluted – their atmospheres display absorption lines from elements heavier than He in addition to the usual H and/or He lines (Zuckerman et al., 2010). These heavy elements must come from recent events because their settling times in a white dwarf's atmosphere are much shorter than a WD's cooling age. The consensus is that the source of pollution is accretion from tidally disrupted extrasolar planetesimals with masses comparable to that of a solar system asteroid (Jura, 2003). Now we have a powerful method to uniquely measure the bulk compositions of extrasolar planetesimals, untouchable by any other techniques (Jura & Young, 2014). For the most heavily polluted WDs, there is often excess infrared radiation coming from the orbiting dust disk of these pulverized planetesimals.

I have been performing multi-wavelength observations to study extrasolar planetesimals around white dwarfs – in the form of atmospheric pollution and orbiting dust disks. Spectroscopic study of polluted WDs directly measures the bulk elemental compositions of extrasolar

planetesimals. Infrared study probes the dust disks prior to accretion onto the central WD and constrain the evolution of extrasolar planetesimals during the WD stage. This thesis is a compilation of four chapters, each from a published paper. A brief summary is provided for each chapter in the following.

Chapter 2 is the results from a Spitzer/IRAC search for infrared excesses around white dwarfs, including 14 newly-observed targets and 16 unpublished archived stars. We find a substantial infrared excess around two warm white dwarfs – J220934.84+122336.5 and WD 0843+516, the latter apparently being the hottest white dwarf known to display a close-in dust disk. Extending previous studies, we find that the fraction of white dwarfs with dust disks increases as the star's temperature increases; for stars cooler than 10,000 K, even the most heavily polluted ones do not have $\sim$1000 K dust. There is tentative evidence that the dust disk occurrence is correlated with the volatility of the accreted material. In the Appendix, we modify a previous analysis to show that Poynting-Robertson drag might play an important role in transferring materials from a dust disk into a white dwarf's atmosphere.

Chapter 3 is about HST/COS studies of GD 362 and PG 1225-079, two helium-dominated, externally-polluted white dwarfs. We determined or placed useful upper limits on the abundances of two key volatile elements, carbon and sulfur, in both stars; we also constrained the zinc abundance in PG 1225-079. In combination with previous optical data, we find strong evidence that each of these two white dwarfs has accreted a parent body that has evolved beyond primitive nebular condensation. The planetesimal accreted onto GD 362 had a bulk composition roughly similar to that of a mesosiderite meteorite based on a reduced chi-squared comparison with solar system objects; however, additional material is required to fully reproduce the observed mid-infrared spectrum for GD 362. No single meteorite can reproduce the unique abundance pattern observed in PG 1225-079; the best fit model requires a blend of ureilite and mesosiderite material. From a compiled sample of 9 well-studied polluted white dwarfs, we find evidence for both primitive planetesimals, which are a direct product from nebular condensation, as well as beyond-primitive planetesimals, whose final compositions were mainly determined by post-nebular processing.

Chapter 4 is about Keck/HIRES and HST/COS spectroscopic studies of extrasolar rocky

planetesimals accreted onto two hydrogen atmosphere white dwarfs, G29-38 and GD 133. In G29-38, 8 elements are detected, including C, O, Mg, Si, Ca, Ti, Cr and Fe while in GD 133, O, Si, Ca and marginally Mg are seen. These two extrasolar planetesimals show a pattern of refractory enhancement and volatile depletion. For G29-38, the observed composition can be best interpreted as a blend of a chondritic object with some refractory-rich material, a result from post-nebular processing. Water is very depleted in the parent body accreted onto G29-38, based on the derived oxygen abundance. The inferred total mass accretion rate in GD 133 is the lowest of all known dusty white dwarfs, possibly due to non-steady state accretion. We continue to find that a variety of extrasolar planetesimals all resemble to zeroth order the elemental composition of bulk Earth.

Chapter 5 is an unexpected discovery that comes with our COS observations of G29-38 and GD 133, as described in Chapter 4. We have detected molecular hydrogen in the atmospheres of three white dwarfs with effective temperatures below 14,000 K, G29-38, GD 133 and GD 31. This discovery provides new independent constraints on the stellar temperature and surface gravity of white dwarfs.

CHAPTER 2

Spitzer Observations of White Dwarfs: the Missing Planetary Debris Around DZ Stars

Reproduced by permission of the AAS (Xu, S., & Jura, M., 2012, Astrophysical Journal, 175, 88).

2.1 Introduction

White dwarfs are the final evolutionary stage of stars with masses less than about eight solar masses. The first infrared excess around a white dwarf was discovered more than 20 years ago (Zuckerman & Becklin, 1987). Since 2005, primarily thanks to the Spitzer Space Telescope (Werner et al., 2004), progress has been dramatic. Including WD 0843+516[1] and J220934.84+122336.5 (hereafter J2209+1223), which are reported in this paper, there are 23 confirmed white dwarfs with a warm disk and 5 additional candidates (see our Table 2.1, an extension of Table 1 in Farihi et al. (2009)). Recently, observations from the WISE mission (Debes et al., 2011) and the UKIRT Infrared Deep Sky Survey (UKISS) (Steele et al., 2011; Girven et al., 2011) are also contributing to the disk studies.

There are three classes of dust disks detected around a white dwarf: (1) $\sim$100 K dust, which is found around $\gtrsim$ 15% pre-white dwarfs and white dwarfs, sometimes in the center of a planetary nebulae (Chu et al., 2011). The source of the dust is believed to be the collisions among analogs to Kuiper-belt objects in the system (Bonsor & Wyatt, 2010; Dong et al., 2010). (2) $\sim$500 K dust around two cool stars, G 166-58 (T_*=7,400 K) (Farihi et al., 2008b)

[1]After reading a short description on astro-ph of a survey on dust disks around white dwarfs (Chu et al., 2010), we learned from Y.-H. Chu that their team has independently found the infrared excess for this star.

and PG 1225-079 (T_*=10,600 K) (Farihi et al., 2010b). A model that reproduces these data invokes emission from an opaque dust ring with a large, dust-free inner hole and an outer boundary within the tidal radius of the white dwarf. However, there are only two dust rings in this class and their origin is uncertain. (3) ∼1000 K dust, which is found in the remaining 21 white dwarfs listed in Table 2.1. In these systems, all the dust lies within the star's tidal radius and the inner boundary is determined by the location where the refractories rapidly sublimate. The excess can be fit with a flat opaque dust disk (Jura, 2003). The excesses from 1000 K dust are substantial at wavelengths greater than 3 μm and can be easily studied with warm Spitzer; we focus on discussing this class of disk in this paper[2].

Gravitational settling of heavy elements is usually so effective in white dwarfs cooler than 25,000 K that their atmospheres are typically pure hydrogen or pure helium (Koester, 2009). However, about 25% of DAs (white dwarfs with hydrogen dominated atmosphere) and 33% of DBs (white dwarfs with helium dominated atmosphere) have atmospheric pollution (Zuckerman et al., 2003, 2010). Given that the diffusion timescale of heavy elements is orders of magnitude less than a white dwarf's cooling age (Koester, 2009), it is unlikely that those heavy elements are intrinsic. Theoretical calculations show that tidal disruption and subsequent accretion of small bodies in the planetary system can explain the source of pollution in these objects (Debes & Sigurdsson, 2002; Jura, 2003; Bonsor et al., 2011). Kilic et al. (2006) first showed a correlation between the presence of an orbiting dust disk and a high level of heavy element pollution in the star's photosphere. Subsequent observations have confirmed this trend and supported the small body accretion model (Jura et al., 2007a; Farihi et al., 2008a,b, 2009, 2010b). Thus studying polluted white dwarfs provides invaluable measures of the bulk composition of extrasolar minor planets (see, for example, Klein et al. (2010)).

However, as can be seen in our Table 2.1 and in Farihi et al. (2009), almost all the disk-host stars have effective temperatures of at least 9,500 K. Here, we report the results from a warm Spitzer Cycle 7 program, searching for infrared excesses around polluted cool white

[2]In the following sections, unless specifically stated, dust disk and infrared excess all refer to this 1000 K dust.

dwarfs and a few highly-polluted warmer targets. Additionally, we reduced some unpublished archived Spitzer data.

Target selections and observations are presented in section 2. In section 3, we describe data reduction procedures and SED fits to the data. In section 4, the main result is discussed: we continue to find dust disks around warm polluted white dwarfs but no dust around highly polluted cool stars. In section 5, we explore the possible correlations between the presence of a dust disk and other characteristics of the star in addition to its temperature. Possible scenarios that can account for the presence of heavy elements without producing a dust disk are discussed in section 6. Conclusions are presented in section 7. In the Appendix, we assess the importance of Poynting-Robertson (P-R) drag on the entire dust disk as a mechanism to transfer material from the disk into the white dwarf's atmosphere.

2.2 Observations

2.2.1 Source Selection

The 14 targets of our Cycle 7 program are listed in Table 2.2. 10 stars are newly identified DZs[3] with distinctively large amount of atmospheric calcium detected in the SDSS spectrum; they all have $T_* < 10{,}000$ K and m(z) < 18.0 mag (0.23 mJy) (Dufour et al., 2006, 2007). 4 additional DBZs[4] with $T_* \sim 15{,}000$ K are also included: 3 stars from Eisenstein et al. (2006) plus G 241-6, which was recognized recently to be a near-twin of GD 40, a highly polluted white dwarf with a dust disk (Zuckerman et al., 2010; Klein et al., 2010).

For the completeness of the sample, we also report IRAC 3.6 μm – 7.9 μm fluxes for 16 single DA white dwarfs from the unpublished archived Cycle 3 program 30856. These stars all have well determined temperatures, surface gravities as well as highly accurate SDSS photometry, which is crucial in determining the presence of a disk. Relevant parameters are listed in Table 2.3.

[3]DZs are cool white dwarfs that display trace elements other than carbon; it is thought that DZs have a helium dominated atmosphere, but the gas is too cool for the helium lines to be detected.

[4]DBZs are DBs with detected heavy elements in the atmosphere.

Table 2.1. Warm Dust Disks and Candidates Discovered Since 2010

WD	Name	SpT	T_* (K)	V (mag)	Discovery Year	Discovery Telescope	Ref
0106-328	HE 0106-3253	DAZ	15,700	15.50	2010	Spitzer	1
0307+077	HS 0307+0746	DAZ	10,200	16.40	2010	Spitzer	1
0435+410	GD 61	DBZ	17,280	14.80	2011	Spitzer	2
	J0738+1835	DBZ	13,600	17.82[d]	2010	Germini/NIRI	3
0843+516	PG 0843+517	DA	23,900	16.15	2011	Spitzer	4
1225-079[a]	PG 1225-079	DZAB	10,500	14.80	2010	Spitzer	1
	J2209+1223	DBZ	17,300	17.43[d]	2011	Spitzer	4
	GALEX J1931+0117	DAZ	20,890[b]	14.20	2011	WISE	5
2221-165	HE 2221-1630	DAZ	10,100	16.10	2010	Spitzer	1
	SDSS 0753+2447[c]	DA	13,400	19.21[d]	2011	UKIRT	6, 7
	SDSS 0959-0200[c]	DA	12,000	18.34[d]	2011	UKIRT	6
	SDSS 1221+1245[c]	DA	12,000	18.39[d]	2011	UKIRT	6
1318+005	J1320+0018[c]	DA	19,600	17.30	2011	UKIRT	7
	J1557+0916[c]	DA	22,000	18.17[d]	2011	UKIRT	7

[a] WD 1225-079 is reported in Farihi et al. (2010b) to have a 4σ excess in the IRAC 7.9 μm band.

[b]Melis et al. (2011) derived a stellar temperature of 23,470 K for this star.

[c] These are debris disk candidates that needs to be confirmed with more infrared data as the UKIRT observation only extends to the K band.

[d]This is SDSS r magnitude.

Note. — This table is supplementary to Table 1 in Farihi et al. (2009), which lists 14 white dwarfs with an infrared excess discovered at that time.

Note. — GD 303, which might have a marginal excess at 2σ level at the IRAC 4 band (Farihi et al., 2010b), is excluded from this table.

References. — (1) Farihi et al. (2010b); (2) Farihi et al. (2011); (3) Dufour et al. (2010); (4) This work; (5) Debes et al. (2011); (6) Girven et al. (2011). (7) Steele et al. (2011);

Table 2.2. Cycle 7 White Dwarf Targets

WD	Name	T_* (K)	SDSS z (mag)	[Ca]/[He][a]	Ref
0033-114	J003601.37-111213.8	7,280	17.18	-9.26	1
0216-095	J021836.69-091944.8	9,560	17.84	-10.63	1
0936+560	J093942.29+555048.7	8,680[b]	17.18	-8.51	1
	J095119.85+403322.4	8,370	17.75	-10.27	1
1035-003	J103809.19-003622.5	8,200[c]	17.30	-7.70	2
1212-023	J121456.39-023402.8	6,000	17.50	···	3
1244+498	J124703.28+493423.6	16,800	17.21	···	4
	J125752.77+425255.1	16,800	17.94	···	4
	J130905.26+491359.7	8,620	17.67	-10.16	1
	G 199-63	8,900	17.15	-9.39	1
	LP 219-80	6,770	16.91	-11.35	1
	J220934.84+122336.5	17,300	17.91	-6.16[d]	4
	J222802.05+120733.3	6,760	16.36	-9.96	1
2222+683	G 241-6	15,300	16.07	-7.25	5

[a] Abundances are expressed as [X]/[Y] = log [n(X)/n(Y)]; n(X) is the number abundance.

[b]This star is reported to be 11,500 K in Kilic et al. (2008a).

[c]This star is reported to be 6,770 K and [Ca]/[He]= -9.44 in Dufour et al. (2007).

[d]This value is derived from measuring the equivalent width of Ca II 3933.7Å from the SDSS spectra and extrapolate from GD 61, a heavily polluted white dwarf with similar effective temperature and surface gravity.

References. — (1) Dufour et al. (2007); (2) Koester et al. (2011); (3) Reid et al. (2001); (4) Eisenstein et al. (2006); (5) Zuckerman et al. (2010).

Table 2.3. Archived White Dwarf Targets

WD	T_{eff} (K)	SDSS z (mag)	Ref
0816+297	16,700	16.53	1
0819+363	18,700	16.38	1
0843+516	23,900	16.86	1
0937+505	35,900	16.86	1
1017+125	21,400	16.55	2
1109+244	37,800	16.64	3
1120+439	27,200	16.28	3
1133+293	23,000	15.69	3
1214+267	65,700	16.54	3
1216+036	14,400	16.66	2
1257+032	17,600	16.39	2
1507+021	20,200	17.23	2
1553+353	25,600	15.59	3
1559+128	29,200	17.74	3
1620+513	20,900	16.61	1
2120+054	36,200	16.93	1

References. — (1) Holberg & Bergeron (2006); (2) Koester et al. (2009); (3) Liebert et al. (2005);

2.2.2 Observing Strategies

Spitzer has been operated in the warm phase mission since the depletion of cryogen in May, 2009. The two shortest wavelength channels (3.6 μm and 4.5 μm) of the IRAC (Fazio et al., 2004) continue to function and were used in this study to obtain broadband images. The observations were performed by using a 30 sec frame time with 30 medium size dithers in the cycling pattern, resulting in a 900 sec total exposure time in each IRAC channel.

The archived data were obtained between 2006 and 2007. The observing mode was random 9-point large dithering with a frame time of 30 sec, resulting in a total of 270 sec in each IRAC channel.

2.3 Data Analysis

2.3.1 Data Reduction and SED Fits

Following the data reduction procedures described in Farihi et al. (2008a,b, 2009), each exposure was processed with MOPEX (version 18.4.9) to create a single mosaic with a pixel size of $0\farcs6$. Though the intrinsic plate scale is $1\farcs2$ pixel^{-1}, a $0\farcs6$ pixel^{-1} mosaic was used because it has a better spatial resolution and the 3.6 μm and 4.5 μm images are oversampled. Aperture photometry was performed on the combined mosaic using both: (i) the standard IRAF apphot task, and (ii) the Astronomical Point source EXtractor (APEX) in MOPEX. We tried an aperture size of both 2 ($2\farcs4$) and 3 ($3\farcs6$) native pixels with a sky annulus of an inner radius of 5 native pixels ($6\farcs0$) and an outer radius of 15 native pixels ($18\farcs0$). We found that in some cases even in a clean field, the measured flux in these two aperture sizes can differ up to 5% and we report the average flux weighted by their SNR. To derive the aperture correction factor, we performed aperture photometry in the point response function (PRF) images in each band with our set of parameters. The PRF is the convolution of the point response function (PSF) of the telescope and the pixel response function of the detector and it is provided by the Spitzer Science Center. There are three factors contributing to the total uncertainty: 5% calibration uncertainty, which is based on previous studies of white dwarfs

Table 2.4. IRAC Fluxes for Cycle 7 Targets

Name	$F_{3.6\mu m}$ μJy	$F_{4.5\mu m}$ μJy
WD 0033-114	61±4	41±3
WD 0216-095	28±2	17±2
WD 0936+560	60±4	37±3
J0951+4033	34±3	22±2
WD 1035-003	53±3	36±3
WD 1212-023	85±5	60±4
WD 1244+498	38±3	23±2
J1257+4252	19±2	13±2
J1309+4913	38±3	24±2
G 199-63	57±4	37±3
LP 219-80	104±7	71±5
J2209+1223	88±5	86±5
J2228+1207	156±9	104±6
WD 2222+683	95±5	64±4

(Farihi et al., 2008a), rather than the 2-3% value optimally derived for other targets (Reach et al., 2005; Bohlin et al., 2011), measurement error and uncertainties caused by the choice of aperture radius; these uncertantities were all added in quadrature. The fluxes independently obtained by IRAF and APEX agree to within 3%. To be conservative, we report the values that have the larger measurement error in Table 2.4 and Table 2.5.

When there is a background source, proper motion analysis is performed to accurately determine the position of the target, followed by PRF fitting to obtain the true flux of the star. A residual mosaic, which subtracted the detected point source from the original mosaic, was produced. To check the result of PRF fitting, aperture photometry was re-performed at the same location of the target in the residual image. A good fit is achieved if the flux level in the aperture is comparable to the sky level, which is a few percent of the flux of the source. Examples of PRF fitting and the residual image are shown in Figure 2.1 and Figure 2.2.

For some archived stars, the background is very noisy in the 5.7 μm and 7.9 μm band.

Table 2.5. IRAC Fluxes for Archived DAs

WD	$F_{3.6\mu m}$ μJy	$F_{4.5\mu m}$ μJy	$F_{5.7\mu m}$ μJy	$F_{7.9\mu m}$ μJy
0816+297	76±5	51±4	28[a]	25[a]
0819+363	97±5	50±3	66±8	55±10
0843+516	140±12	134±9	98±10	154±13
0937+505	43±3	27±3	22±7	27[a]
1017+125	71±6	47±6	35[a]	24[a]
1109+244	57±5	36±4	37[a]	29[a]
1120+439	83±5	47±4	65±11	54[a]
1133+293	147±9	90±6	61±13	53±16
1214+267	54±4	35±3	32[a]	19[a]
1216+036	74±4	45±3	34[a]	36[a]
1257+032	85±5	51±4	34±11	33[a]
1507+021	40±3	25±3	32[a]	26[a]
1553+353	167±9	102±6	60±7	38±9
1559+128	21±2	12±2	38[a]	21[a]
1620+513	69±4	43±3	23[a]	26[a]
2120+054	45±3	27±3	39[a]	23[a]

[a] 3σ upper limit.

Note. — The WISE photometry for WD 0819+363 and WD 1559+128 might be somewhat misleading as the IRAC images show a background source within 5.″0, which cannot be resolved by WISE and its measurement indicates a substantial infrared excess for these two stars. Confusion is also likely to be a problem for GALEX 1931+0117, Melis et al. (2011) found a significantly lower L-band flux with ground based photometry than Debes et al. (2011) did by using WISE.

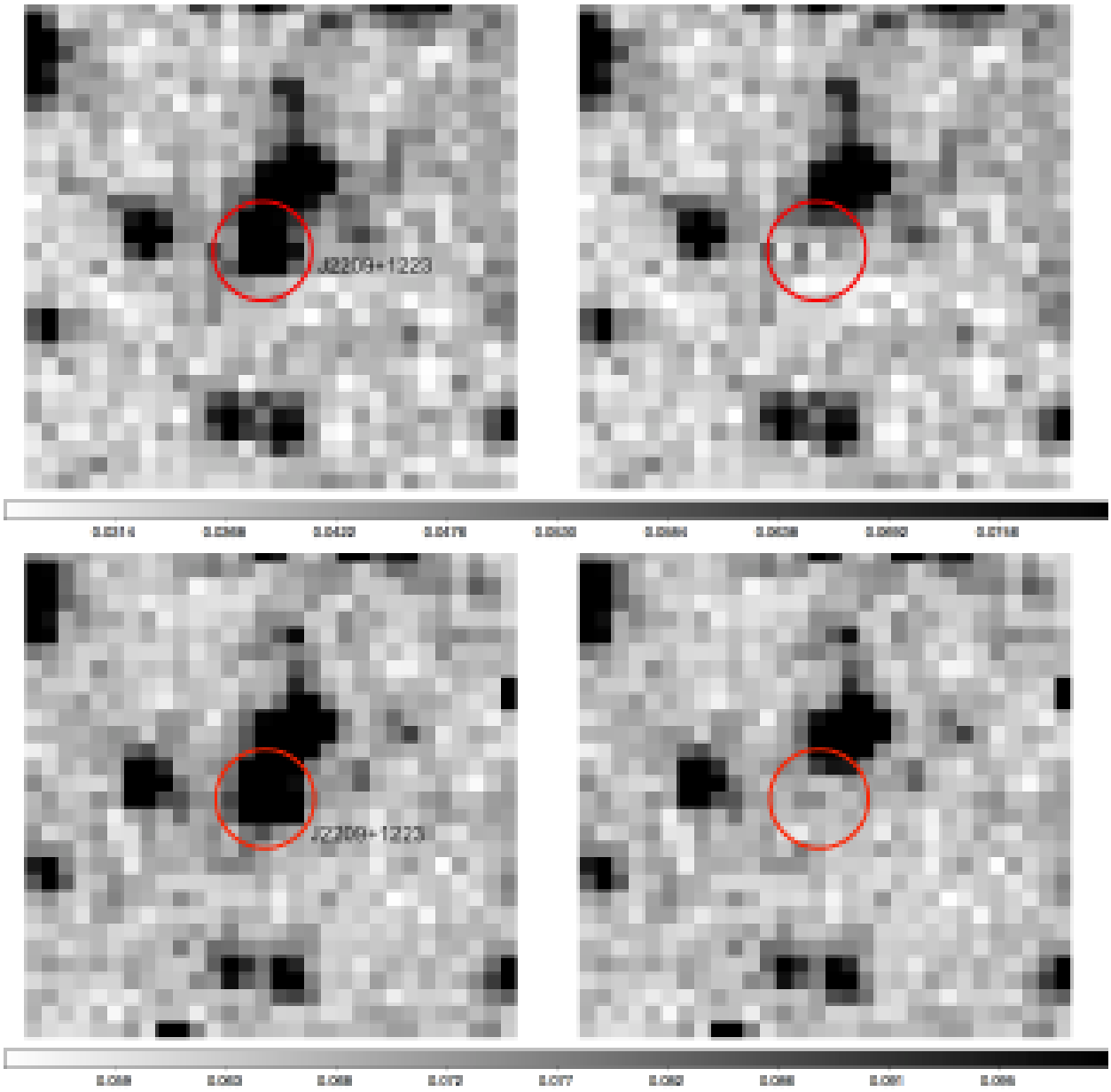

Figure 2.1 IRAC mosaics of J2209+1223 in 3.6 μm (the upper panel) and 4.5 μm band (the lower panel) in the plate scale of $1\farcs2$ pixel^{-1}; the left columns are the original data and the right columns are the residue after PRF fitting and the white dwarf is subtracted. North is up and East is left; the field of view is $36\farcs0$ by $36\farcs0$. The red circle is centered on J2209+1223 with a radius of 3 pixels and the nearby star is $6\farcs2$ away at position angle 333°.

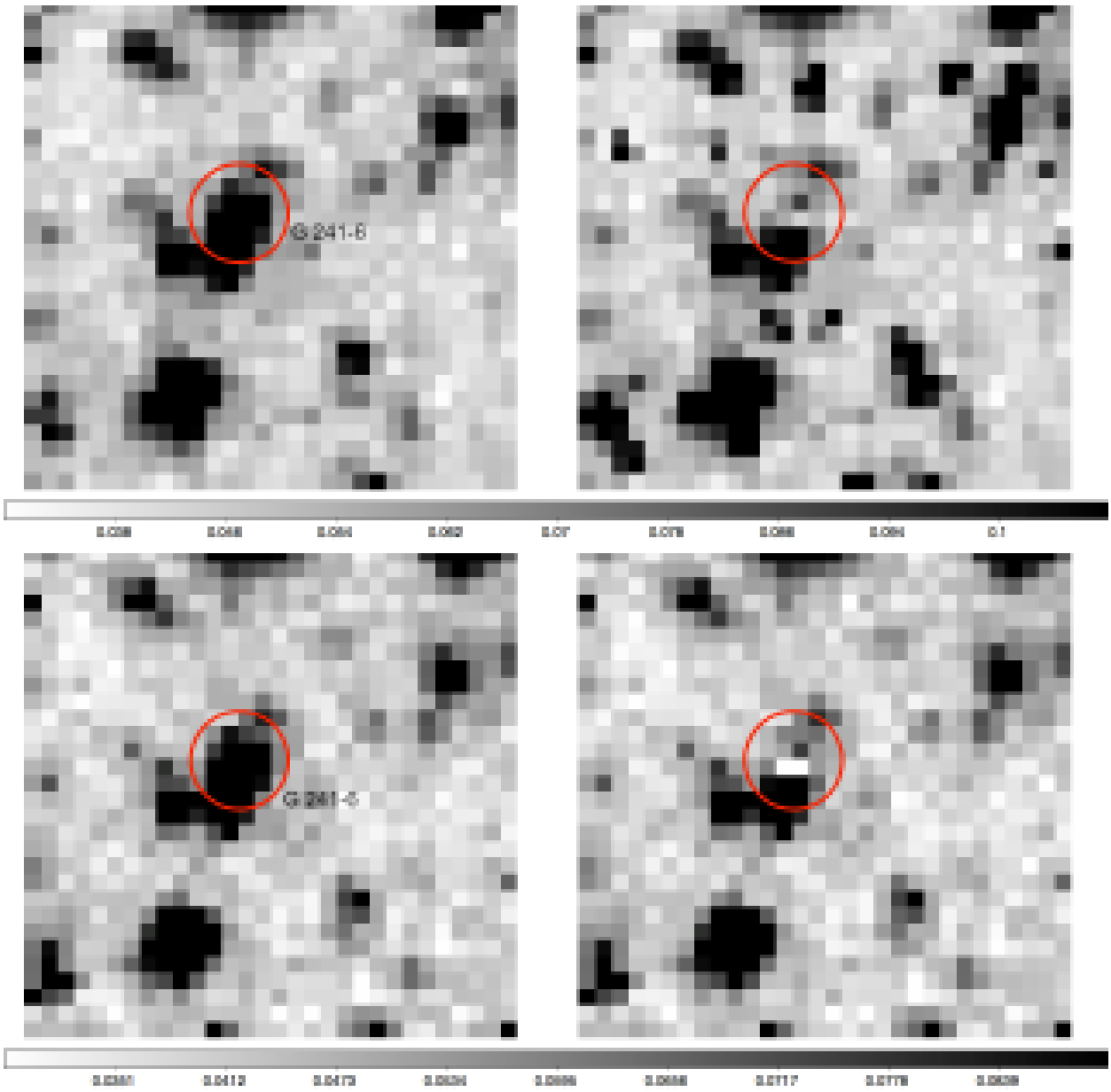

Figure 2.2 The same as Figure 2.1 except for G 241-6. We see this is a very complicated field and G 241-6 is heavily blended with an object with an angular separation of only 2.″3 at position angle 170° and another galaxy, J222334.23+683723.8 with a separation of 5.″5 and position angle 110°.

We report a positive detection when the measured flux is at least 3σ. To measure the upper limit, aperture photometry was performed in 20 empty background regions around the source with an aperture size of 2 native pixels. Then the standard deviation of these fluxes is taken to equal 1σ.

The Spectral Energy Distribution (SED) of all the targets are plotted in Figures 2.3 – 2.10. Also included in the SEDs are ugriz fluxes from the SDSS, JHK fluxes from the Two Micron All Sky Survey (2MASS) and WISE fluxes when the data are available. Ultraviolet fluxes from the Galaxy Evolution Explorer (GALEX) (Martin et al., 2005) are usually excluded because they can be strongly suppressed due to heavy element blanketing (Koester et al., 2011) or interstellar extinction. A blackbody model is then adopted to fit the star's photospheric flux, with most weight given to the SDSS photometry because the 2MASS fluxes have larger uncertainties. Though the blackbody temperature does not always agree with the reported white dwarf temperature of Dufour et al. (2007), this method is sufficient to identify infrared excess that is 10% above the photospheric value. When there is a detected excess, a thin, opaque, passive dusty disk is used to fit the SED (Jura, 2003).

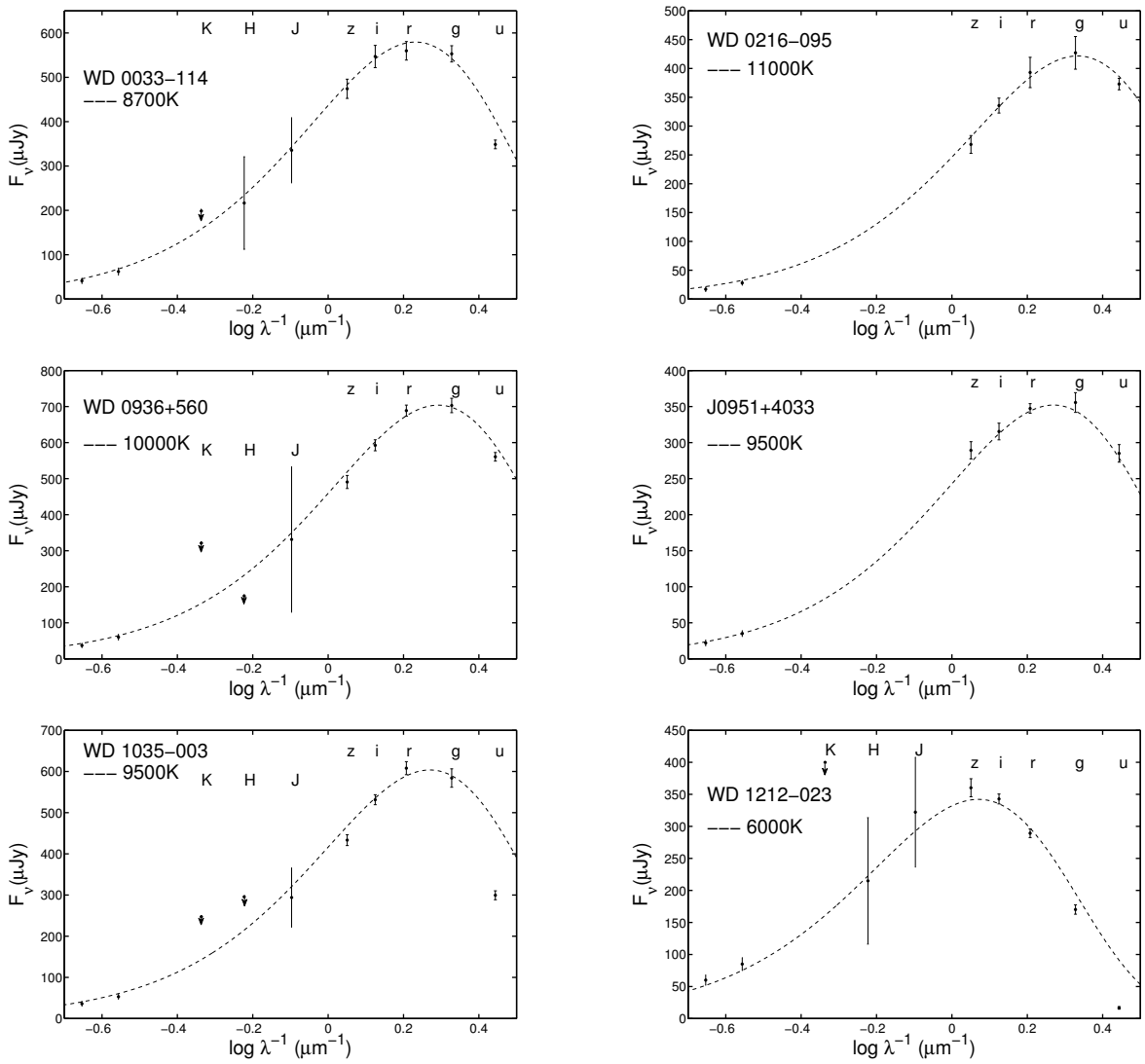

Figure 2.3 SEDs for Cycle 7 targets, including data from SDSS, 2MASS and IRAC with 2σ error bars. The dashed line is a simple blackbody fit to the photospheric flux.

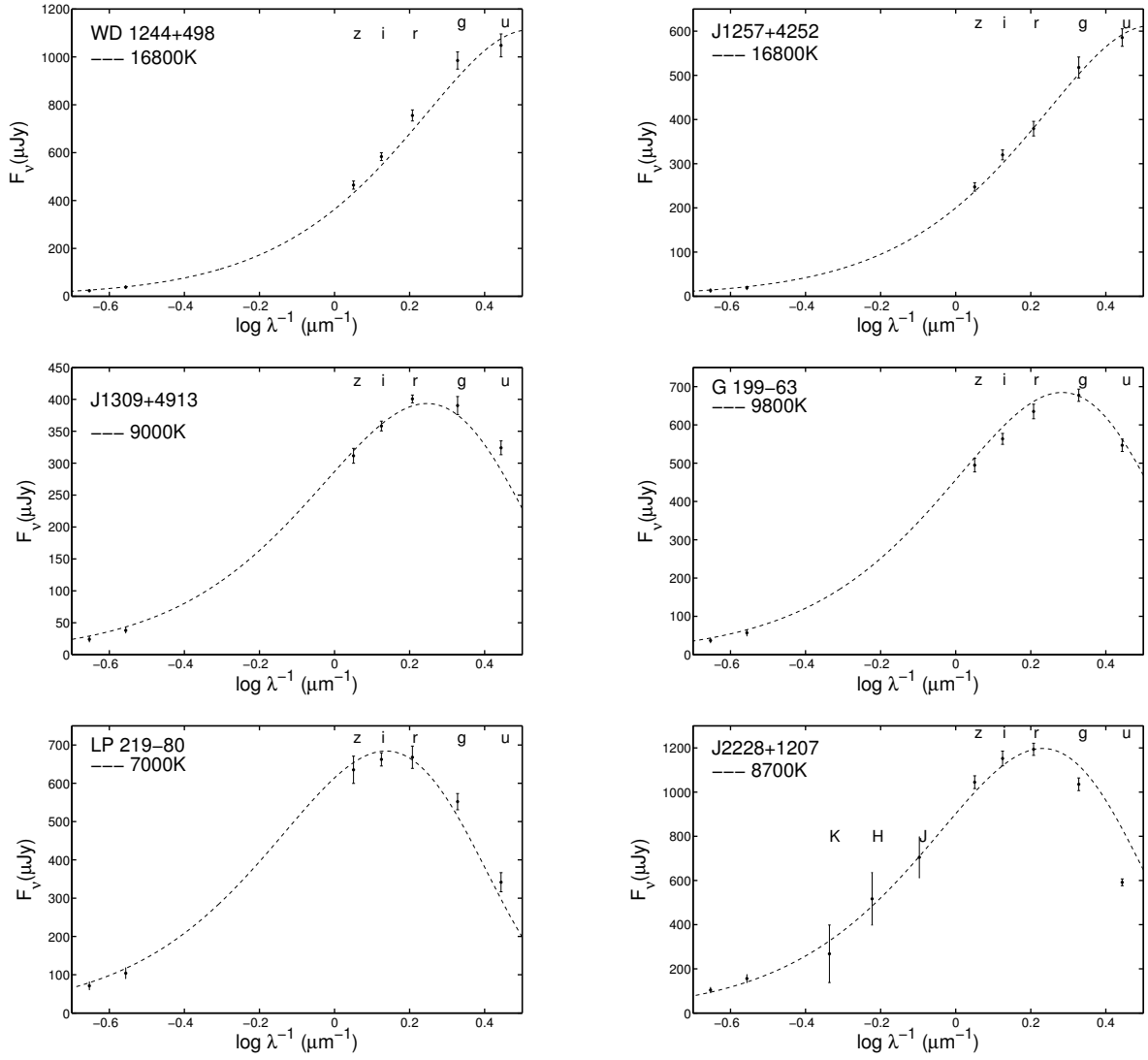

Figure 2.4 The same as Figure 2.3.

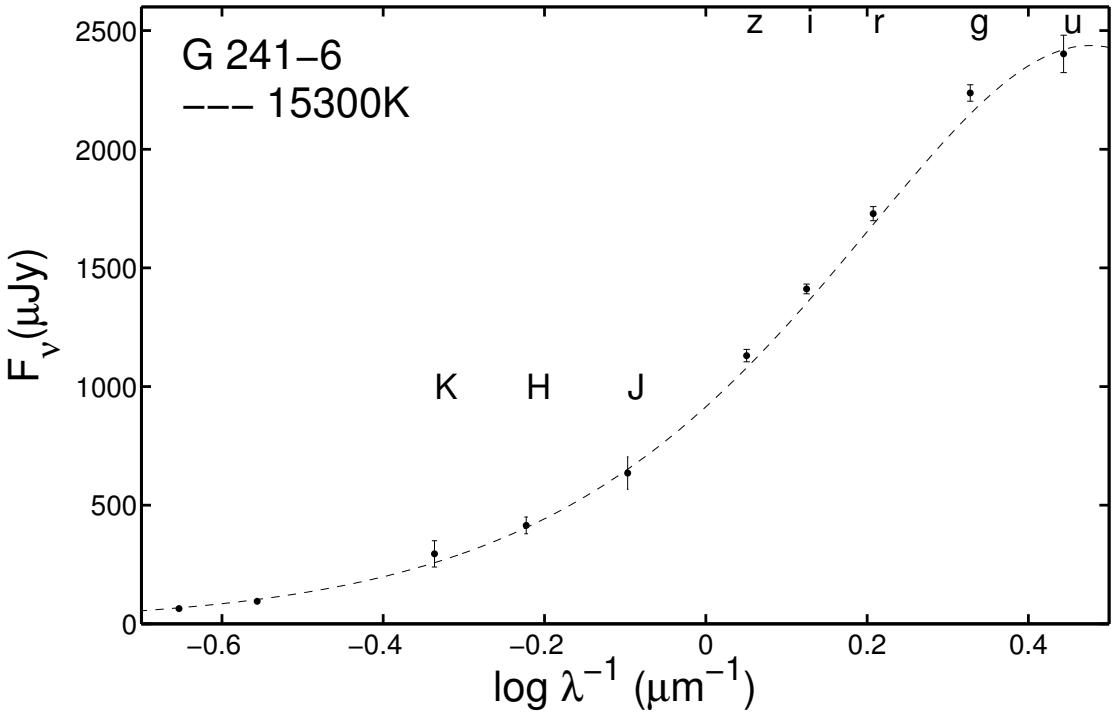

Figure 2.5 The same as Figure 2.3 except for G 241-6.

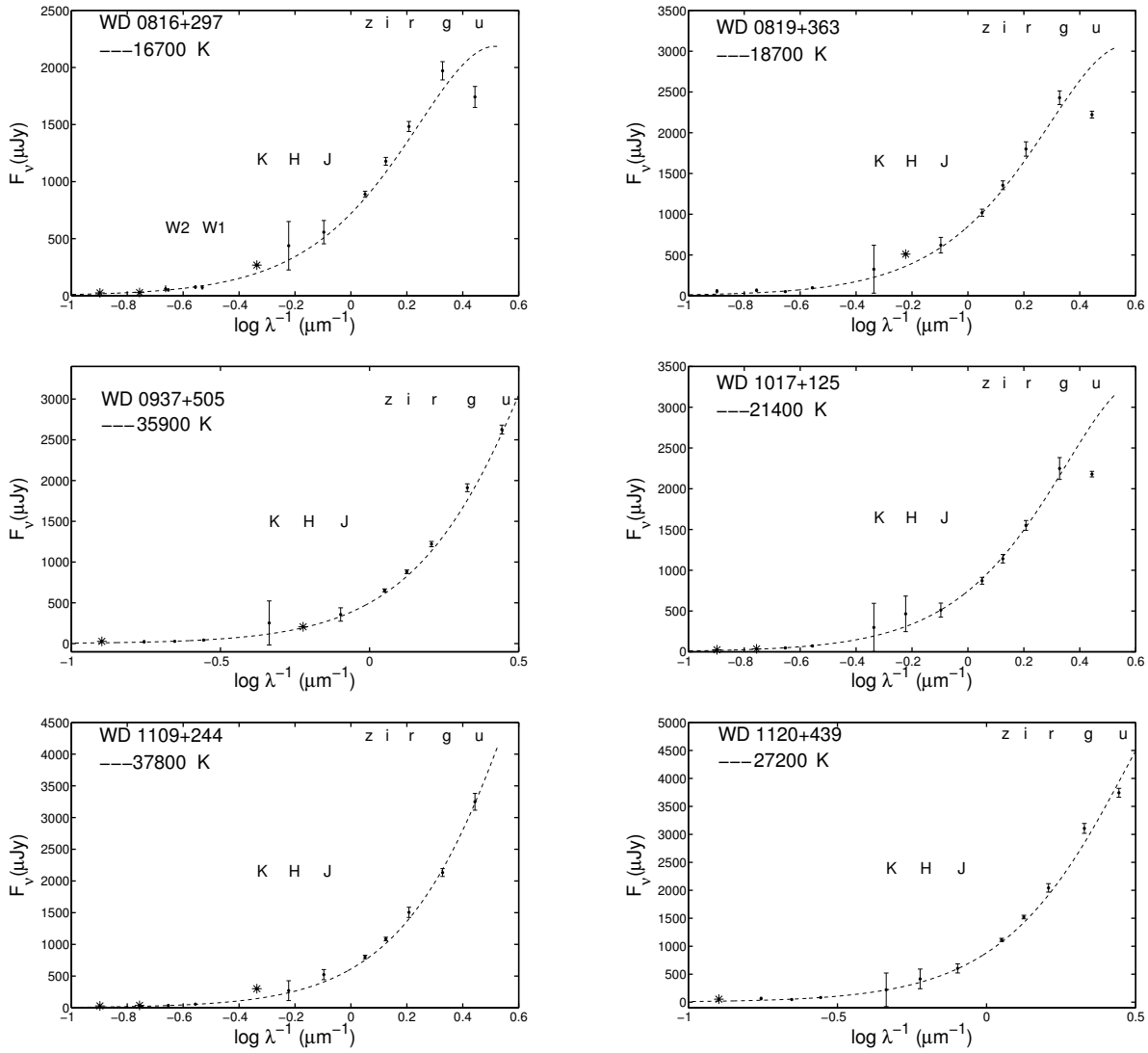

Figure 2.6 SED for archived targets, including data from SDSS, 2MASS, IRAC and WISE data when available with 2σ error bars. The asterisks denote upper limit. The dashed line is a simple blackbody fit to the photospheric flux.

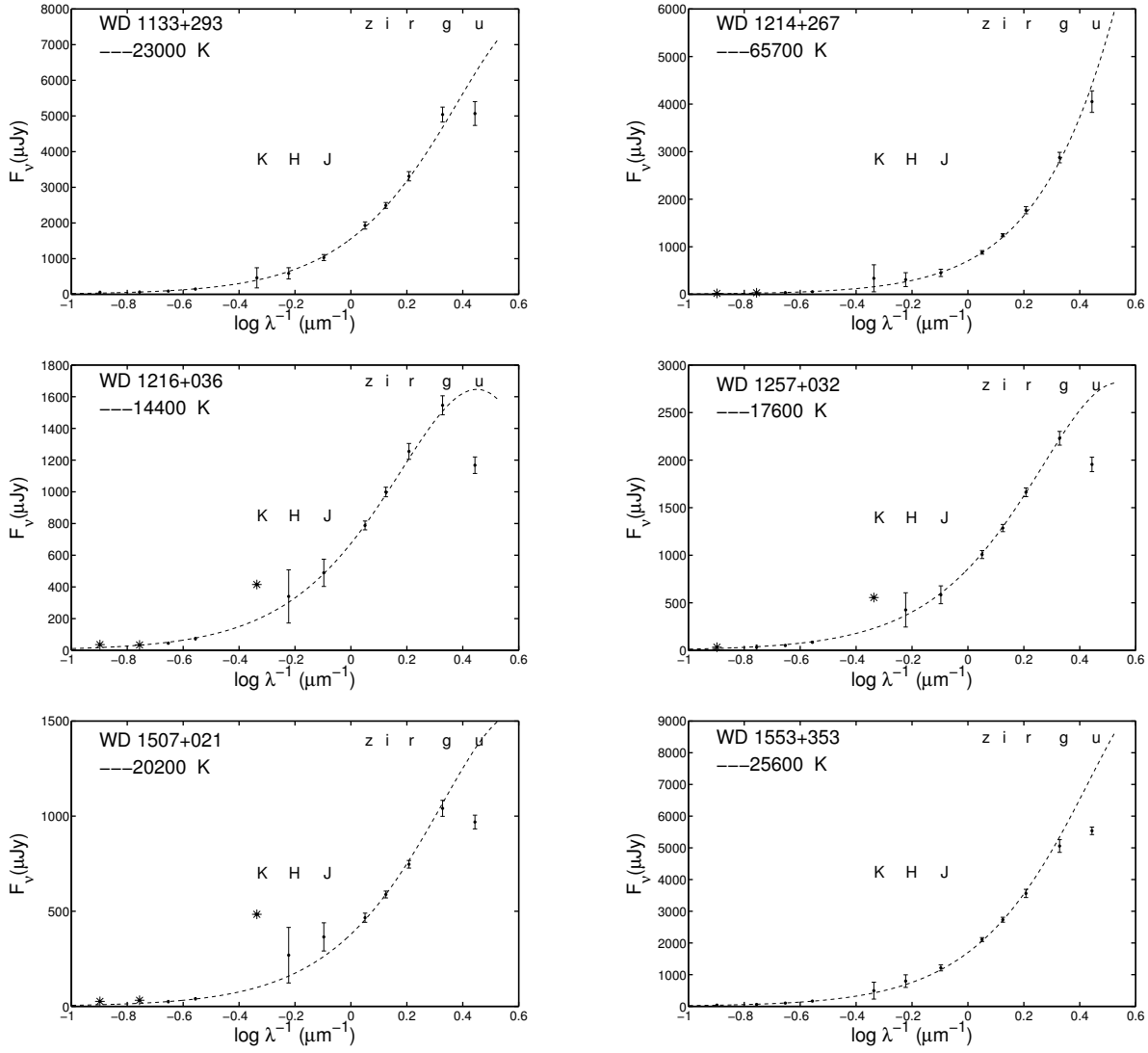

Figure 2.7 The same afigs Figure 2.6.

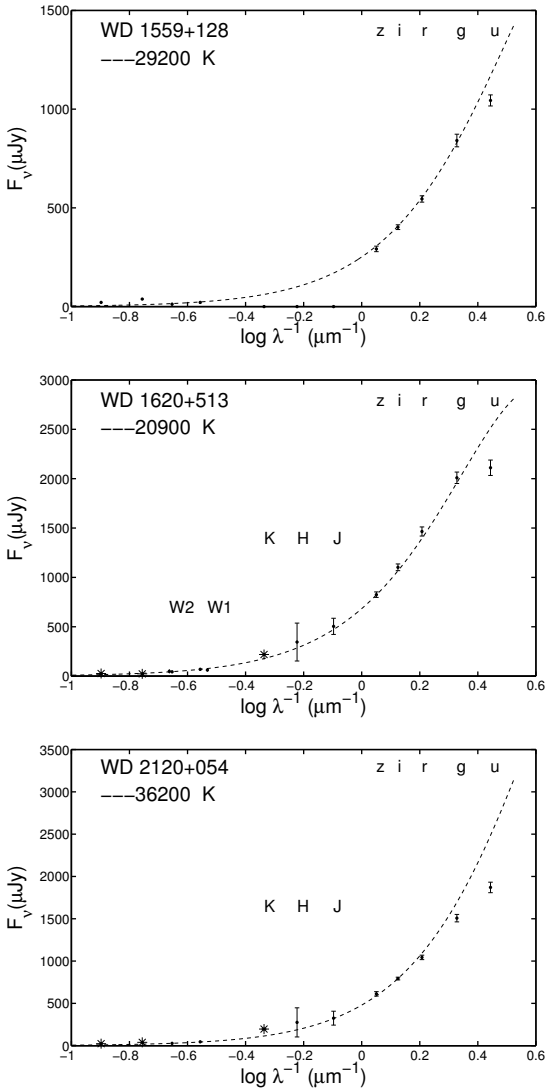

Figure 2.8 The same as Figure 2.6.

2.3.2 Notes on Individual Stars

2.3.2.1 WD 0216-095

This star is heavily blended with a nearby galaxy SDSS J021836.98-091955.7 with an angular separation of 2.″6 at position angle 210°. We take a proper motion of 130 mas/yr in RA and 43 mas/yr in Dec from the NOMAD catalog (Zacharias et al., 2005) to derive a position of 02:18:36.77-09:19:44.24 at the epoch of the Spitzer observation. Then we used the method

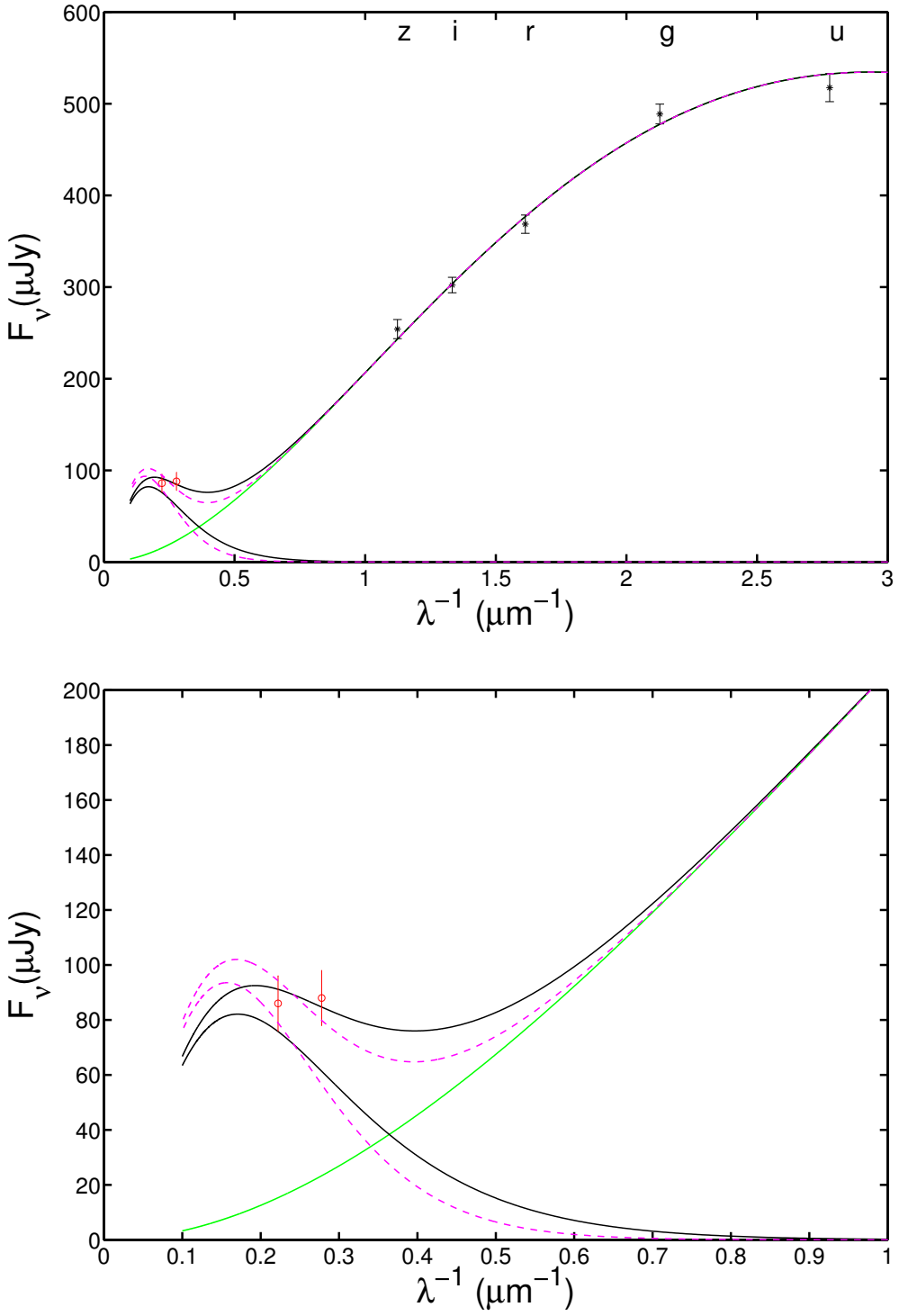

Figure 2.9 SED for J2209+1223. The green line displays the photospheric flux from the star. The black lines and dashed pink lines represent the two disk models listed in Table 2.6: the flux from the disk and its total flux. The upper panel shows the fit to the entire model while the lower panel shows the fit to the disk; 2σ error bars are displayed.

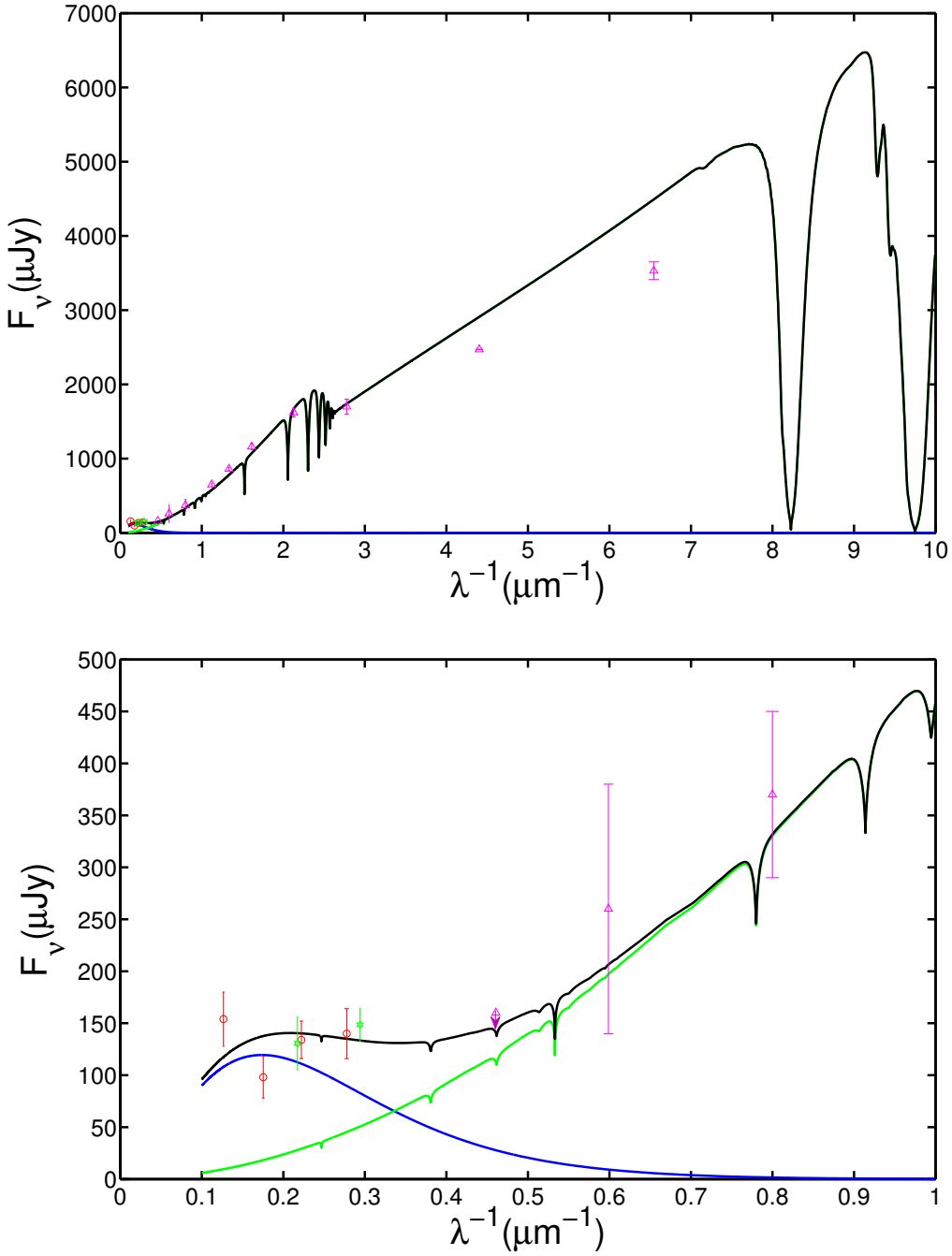

Figure 2.10 SED for WD 0843+516. The green line displays the model atmosphere (D. Koester, private communication), the blue line the model disk and the black line the sum of both. The upper panel shows the entire fit to the model atmosphere while the lower figure only shows the disk portion. The pink dots are taken from GALEX, SDSS, 2MASS, green dots from WISE and red dots from IRAC, respectively; 2σ error bars are displayed.

described above to resolve these two objects. No excess is detected for this star.

2.3.2.2 WD 0936+560

In Figure 2.3, we see the 2MASS H band upper limit is significantly lower than our predicted photospheric flux. Based on the SDSS photometry and the near infrared spectra for this star in Kilic et al. (2008a), we assign a very low weight for this point when fitting the SED and no infrared excess is found for this star.

2.3.2.3 J2209+1223

The IRAC image of this star reveals an unresolved background star separated at $6\farcs2$ at position angle 333° (see Figure 2.1). The proper motion of this star is small enough that it is neglected. Robust centroid methods were used in each exposure to accurately determine the position of these two objects, and then PRF fitting was performed. To demonstrate the effectiveness of the PRF fitting, the original image and residue after subtracting the star are shown in Figure 2.1.

Figure 2.9 shows the SED for J2209+1223; we see a strong infrared excess in both IRAC bands, which is better explained by a flat disk rather than a companion. In the disk models of Jura (2003), there is a degeneracy between the inclination of the disk and its size. With only two data points, there are two sets of parameters as listed in Table 2.6 that can reproduce the SED: a more inclined larger disk or more face-on smaller disk. Another good fit to the SED is a blackbody with T = 1000 K and R = $9R_{\odot}$ at the same distance as the white dwarf, 190 pc. However, this derived radius is much too large for a brown dwarf. Furthermore, there is no feature indicative of M dwarf companions, such as Hα emission or TiO absorption lines in the SDSS spectra of this star.

J2209+1223 has an effective temperature of 17,300 K with an accretion rate of 3×10^{10} g s^{-1}; this value is quite uncertain as it is derived from scaling the equivalent width of magnesium lines from GD 61, which is a white dwarf with similar stellar parameters (Farihi et al., 2011). This star falls into the catalog of highly polluted warm white dwarfs with an

infrared excess.

2.3.2.4 G 241-6

We take the proper motion of G 241-6 as 144 mas/yr in RA and 244 mas/yr in Dec (Zacharias et al., 2005) to derive its position at 22:23:33.38+68:37:26.77 in the Spitzer observation. In Figure 2.2, we can see in both IRAC bands this star is heavily blended with an unknown object at an angular separation of 2.″3 at position angle 170°. Another galaxy is present at J222334.23+683723.8 at an angular distance of 5.″5 and position angle 110°. By using PRF fitting, we successfully resolve these objects and no excess is found even though this 15,300 K star is as heavily polluted as GD 40 (Zuckerman et al., 2010), which does have a dust disk (Jura et al., 2007a).

2.3.2.5 WD 0819+363

In four IRAC bands, this star is blended with the galaxy SDSS J082245.87+361410.2 with a distance of 3.″5 at position angle 240° and another unknown object separated at 4.″1 and position angle 110°. The proper motion of this star is -78 mas/yr in RA and -58 mas/yr in Dec (Zacharias et al., 2005), and it is located at 8:22:46.2+36:14:12.04 at the epoch of the Spitzer observation. PRF fitting was performed in the 3.6 μm and 4.5 μm band and no excess was found. In the 5.7 μm and 7.9 μm band, the background is so noisy that APEX failed to perform PRF fitting in the nominal position derived from IRAC band 1 and 2. Instead we used aperture photometry at the position of the star and there appears to be a 3σ excess as shown in Figure 2.6. However, this is unlikely to be real considering the complicated field.

2.3.2.6 WD 0843+516

Fig 2.10 shows the SED for WD 0843+516, apparently the hottest white dwarf so far detected to have a dust disk. The model atmosphere was provided by D. Koester (private communication). An opaque disk model can reproduce the data with the parameters listed in Table 2.6. As previously found with GD 362 (Jura et al., 2007a), the model tends to

Table 2.6. Disk Model Parameters

Name	T_* (K)	r_*/D^a (10^{-12})	T_{inner} (K)	T_{outer} (K)	r_{inner} (R_*)	r_{outer} (R_*)	cos i
WD 0843+516	23,900	3.9	1,260	640	30	75	0.17
J2209+1223	15,000	1.6	1,340	590	15	45	0.08
		1.6	910	710	25	35	0.29

[a]This is the ratio of the stellar radius and its distance to the Sun.

underpredict the flux at 7.9 μm, which might be contaminated by strong silicate emission in this band. An M dwarf companion can be ruled out as there is no excess in the JHK bands (see Hoard et al. (2007)). Another fit to the SED can be achieved with a blackbody of T = 800 K and R = $0.22R_\odot$ at 80 pc. However, this radius is much too large for a brown dwarf, so this possibility is also excluded. So far WD 0843+516 is the only white dwarf with an infrared excess that is yet to know whether it is polluted as there is no suitable spectra reported in the literature.

2.4 Results

2.4.1 Missing Planetary Debris Around Cool Stars

Warm dust has been found around 21 white dwarfs with temperatures ranging from 9,500 K to 24,000 K and at least 20 of them have a highly polluted atmosphere. Between 1% to 3% single white dwarfs with cooling ages less than 0.5 Gyr possess warm circumstellar dust (Farihi et al., 2009). In contrast, the disk fraction around cool white dwarfs ($T_* < 6000$ K) only has an upper limit of 0.8% (Kilic et al., 2009). Previously, 11 DZs have been targeted with Spitzer/IRAC (Farihi et al., 2008a,b, 2009), but none shows an infrared excess. In this study, we observed 10 additional DZs, which are heavily polluted and most likely disk-host stars. Though almost doubling the numbers of DZs, we still fail to find any infrared excess. We address the implications and possible explanations in section 5 and 6.

2.4.2 Hot White Dwarfs with a Close-in Disk

As discussed by von Hippel et al. (2007), we need to understand how solid dust grains can survive around hot white dwarfs. Dust disks have been confirmed around four stars with stellar temperature higher than 20,000 K: WD 0843+516 (this paper), GALEX 1931 (Debes et al., 2011), PG 1457-086 (Farihi et al., 2009) and WD 1226+110 (Brinkworth et al., 2009). Currently, there are two different models to describe the inner boundary of the disk: a fully opaque disk model (Jura, 2003) and an opaque disk with a thin transition zone, which goes from optically thin to optically thick (Rafikov, 2011a). However, for the hot white dwarfs, only the opaque disk model allows the inner boundary of the disk to be within the tidal radius,

$$r_{inner} = \left(\frac{2}{3\pi}\right)^{1/3} \left(\frac{T_*}{T_s}\right)^{4/3} r_* \tag{2.1}$$

where T_* and r_* is the stellar temperature and radius. T_s is the temperature at which the dust particles sublimate; it can be constrained from the 3.6 μm excess and it is usually 1200 K (see, for example, Jura et al. (2007a)). So for a 20,000 K star, the inner boundary for a complete opaque disk is 25 r_*.

In the model described by Rafikov (2011a), the inner boundary of the optically thin region is,

$$r_{inner} = \frac{r_*}{2} \left(\frac{T_*}{T_s}\right)^2 \tag{2.2}$$

For a 20,000 K star, the inner radius is 140 r_*, whereas the tidal radius is approximately 130 r_* (von Hippel et al., 2007). In this case, all the dust particles lie outside of the tidal radius.

We have no way to resolve the disk and directly tell which model is correct, but the fully opaque disk model is the simplest explanation for the presence of close-in dust. There are two additional arguments in favor of the opaque disk model: it can reproduce the substantial amount of infrared excess and the dust disk radii agree with those derived from gaseous emission lines (Melis et al., 2010). Further discussion is in presented in the Appendix, where

we consider P-R drag on a completely opaque disk described by Jura (2003) and derive an accretion rate that agrees better with the data than the model described in Equation (2.2) (Rafikov, 2011a).

2.5 Characteristics of Disk-host Stars

We see the planetary debris seems to be missing around the polluted cool stars. Why is that? In this section, we explore different characteristics that might be correlated with the occurrence of a dust disk.

2.5.1 High Heavy Element Accretion Rate?

It is found that at least 50% of white dwarfs with heavy element accretion rate over 3×10^8 g s^{-1} have warm dust (Farihi et al., 2009). But cool stars do not appear to follow this pattern. Figure 2.11 shows a comparison of the overall accretion rate with a white dwarf's stellar temperature. We see that there are numerous cool white dwarfs ($T_* < 10{,}000$ K), that have an accretion rate higher than 3×10^8 g s^{-1}, but none displays a dust disk.

To calculate the accretion rate of element A, we assume a steady state so it equals the mass of A in the convective zone divided by its settling time. For the stars that have well determined major element abundances, the accretion rate is simply the sum of all the heavy elements. For the stars that have both magnesium and iron abundance, we assume they are 30% of the total mass of the parent body. For the Cycle 7 targets, calcium is the only detected element and we assume it is 0.6% of the total mass, extrapolated from the cool DZs in Koester et al. (2011). All the stellar parameters are extrapolated from Koester (2009); Koester et al. (2011).

2.5.2 Massive Parent Bodies?

Another possibility is that while more massive parent bodies can form a dusty disk, less massive parent bodies can only form a more tenuous, short-lived dust disk or a purely gaseous

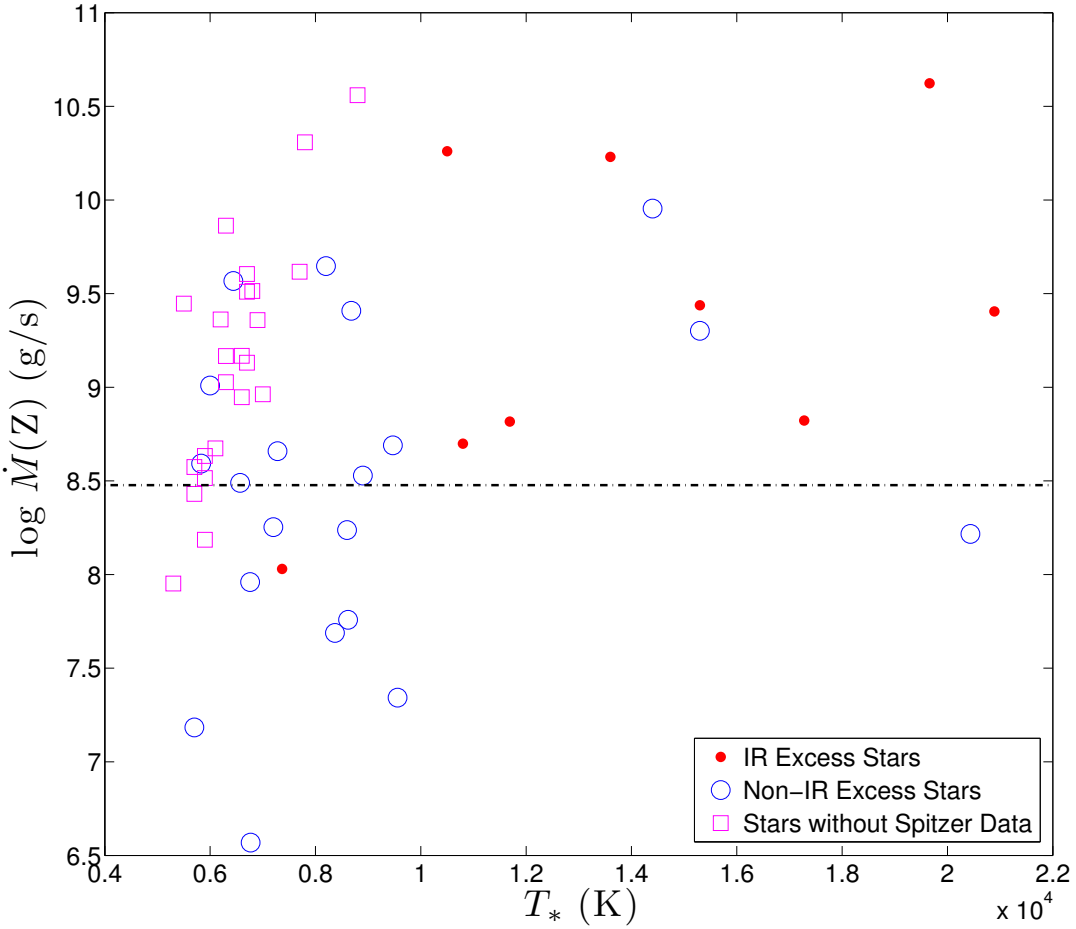

Figure 2.11 Accretion rates at different stellar temperatures. The data include stars with well determined major element abundance, newly identified heavily polluted DZs (Koester et al., 2011), DAZs (Zuckerman et al., 2003) and Cycle 7 stars reported in this paper. The dash-dotted line represents an accretion rate of 3×10^8 g s^{-1}, a threshold proposed by Farihi et al. (2009): over 50% of single white dwarfs with accretion rate at least this high display an infrared excess from ∼1000 K dust.

disk (see Jura (2008)). A comparison of the mass of heavy elements in the atmosphere versus the white dwarf's effective temperature is shown in Figure 2.12. We see there is no difference in the mass in the convective zone, $M(Z)$, between stars with and without an infrared excess. An uncertainty is that the mass plotted in Figure 2.11 are only lower bounds since we do not know how long the accretion has been going on. Also, there is no reason to think that the as-yet-to be accreted mass in the disk is a function of the star's temperature.

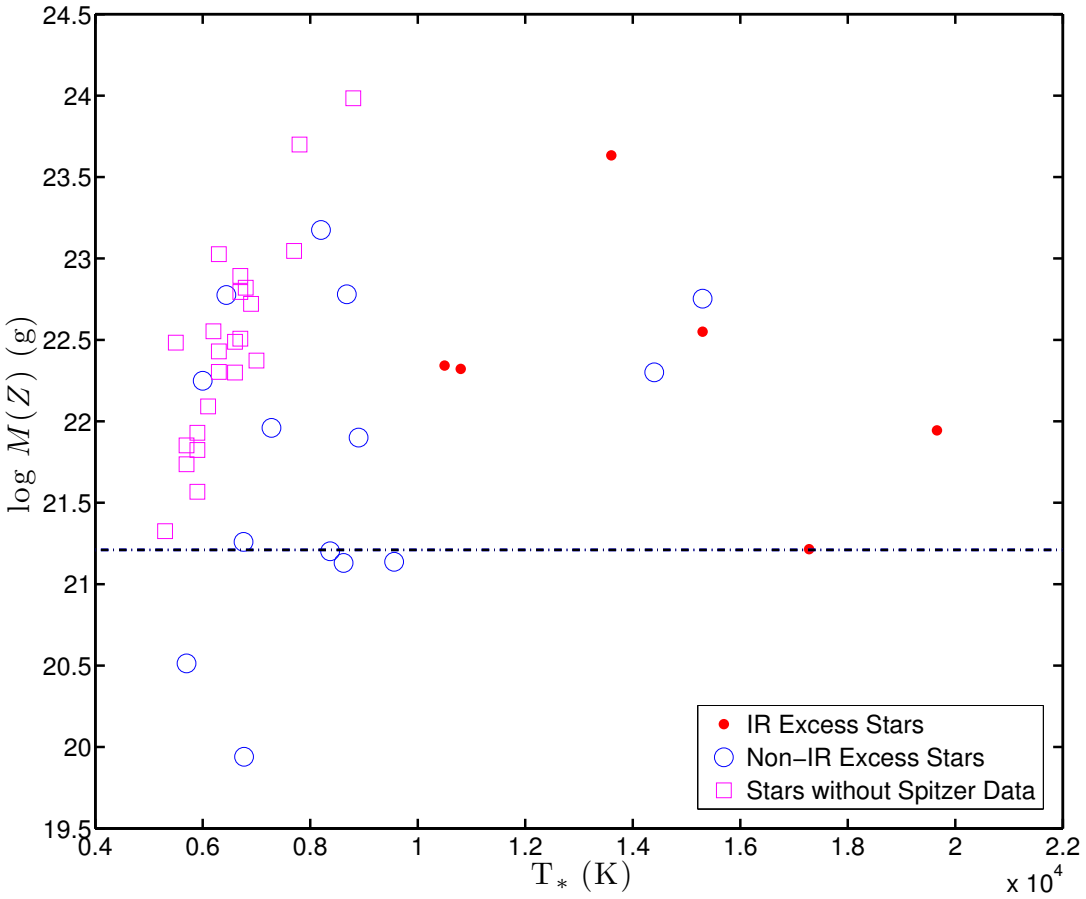

Figure 2.12 Mass of the pollution in the convective zone versus temperature for all the DBZs and DZs in Figure 2.11. The black dashed line denotes the mass in the mixing zone of GD 61, 1.6×10^{21}g, which is the minimum mass found so far to have an infrared excess (Farihi et al., 2011). We see most of the stars are accreting from parent bodies more massive than this value.

2.5.3 Refractory-rich Parent Bodies?

Jura & Xu (2012) argue that there are at least two populations of parent bodies that are accreted onto a white dwarf: water-rich comet-like objects and dry rocky objects. Here we suggest that the compositional variations of the accreted materials might be important in the formation of a dust disk. A comparison between calcium, magnesium and iron accretion rates is plotted in Figure 2.13. $\log \dot{n}(\mathrm{Ca})/\dot{n}(\mathrm{Mg})$ and $\log \dot{n}(\mathrm{Fe})/\dot{n}(\mathrm{Mg})$ versus the star's temperature are shown in order to correct for different settling rates. These values correspond to the intrinsic abundance ratio in the parent body assuming a steady state.

We see in the upper panel of Figure 2.13 that most stars with an infrared excess have relatively high abundance of Ca, a highly refractory element (Allègre et al., 2001); the average [Ca]/[Mg] in these stars is -0.71 while it is -1.21 in bulk Earth. In contrast, when measured in a different sample of DZs than studied here, [Ca]/[Mg] equals -1.42 (Koester et al., 2011). In the lower panel of Figure 2.13, we see Fe abundance almost stays the same. Since iron is one of the dominant elements in bulk Earth as well as white dwarf pollution (Klein et al., 2010), there is no reason to think its abundance should vary a lot. There is additional evidence supporting that cool white dwarfs are accreting more volatile-rich materials. Sodium, which is an important volatile, has a nearly solar abundance in 28 extreme DZs, much higher than the bulk Earth value (Koester et al., 2011; Allègre et al., 2001).

2.6 Origin of Heavy Elements in Stars without an Infrared Excess

We see most polluted white dwarfs do not possess a dust disk. So where do the heavy elements come from? Interstellar accretion was traditionally considered to be the origin of this material (Dupuis et al., 1993) but this model has faced many challenges (Farihi et al., 2010a; Koester et al., 2011). We discuss two avenues of accretion that can pollute a white dwarf's atmosphere without producing a dust disk.

Accretion from a distant reservoir. It has been suggested that some comets go through natural fragmentation due to fast rotation (Drahus et al., 2011) and in this way contribute to

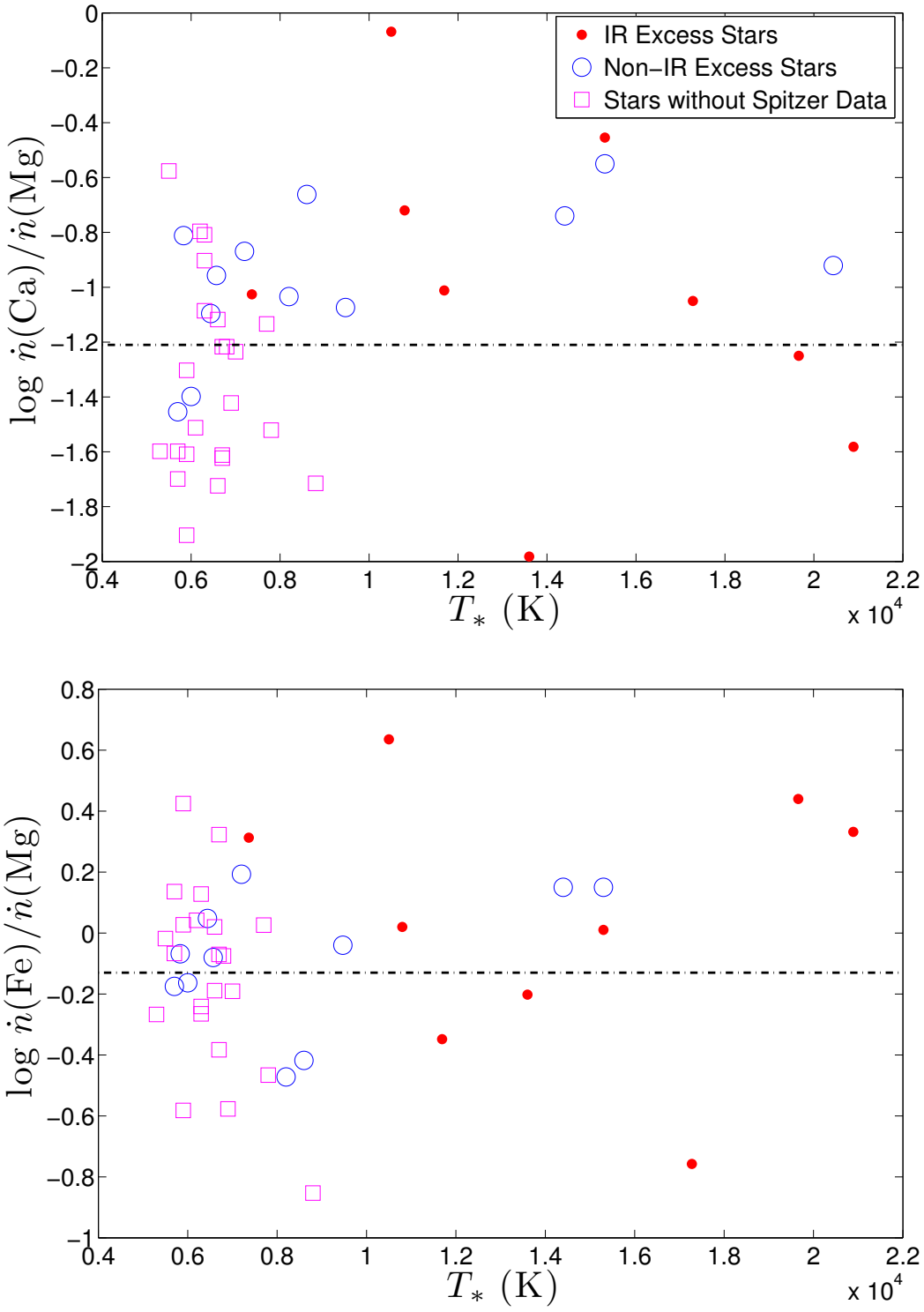

Figure 2.13 Compositional difference for all the stars in Figure 2.11 that have Ca, Mg and Fe detections. The relative abundance has been corrected for settling assuming a steady state. The dashed line is the value for bulk Earth. We see the stars with infrared excess usually have a high $\dot{n}(\mathrm{Ca})/\dot{n}(\mathrm{Mg})$.

the zodiacal light in our solar system (Nesvorný et al., 2010). A similar process might happen around a white dwarf given that there might be a large reservoir of comets. Eventually some of the dust particles will drift inward due to P-R drag and the amount of infrared flux produced at frequency ν is (Jura et al., 2007a),

$$F_\nu \approx \frac{1}{2} ln \left(\frac{R_i}{R_f} \right) \frac{\dot{M}(Z) c^2}{\nu} / 4\pi D^2 \tag{2.3}$$

where R_i, R_f is the initial and final distance of the accretion and R_i/R_f is taken to be 1000, $\dot{M}$(Z) is the total accretion rate, c is the speed of light and D is the distance between the Sun and the white dwarf. We compare the flux predicted from Equation (2.3) with our data for Cycle 7 targets in Table 2.7. For the heavily polluted Cycle 7 targets, we see that the calculated flux is always much higher than the observed value. However, there are other cool white dwarfs with an accretion rate $\sim 10^6$ g s^{-1} (Farihi et al., 2009) where this process might be important.

Accretion from an orbiting gaseous disk. A gaseous disk that does not emit too much in the infrared can be formed if the grains mutually annihilate as described in the model of Jura (2008) or the objects sublimate as they get close to the white dwarf. This is likely to be true for DAZs warmer than 11,000 K because their settling time is only days (Koester, 2009). Without the continuous feeding of material, the elements would have quickly settled.

2.7 Conclusions

We find two new stars with an infrared excess, J2209+1223 and WD 0843+516, apparently the hottest white dwarf with a close-in disk. We fail to find any warm dust around heavily polluted DZs, all of which have $T_* < 10{,}000$ K. We raise the possibility that there might be some correlation between the occurrence of dust disk and the volatility of the accreted material. The best model to explain the source of pollution in white dwarfs without an infrared excess has yet to be established.

Table 2.7. Infrared Flux Produced by Accretion from Cometary Dust

Name	D (pc)	log $\dot{M}$(Z) (g/s)	$F_{4.5\mu m}(\mu Jy)$ predicted[a]	observed
WD 0033-114	55	8.66	6,300	41±3
WD 0216-095	97	7.34	120	17±2
WD 0936+560	65	9.41	25,000	38±2
J0951+4033	84	7.69	310	22±2
WD 1035-003	49	9.65	77,000	37±2
J1309+4913	83	7.76	370	24±2
G 199-63	68	8.53	3,100	37±2
LP 219-80	45	6.61	160	71±4
J2228+1207	34	7.96	3,200	105±6

[a]These values are the predicted total flux, which is the sum of the photospheric flux and the excess due to accretion from the cometary dust.

Note. — This table contains all the Cycle 7 stars with reported distance (Dufour et al., 2006).

2.8 APPENDIX

In this section, we extend the model of Rafikov (2011a) for P-R drag on the entire disk to account for the observed mass accretion rates. Our modification of his model leads to a better agreement with the data.

Assuming a steady state, the accretion rate provided by P-R drag is (Rafikov, 2011a),

$$\dot{M}(r_{inner}) = \frac{16\phi_r}{3}\frac{r_*^3}{r_{inner}}\frac{\sigma T_*^4}{c^2} \tag{2.4}$$

where σ is the Stefan Boltzmann constant, c is the speed of light, and ϕ_r is an efficiency coefficient.

Using Equation (2.2), Rafikov (2011a) derived an accretion rate,

$$\begin{aligned} \dot{M}(r_{inner}) &= \frac{32\phi_r}{3}\sigma\left(\frac{r_* T_* T_s}{c}\right)^2 \\ &= 1.80\times10^8\left(\frac{T_*}{15000K}\right)^2 g\ s^{-1} \end{aligned} \tag{2.5}$$

In the last step we take r_*=0.013 $R_\odot$ and $\phi_r = 1$.

As discussed in section 2.4.2, our inner boundary is described by Equation (2.1); so we get a different value of accretion rate,

$$\begin{aligned} \dot{M}(r_{inner}) &= \left(\frac{3\pi}{2}\right)^{1/3}\frac{16\phi_r\sigma}{3}\left(\frac{r_*}{c}\right)^2 (T_s T_*^2)^{4/3} \\ &= 8.14\times10^8\left(\frac{T_*}{15000K}\right)^{8/3} g\ s^{-1} \end{aligned} \tag{2.6}$$

A comparison between these two accretion rates are shown in Figure 2.14 and we see they differ as much as a factor of 5.

Observationally, we can also derive the accretion rate from the atmospheric pollution.

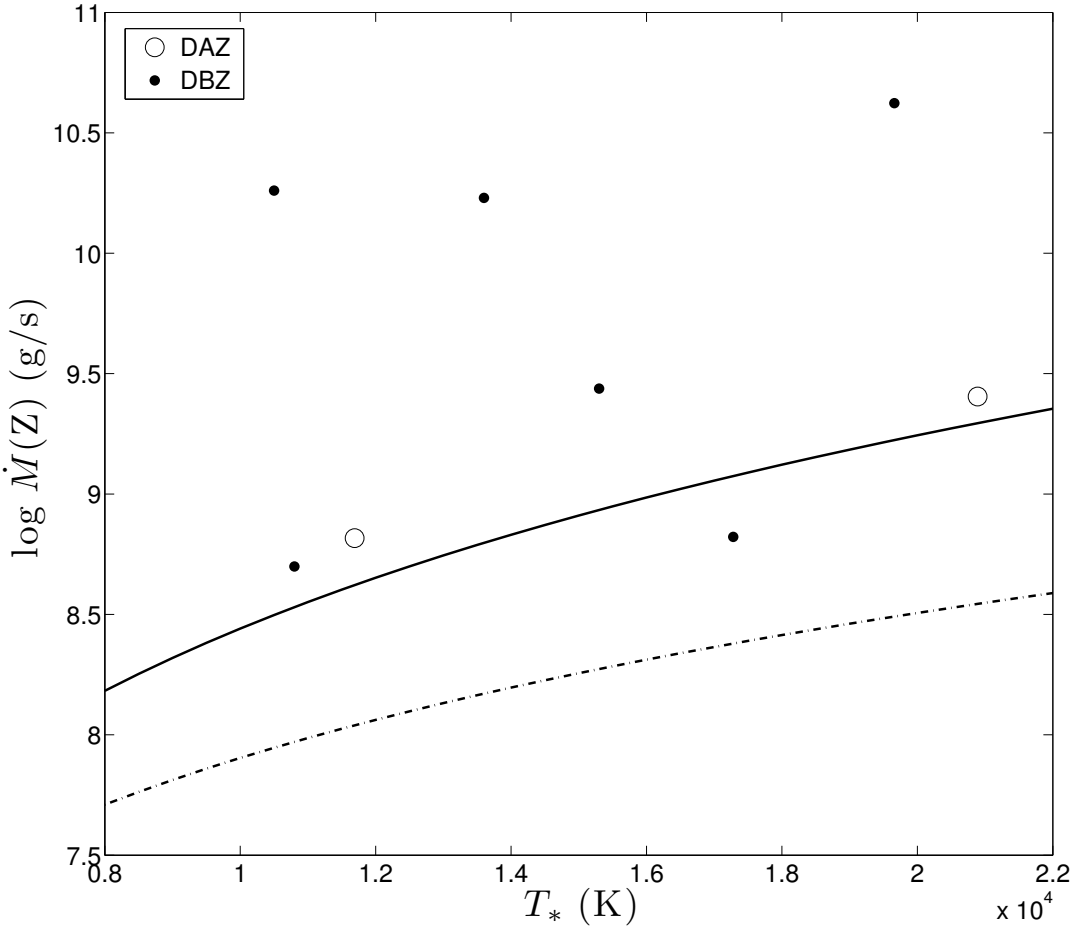

Figure 2.14 Mass accretion rate onto white dwarfs with an infrared excess. The solid line shows the value predicted by our model while the dashed line is the value derived in Rafikov (2011a). The DAZs are G29-38 (Koester, 2009) and GALEX 1931 (Vennes et al., 2011). And DBZs are GD 40 (Klein et al., 2010), GD 61 (Farihi et al., 2011), SDSS J0738 (Dufour et al., 2010), PG 1225-079 (Klein et al., 2011), Ton 345 (D. Koester, private comminucation) and GD 362 (Koester, 2009). All the stars in this figure have well determined major element abundance.

Since we are trying to make a comparison between models that vary by a factor of 5, we need accurate abundances. Therefore, we only consider stars that have measurements for at least three of the four major elements in white dwarf pollution (Klein et al., 2010): O, Mg, Si and Fe. In Figure 2.14, we see the accretion rates derived from our model and spectroscopical analysis agree well for DAZs. Since the settling time for heavy elements is relatively short in these stars, the presence of a dusty disk indicates the accretion should be in a steady state (Koester, 2009), which satisfies the assumption of the calculation above. For DBZs, the settling time is comparatively longer and we cannot determine if the system is in the build-up phase or steady state. The accretion rate driven by PR drag gives a good lower bound in these stars and there might be other mechanisms on top of that, as discussed in Rafikov (2011b).

CHAPTER 3

Two Beyond-Primitive Extrasolar Planetesimals

Reproduced by permission of the AAS (Xu, S., Jura, M., Klein, B., Koester, D., & Zuckerman, B., 2013, Astrophysical Journal, 766, 132).

3.1 Introduction

Planetesimals are building blocks of planets and their formation is a key step towards planet formation. How do planetesimals form? What determines their bulk composition? To answer these questions, we start by examining our own solar system.

The overall configuration of the solar system is that volatile-depleted, dry rocky objects are ubiquitous relatively close to the Sun while volatile-rich, icy objects are found beyond the snow line. This correlation between the volatile fraction and heliocentric distance can be explained by primitive nebular condensation: refractory elements condensed closer to the Sun while volatile elements can only be incorporated into the planetesimals where the temperature is low enough. Many solar system objects have experienced some additional processing that changed their initial compositions. For example, it has been argued that a collision between a large asteroid and proto-Mercury stripped off most of Mercury's silicate mantle, leaving it $\sim$70% iron by mass (Benz et al., 1988). Also, the "late veneer" has delivered a large amount of water and volatiles onto Earth (Chyba, 1990). Post-nebular processing, such as collisions, melting and differentiation, is important in redistributing the elements among solar system objects.

Currently, the best way to measure the elemental compositions of planetesimals in the solar system is from meteorites, which are fragments from collisions among asteroids. Follow-

ing O'Neill & Palme (2008), we classify all meteorites into two categories in this paper. (i) "Chondritic" is used to refer to chondrites, which are a direct product of nebular processing. Objects in this category are described as "primitive" planetesimals. (ii) "Non-chondritic" objects consist of achondrites, stoney-iron meteorites and iron meteorites. Examples of their parent bodies include the Moon, Mars or asteroids that have experienced various amounts of post-nebular processing. Planetesimals in this category are considered to be "beyond-primitive".

What about planetesimal formation in extrasolar planetary systems? High-resolution, high-sensitivity spectroscopic observations of externally-polluted white dwarfs are a powerful tool for determining the bulk elemental compositions of extrasolar planetesimals (Jura, 2013). Calculations show that minor planets can survive the red giant stage of a star and persist into the white dwarf phase with most of their internal water and volatiles intact (Jura, 2008; Jura & Xu, 2010). Orbital perturbations from one or multiple planets can cause these planetesimals to stray into the tidal radius of the white dwarf and get tidally disrupted (Debes & Sigurdsson, 2002; Bonsor et al., 2011; Debes et al., 2012b), sometimes producing a dust disk that emits mostly in the infrared (Jura, 2003; Kilic et al., 2006; von Hippel et al., 2007; Farihi et al., 2009; Xu & Jura, 2012). Eventually, all this planetary debris is accreted onto the central white dwarf and pollutes its otherwise pure hydrogen or helium atmosphere.

The first comprehensive abundance measurement of an externally-polluted white dwarf was performed by Zuckerman et al. (2007), who identified 15 elements heavier than helium in the atmosphere of GD 362, including Mg, Si and Fe, which are often called the "common elements" (Larimer, 1988). The disrupted object had a minimum mass $\sim 10^{22}$ g, which is comparable to that of a massive solar system asteroid. Three years later, the abundances of eight heavy elements were determined in the atmosphere of GD 40, including all the major rock-forming elements – O, Mg, Si and Fe (Klein et al., 2010). Now there are many more high-resolution optical spectroscopic studies of externally-polluted white dwarfs [e.g., Klein et al. (2011); Melis et al. (2011); Zuckerman et al. (2011); Farihi et al. (2011); Dufour et al. (2012); Vennes et al. (2010, 2011)].

However, optical spectroscopy of externally-polluted white dwarfs typically does not en-

able sensitive detection of highly-volatile elements, such as carbon, nitrogen and sulfur, which are key to understanding the thermal history of the system. Ultraviolet spectroscopy is complimentary to optical observations in determination of volatile abundances.

To-date, there are four white dwarfs with both published high-resolution optical and ultraviolet measurements[1]; we are beginning to accumulate an atlas of the compositions of extrasolar planetesimals. To zeroth order, we find that they are strikingly similar to meteorites in the solar system: (i) O, Mg, Si and Fe are always dominant and their sum is more than 85% of the accreted mass; (2) volatile elements, especially C, are typically depleted by more than a factor of 10 compared to solar abundances[2].

In this paper, we report ultraviolet spectroscopic observations of GD 362 and PG 1225-079 with the Cosmic Origins Spectrograph (COS) onboard the Hubble Space Telescope (HST), complimentary to previous optical studies from the Keck High Resolution Echelle Spectrometer (HIRES) (Zuckerman et al., 2007; Klein et al., 2011). PG 1225-079 has been observed with the low-resolution International Ultraviolet Explorer (IUE) (Wolff et al., 2002); there is no previous ultraviolet spectroscopy for GD 362. The rest of the paper is organized as follows. Data reduction is summarized in section 2 and atmospheric abundance determinations are reported in section 3. In section 4, we used a reduced chi-squared analysis to look for solar system analogs to the accreted parent bodies. The formation mechanisms of extrasolar planetesimals are assessed in section 5 and conclusions are given in section 6. In Appendix A, we report the Herschel Photodetecting Array Camera and Spectrometer (PACS) observation of GD 362. In Appendix B, we extend the reduced chi-squared analysis to two additional externally-polluted helium white dwarfs with both high-resolution optical and ultraviolet observations.

[1]The four white dwarfs are: GD 61 (Desharnais et al., 2008; Farihi et al., 2011); GD 40, G241-6 (Klein et al., 2010, 2011; Zuckerman et al., 2010; Jura et al., 2012) and WD 1929+012 (Vennes et al., 2010, 2011; Melis et al., 2011; Gänsicke et al., 2012).

[2]Very recently, Koester et al. (2012) reported several white dwarfs with solar carbon-to-silicon ratio. However, the source of this pollution is unclear and more analysis is forthcoming.

3.2 Observations and Data Reduction

GD 362 and PG 1225-079 were observed during HST/COS Cycle 18 under program 12290. These two white dwarfs are too cool to be observed effectively with the G130M grating centering around 1300 Å, as was employed by Jura et al. (2012) and Gänsicke et al. (2012) for other hotter white dwarfs. Instead, the G185M grating was used with a central wavelength of 1921 Å and wavelength coverage of 1800 – 1840 Å, 1903 – 1940 Å and 2008 – 2044 Å. The spectral resolution was ∼18,000. Total exposure times were 7411 and 1805 sec for GD 362 and PG 1225-079, respectively.

The raw data were processed using the standard pipeline CALCOS 2.13.6. The fluxes at 2030 Å are 2.9×10^{-15} erg s^{-1} cm^{-2} Å^{-1} and 1.5×10^{-14} erg s^{-1} cm^{-2} Å^{-1} for GD 362 and PG 1225-079, respectively, in approximate agreement with broadband NUV fluxes from the GALEX satellite. The signal-to-noise ratio (SNR) in the original un-smoothed spectrum was 6 for PG 1225-079 and 4 for GD 362.

Following previous data reduction procedures (Klein et al., 2010, 2011; Jura et al., 2012), for PG 1225-079, equivalent widths (EWs) of each spectral line were measured in the un-smoothed spectra by fitting a Voigt profile with three different nearby continuum intervals in IRAF. The EW uncertainty is calculated by adding the standard deviation of the three EWs and the average uncertainty from the profile fitting in quadrature. The EW upper limit is obtained by artificially inserting a spectral line with different abundance into the model and comparing with the data. We adopt a different method to measure the EW for C I 1930.9 Å in GD 362, as described in section 3.1. The measured values are listed in Tables 3.1 and 3.2 for GD 362 and PG 1225-079, respectively. The average Doppler shift relative to the Sun for PG 1225-079 is 42 ± 13 km s^{-1}, in essential agreement with the value 49 ± 3 km s^{-1} derived from optical studies (Klein et al., 2011). The large velocity dispersion in the ultraviolet is due to the low SNR of the spectrum and the ∼ 15 km s^{-1} uncertainty of COS (COS Instrument Handbook). For GD 362, we marginally detected C I 1930.9 Å and it has a Doppler shift of 48 km s^{-1}, in agreement with 49.3 ± 1.0 km s^{-1} from the optical study (Zuckerman et al., 2007).

Table 3.1 Measured Equivalent Widths and Abundance Determinations for GD 362

Ion	λ (Å)	E_{low} (eV)	EW (mÅ)	log n(Z)/n(He)
C I	1930.905	1.26	$560\ ^{+230}_{-158}$ [a]	-6.70 ± 0.30
S I	1807.311	0	$\lesssim 900$	$\lesssim$ -6.70
S I	1820.341	0.049	$\lesssim 710$	$\lesssim$ -6.40
S				$\lesssim$ -6.70

[a] This is measured from the model spectra, as described in section 3.1.

Table 3.2 Measured Equivalent Widths and Abundance Determinations for PG 1225-079

Ion	λ (Å)	E_{low} (eV)	EW (mÅ)	log n(Z)/n(He)
C I	1930.905	1.26	1600 ± 200	-7.80 ± 0.10
S I	1807.311	0	$\lesssim 170$	$\lesssim$ -9.50
S I	1820.341	0.049	$\lesssim 150$	$\lesssim$ -9.30
S				$\lesssim$ -9.50
Mg I	2026.477[a]	0	288 ± 100[b]	$\lesssim$ -7.60
Si II	1808.013	0	936 ± 109	-7.44 ± 0.10
Si II	1816.928	0.04	1232 ± 145	-7.46 ± 0.10
Si				-7.45 ± 0.10
Fe II	1925.987	2.52	192 ± 72	-7.62 ± 0.28
Fe II	2011.347	2.58	309 ± 97	-7.35 ± 0.24
Fe II	2019.429	1.96	211 ± 67	-7.56 ± 0.24
Fe II	2021.402	1.67	181 ± 68	-7.71 ± 0.27
Fe II	2033.061	2.03	311 ± 67	-7.24 ± 0.17
Fe II	2041.345	1.964	215 ± 50	-7.24 ± 0.18
Fe				-7.45 ± 0.23
Zn II	2026.136	0	288 ± 47[b]	$\lesssim$ -11.30

[a] The atomic parameters for this line are taken from Kelleher & Podobedova (2008).
[b] Mg I 2026.5 Å and Zn II 2026.1 Å are blended and the reported EW is for the entire feature.

3.3 Atmospheric Abundance Determinations

Because we are most interested in the abundance of an element relative to other heavy elements and these ratios are not strongly dependent upon the stellar temperature and surface gravity (Klein et al., 2011), we only adopt one set of stellar parameters as listed in Table 3.3 and compute the model spectra following Koester (2010). Atomic data are mostly taken from the Vienna Atomic Line Database (Kupka et al., 1999). The computed model atmosphere spectra were convolved with the COS NUV line spread function[3]. The abundance of each element was derived by comparing the EW of each spectral line with the value derived from the model atmosphere, as shown in Figures 3.1-3.5 and Tables 3.1 and 3.2. The final abundances, combining ultraviolet with optical observations, are given in Tables 3.4 and 3.5 for GD 362 and PG 1225-079, respectively. Our results mostly agree with previous reports but have a higher accuracy. For PG 1225-079, we newly derive the abundances of carbon and silicon and have tentative detections of sulfur and zinc. The magnesium abundance is updated while the iron abundance agrees with previous optical results. Because the data are noisier for GD 362, we are only able to crudely constrain the abundance of carbon and sulfur.

Table 3.3 Adopted Stellar Properties for GD 362 and PG 1225-079

star	M_* ($M_\odot$)	T (K)	log g (cm^2 s^{-1})	D (pc)	log M_{cvz}/M_*[a]	Ref
GD 362	0.72	10,540	8.24	51	-6.71	(1) (2)
PG 1225-079	0.58	10,800	8.00	26	-5.02	(3) (4)

[a] Newly-derived mass of the convective zone (see section 4).
References.(1) Kilic et al. (2008b); (2) Zuckerman et al. (2007); (3) Klein et al. (2011); (4) Farihi et al. (2005).

[3]http://www.stsci.edu/hst/cos/performance/spectral_resolution/nuv_model_lsf

Table 3.4 Atmospheric Abundances for GD 362

Z	log n(Z)/n(He)[a]	t_{set}[b] (10^5 yr)	$\dot{M}(Z_i)$[c] (g s^{-1})
H	-1.14 ± 0.10	...	...
C*	-6.70 ± 0.30	2.1	2.5×10^7
N	< -4.14	2.2	$< 9.0 \times 10^9$
O	< -5.14	2.2	$< 1.1 \times 10^9$
Na	-7.79 ± 0.20	2.2	3.7×10^6
Mg	-5.98 ± 0.25	2.2	2.5×10^8
Al	-6.40 ± 0.20	1.6	1.5×10^8
Si	-5.84 ± 0.30	1.2	7.2×10^8
S*	$\lesssim$ -6.70[d]	0.79	$\lesssim 1.7 \times 10^8$
Ca	-6.24 ± 0.10	0.99	5.1×10^8
Sc	-10.19 ± 0.30	0.93	6.8×10^4
Ti	-7.95 ± 0.10	0.94	1.2×10^7
V	-8.74 ± 0.30	0.95	2.1×10^6
Cr	-7.41 ± 0.10	1.0	4.3×10^7
Mn	-7.47 ± 0.10	1.0	4.0×10^7
Fe	-5.65 ± 0.10	1.1	2.5×10^9
Co	-8.50 ± 0.40	0.99	4.1×10^6
Ni	-7.07 ± 0.15	1.0	1.1×10^8
Cu	-9.20 ± 0.40	0.83	1.1×10^6
Sr	-10.42 ± 0.30	0.56	1.3×10^5
Total			4.4×10^9

* New measurements from this paper. The rest are from Zuckerman et al. (2007) but we reference abundances relative to He, the dominant element in GD 362's atmosphere, rather than H, as presented in Zuckerman et al. (2007). Consequently, there is a possible systematic offset up to 0.1 dex in all entries derived from that paper.

[a] The final abundance of an element combining optical and ultraviolet data.

[b] Newly-derived settling times in the convective zone (see section 4); they are typically a factor of 2-3 longer than previously-derived values in Koester (2009).

[c] Accretion rates calculated from Equation (1).

[d] The equality sign corresponds to the red model fit shown in figures.

Table 3.5 Atmospheric Abundances for PG 1225-079

Z	log n(Z)/n(He)	t_{set} (10^6 yr)	$\dot{M}(Z_i)$ (g s^{-1})
H	-4.05 ± 0.10	...	...
C*	-7.80 ± 0.10	5.5	3.1×10^6
O	< -5.54	4.5	$< 9.1 \times 10^8$
Na	< -8.26	4.4	$< 2.6 \times 10^6$
Mg*	-7.50 ± 0.20	4.8	1.4×10^7
Al	< -7.84	3.6	$< 9.5 \times 10^6$
Si*	-7.45 ± 0.10	3.0	3.0×10^7
S*	$\lesssim$ -9.50	1.7	$\lesssim 5.2 \times 10^5$
Ca	-8.06 ± 0.03	1.9	1.6×10^7
Sc	-11.29 ± 0.07	1.8	1.1×10^4
Ti	-9.45 ± 0.02	1.8	8.3×10^5
V	-10.41 ± 0.10	1.8	9.6×10^4
Cr	-9.27 ± 0.06	1.9	1.3×10^6
Mn	-9.79 ± 0.14	2.0	4.0×10^5
Fe	-7.42 ± 0.07	2.1	9.0×10^7
Ni	-8.76 ± 0.14	2.3	4.0×10^6
Zn*	$\lesssim$ -11.30	2.2	$\lesssim 1.3 \times 10^4$
Sr	< -11.65	1.2	$< 1.4 \times 10^4$
Total			1.6×10^8

* New results from this paper. The rest are from Klein et al. (2011).
Notes. The columns are defined the same as Table 3.4.

3.3.1 Carbon

There is only one useful carbon line in the observed wavelength interval, C I 1930.9 Å, as shown in Figures 3.1 and 3.2. Because it arises from an excited level, it cannot be contaminated by interstellar absorption. However, this line can be blended with Mn II 1931.4 Å. Fortunately, accurate Mn abundances have been determined for both stars from optical data (Zuckerman et al., 2007; Klein et al., 2011) and the predicted EW for Mn II 1931.4 Å is less than 50 mÅ in the model spectrum. Considering the measured EW of this feature is more than 500 mÅ for both stars (see Tables 3.1 and 3.2), we conclude that the line is dominated by C I 1930.9 Å. For PG 1225-079, our derived carbon abundance[4] [C]/[He] = -7.80 ± 0.10 agrees with the IUE upper limit of -7.5 (Wolff et al., 2002).

For GD 362, the largest uncertainty is from the low SNR of the data; the measured continuum flux is (3.1 ± 1.0) × 10^{-15} erg s^{-1} cm^{-2} $Å^{-1}$. It is hard to measure the EW of C I 1930.9 Å directly from the noisy data. Instead, we computed model spectra with different carbon abundance to match the observed spectrum. In Figure 3.1, we present three best-fit models with [C]/[He] = - 6.4, [C]/[He] = -6.7, [C]/[He] = -7.0 and a continuum flux at 4.1 × 10^{-15} erg s^{-1} cm^{-2} $Å^{-1}$, 3.1 × 10^{-15} erg s^{-1} cm^{-2} $Å^{-1}$, 2.1 × 10^{-15} erg s^{-1} cm^{-2} $Å^{-1}$, respectively. The final abundance is [C]/[He] = -6.7 ± 0.3 and the EW reported in Table 3.1 is measured from the model spectra.

3.3.2 Sulfur

There are two useful sulfur lines, S I 1807.3 Å and S I 1820.3 Å. However, at best, we have only a tentative detection of sulfur in each star. S I 1807.3 Å, the stronger line, is adjacent to Si II 1808.0 Å. Fortunately, for GD 362, the silicon abundance is determined from previous optical data (Zuckerman et al., 2007); for PG 1225-079, other ultraviolet lines can be used to derive the silicon abundance (see section 3.4). The data and model atmosphere spectra for GD 362 and PG 1225-079 are presented in Figures 3.3 and 3.4, respectively. Considering the apparent match between the model and data for both S I lines, tentative sulfur abundances

[4]Here, log n(X)/n(Y) is abbreviated as [X]/[Y].

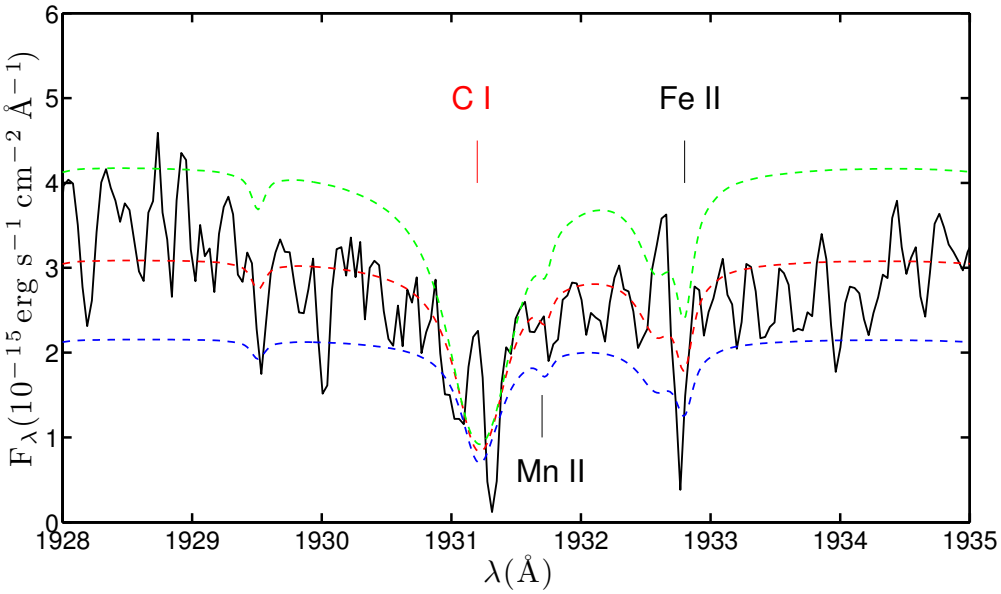

Figure 3.1 HST/COS spectrum of GD 362. The black line is the data smoothed with a 3 pixel boxcar. The green, red, blue line represents the computed model spectrum with [C]/[He] = -6.4, -6.7, -7.0, respectively, placed at a different continuum level; the abundances of other elements are from Table 3.4. The adopted carbon abundance is -6.7 ± 0.3. The red labels represent lines that are used for abundance determinations. Wavelength is presented in the star's reference frame in vacuum.

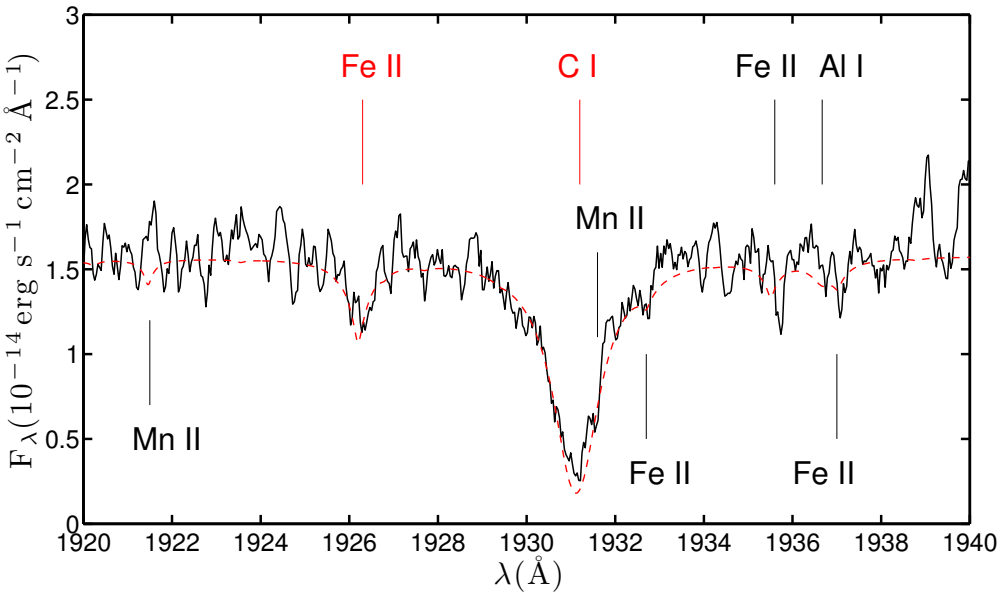

Figure 3.2 Similar to Figure 3.1 except for PG 1225-079
Similar to Figure 3.1 except for PG 1225-079 with abundances from Table 3.5. The data were smoothed with a 5 pixel boxcar.

of -6.7 for GD 362 and -9.5 for PG 1225-079 can be assigned. Conservatively, these results are upper limits.

3.3.3 Magnesium and Zinc

In PG 1225-079, Mg I 2026.4 Å and Zn II 2026.1 Å are heavily blended. As shown in Figure 3.5, our best fit model which matches the measured EW of the absorption feature requires [Mg]/[He] = -7.6 and [Zn]/[He] = -11.3. These values are individually taken as upper limits due to the blending. However, the reported magnesium abundance is -7.27 ± 0.06 from the optical data (Klein et al., 2011), which is largely based on three Mg lines but the detections for two lines are only 2σ. Wolff et al. (2002) reported [Mg]/[He] to be -7.6 ± 0.6 from the IUE data. Averaging these measurements, our final magnesium abundance is -7.50 ± 0.20. Because of the blending, the zinc abundance is only an upper limit. This provides the first stringent constraint on zinc in an extrasolar planetesimal.

3.3.4 Silicon

In PG 1225-079, we measured two silicon lines, Si II 1808.0 Å and Si II 1816.9 Å, as shown in Figure 3.4. Si II 1808.8 Å arises from the ground state and the photospheric line can be distorted by interstellar absorption. However, its measured EW is only 87 ± 11 mÅ in ζ Oph, a star at a distance of 112 pc with a large amount of foreground interstellar gas (Morton, 1975). Considering PG 1225-079 is only 26 pc away, it has much less interstellar absorption. The measured EW is 936 ± 109 mÅ and we conclude that Si II 1808.0 Å is largely photospheric and essentially free from interstellar absorption. The shape of Si II 1808.0 Å in the model does not quite fit the data; but the measured EW of the data, which is key in the abundance determination, has a good agreement with that in the model. Using these two Si II lines, we derive a final silicon abundance of -7.45 ± 0.10, in agreement with, but much better than the reported IUE abundance of -7.5 ± 0.5 (Wolff et al., 2002) and the previous optical upper limit of -7.27 (Klein et al., 2011).

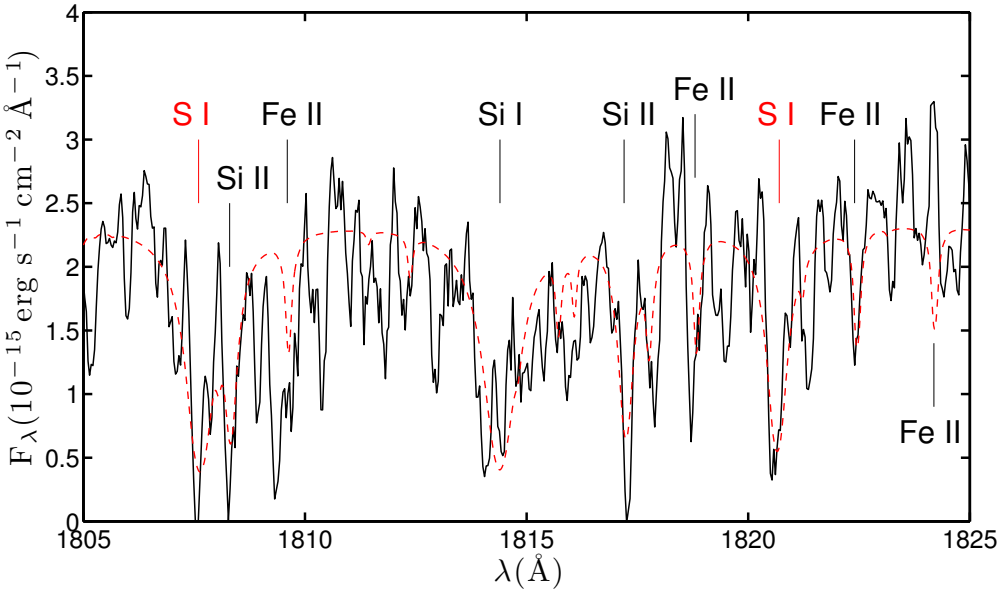

Figure 3.3 HST/COS spectrum of GD 362. All notations are the same as Figure 3.1 and the data are smoothed by a 5 pixel boxcar. S I 1807.3 Å and 1820.3 Å are used for constraining the sulfur abundance.

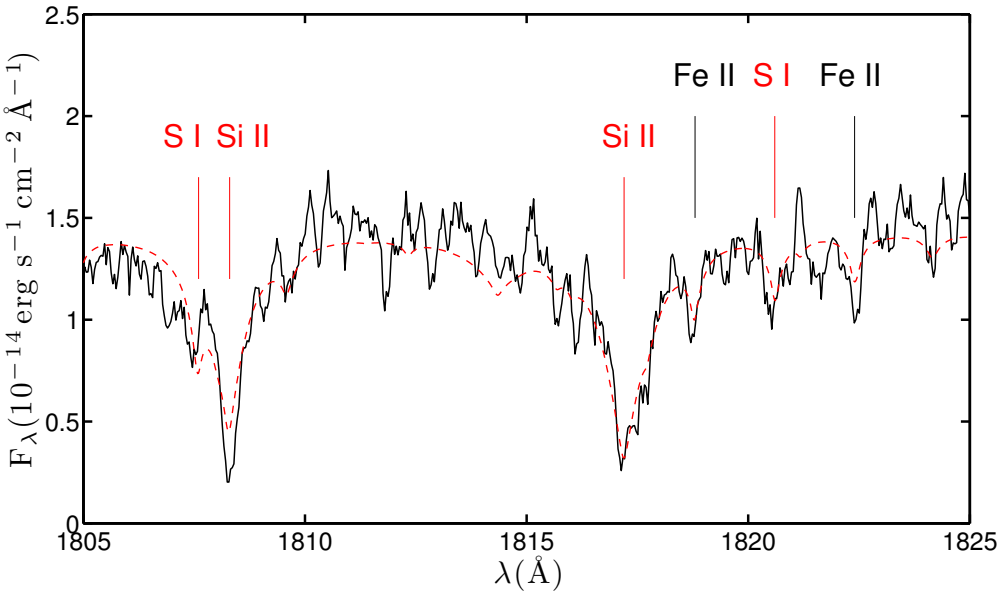

Figure 3.4 Similar to Figure 3.3 except for PG 1225-079. Si II 1808.0 Å and 1816.9 Å lines are used for determining the silicon abundance.

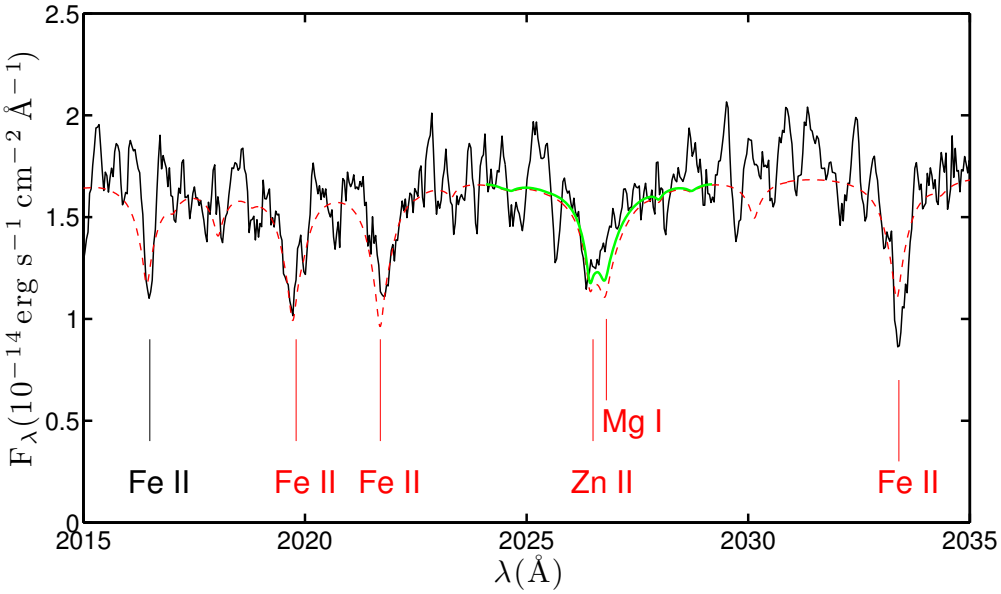

Figure 3.5 HST/COS spectrum of PG 1225-079 and the data are smoothed by a 5 pixel boxcar. All notations are the same as Figure 3.1. Zn II 2026.1 Å and Mg I 2026.5 Å are used for determining the Zn and Mg abundances, respectively. The green line presents the best fit model that matches the overall EW of the absorption feature at 2026 Å ([Mg]/[He] = -7.6, [Zn]/[He] = -11.3); the red line is the adopted model combining with the optical results ([Mg]/[He] = -7.5, [Zn]/[He] = -11.3). Fe II 2019.4 Å, 2021.4 Å, 2033.0 Å and 1926.0 Å in Figure 3.2 are used for determining the iron abundance.

3.3.5 Iron

In the COS data for PG 1225-079, there are six Fe II lines with EWs larger than 100 mÅ. Four of them are shown in Figures 3.2 and 3.5. We derived an iron abundance of -7.45 ± 0.23, in good agreement of the optical value of -7.42 ± 0.07, which is based on 28 high-SNR iron lines (Klein et al., 2011). Because the ultraviolet data are noisier, we adopt the optically-derived iron abundance.

3.4 Comparison with Solar System Objects

Combined with previous data, we now have determined the abundances of 16 elements heavier than helium in the atmosphere of GD 362 and 11 heavy elements in PG 1225-079. However, the measured composition need not be identical to the composition of the accreted planetesimal because different elements gravitationally settle at different rates in a white dwarf atmosphere. Three major phases are proposed for a single accretion event: build-up, steady-state and decay (Dupuis et al., 1993; Koester, 2009).

Because an infrared excess is found for GD 362 and PG 1225-079 (Becklin et al., 2005; Kilic et al., 2005; Farihi et al., 2010b), the accretion should be either in the build-up or steady-state phase. The timescale for build-up stage is comparable to the settling times (Koester, 2009); it is $\sim 10^5$ yr, for GD 362 and PG 1225-079 (see Tables 3.4 and 3.5). The rest of the disk-host stage should all be under the steady-state approximation. The dust disk lifetime has been under intensive studies for a few years but the values are still very uncertain, including 10^5 yr (Farihi et al., 2009; Rafikov, 2011b), 10^6 yr (Rafikov, 2011a; Girven et al., 2012; Farihi et al., 2012b) and up to 10^7 yr (Barber et al., 2012). The true disk lifetime might have a range but it is likely to be longer than the settling times. Furthermore, Zuckerman et al. (2010) suggested that steady-state approximation is the dominant situation for white dwarf accretion event based on a study of helium dominated stars; the settling times are only 0.1% of their cooling times but 30% of them show atmospheric pollution. GD 362 and PG 1225-079 are more likely to be under the steady-state approximation and that is the

main focus of this paper.

In the steady-state model, the observed concentration of an element is dependent on the time it takes to sink out of the convective envelope. To derive the theoretical settling times and obtain an improved understanding of the uncertainties, we formulated several numerical experiments with the code for the envelope structure and corrected two errors found in our previous calculations of diffusion timescales. In the course of changing the equations describing element diffusion from the version in Paquette et al. (1986) (Equation 4) to the one in Pelletier et al. (1986) (Equation 5), which is more accurate in the case of electron degeneracy, one of us (D.K.) discovered an error in the former paper. A factor of $\rho^{1/3}$ is missing in the second alternative of Equation 21, which we had not noticed before. A rederivation of all our equations uncovered another error in our implementation of the contribution of thermal diffusion. These errors have only a very small effect in stars with relatively shallow convection zones, like the hydrogen-dominated white dwarfs. However, for helium-dominated white dwarfs with T < 15,000 K and a deep convection zone, the diffusion timescales can be slower by factors 2-3 relative to our earlier calculations[5]. The accretion rate $\dot{M}(Z_i)$ of an element Z is calculated as (Koester, 2009)

$$\dot{M}(Z_i) = \frac{M_{cvz} X(Z_i)}{t_{set}(Z_i)} \tag{3.1}$$

where M_{cvz} is the mass of the convective envelope. $X(Z_i)$ is the mass fraction of the element Z_i relative to the dominant element in the atmosphere, either hydrogen or helium; $t_{set}(Z_i)$ is the settling time. A longer settling time corresponds to a lower diffusion flux. Fortunately, the relative timescales for different elements, which are important for the determination of the abundances in the accreted matter, change much less.

For GD 362 and PG 1225-079, compared to previously published values, the settling times listed in Tables 3.4 and 3.5 typically increase by factors of 2-3 while the mass of the convective zone is 0.13 dex smaller for GD 362 and 0.05 dex larger for PG 1225-079 (Table 3.3). These corrections lead to smaller total accretion rates by a factor of 3 for both stars.

[5]Updated diffusion timescales can be obtained at http://www.astrophysik.uni-kiel.de/ koester/astrophysics/

The next step is to compare the composition of the accreted parent body with those of solar system objects. We choose the summed mass of all the major elements as the normalization factor so that the analysis is independent of the chemical property and abundance uncertainty of each individual element. However, one complication is that no oxygen lines are detected in either GD 362 or PG 1225-079 due to their low photospheric temperatures relative to other helium-dominated white dwarfs; only upper limits were obtained for this major element. Therefore, our approach is to compare the mass fraction of an element relative to the summed mass of the common elements Mg, Si and Fe. For solar system objects, we include 80 representative and well-analyzed meteorite samples mostly from Nittler et al. (2004). We also include the bulk composition of Earth from Allègre et al. (2001) and an updated carbon abundance from Marty (2012). For our purpose, Earth appears to be chondritic and its bulk composition approaches CV chondrites even though Earth has experienced some post-nebular processing, such as differentiation and collisions.

3.4.1 GD 362: Accretion from a Mesosiderite Analog?

In Figure 3.6, we compare the abundances of all 18 elements, including upper limits, of the accreted material in GD 362 with CI chondrites, which are the most primitive material in the solar system. The composition of CI chondrites is almost identical to the solar photosphere, with the exception of depletion of volatile elements C, N as well as H and noble gases. The parent body accreted onto GD 362 looks nothing like a CI chondrite, as first pointed out in Zuckerman et al. (2007). For the volatile elements, the mass fraction of C and S are depleted by at least a factor of 7 and 3, respectively, relative to CI chondrites; refractory elements, such as V, Ca, Ti and Al, are all enhanced.

Though oxygen is not detected in GD 362, its stringent upper limit can still provide useful insights. Following Klein et al. (2010), we can calculate the required number of oxygen atoms to form oxides $\mathrm{Z}_{p(Z)}\mathrm{O}_{q(Z)}$ as

$$n(O) = \sum_{Z} \frac{q(Z)}{p(Z)} n(Z) \tag{3.2}$$

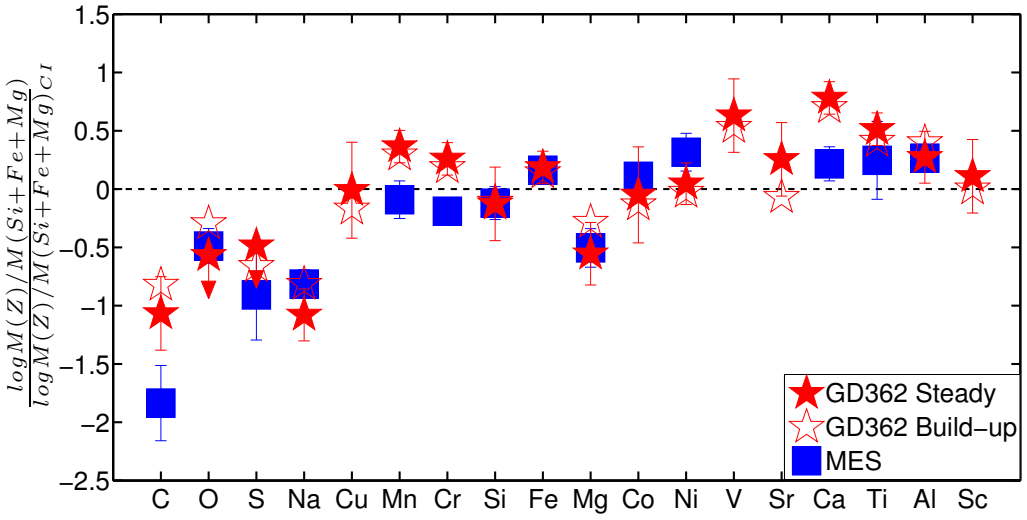

Figure 3.6 Mass fractions of heavy elements in GD 362 with respect to the summed mass of silicon, iron and magnesium from Table 3.4. The abundances are normalized to those of CI chondrites. The elements are ordered by decreasing volatility. The filled stars represent the steady-state approximation while the open stars are in the build-up stage. 1σ error bars and arrows for upper limits are plotted only for the steady-state approximation for clarity. We also plot the average values for five mesosiderites (Emergy, Barea, Patwar, Dyarrl Island and ALH 77219) from Nittler et al. (2004); 1σ deviations are shown as blue error bars. The error bars are smaller than the symbol when they are not visible in the figure. There are no reported whole rock fractions of Cu, V, Sr and Sc in mesosiderites.

Hydrogen is excluded here because GD 362 has an enormous amount and it might not be associated with the parent body or bodies currently in its atmosphere (see Appendix A). Under the steady-state approximation, [O]/[He] = -5.07 is required to form MgO, Al_2O_3, SiO_2 and CaO; this value is comparable to the observed oxygen upper limit of -5.14. However, Fe is the most abundant heavy element in the atmosphere of GD 362 and there is insufficient oxygen to tie it up in either FeO or Fe_2O_3. Thus, most, if not all the iron in the parent body is in metallic form, which is very different from CI chondrites where most iron is in oxides (Nittler et al., 2004).

O'Neill & Palme (2008) suggested that [Mn]/[Na] can be used as an indicator of post-nebular processing. For example, [Mn]/[Na] is -0.79 for all chondrites as well as the solar photosphere while non-chondritic objects have a much higher value. Interestingly, [Mn]/[Na] is 0.65 $\pm$ 0.22 for GD 362, which is larger than -0.01 for Mars and 0.32 for the Moon (O'Neill & Palme, 2008). This suggests that the planetesimal accreted onto GD 362 is likely to be non-chondritic and have experienced some post-nebular processing. Zuckerman et al. (2007) compared the [Na]/[Ca] ratio in GD 362 with solar system objects and reached a similar conclusion; the accreted planetesimal was non-chonridtic. The only other polluted white dwarf with both Mn and Na detections is WD J0738+1835 wherein [Mn]/[Na]= -0.54 $\pm$ 0.19 (Dufour et al., 2012); this agrees with the chondritic value within the uncertainties.

To find the best solar system analog to the parent body accreted onto GD 362, we calculated a reduced chi-squared value for each object in our sample (χ^2_{red}), defined as:

$$\chi^2_{red} = \frac{1}{N} \sum_{i=1}^{N} \frac{(M_{wd}(Z_i) - M_{mtr}(Z_i))^2}{\sigma^2_{wd}(Z_i)} \tag{3.3}$$

where N is the total number of elements considered in the analysis. $M_{wd}(Z_i)$ and $M_{mtr}(Z_i)$ represent the mass fraction of an element Z_i relative to the summed mass of Mg, Si and Fe in the extrasolar planetesimal and solar system objects, respectively. $\sigma_{wd}(Z_i)$ is the propagated uncertainty in mass fraction.

For GD 362, we calculated χ^2_{red} for 11 heavy elements, C, Na, Mg, Al, Si, Ca, Ti, Cr,

Mn, Fe and Ni, which have detections both in GD 362 and the meteorite sample[6]. The results are shown in Figure 3.7 for both steady-state and build-up approximations. There is no qualitative difference between these two models and mesosiderites provide the best fit considering all 11 elements. In particular, the mesosiderite ALH 77219 can match the overall abundance pattern to 95% confidence level. As shown in Figure 3.6, the abundance of individual elements agrees within 2σ between mesosiderites and the planetesimal accreted onto GD 362.

Mesosiderites are a rare type of stoney-iron meteorite with equal amounts of silicates and metallic iron and nickel. One mystery about mesosiderties is that the Si-rich crust and Fe, Ni-rich core materials are abundant but the olivine Mg-rich mantle seems to be missing. One model for the formation of mesosiderites is that a 200-400 km diameter asteroid with a molten core was nearly catastrophically disrupted by a 50-150 km diameter projectile at 4.42-4.52 Gyr ago (Scott et al., 2001). The collision mixed the target's molten core with its crustal material but excluded the large and hot mantle fragments. The planetesimal accreted onto GD 362 may have been formed in a similar way.

While mesosiderites may be a prototype for the accreted planetesimal onto GD 362, there are three major hurdles for this hypothesis to overcome. First, in the model of Scott et al. (2001), only half of the original mass of a 200-400 km diameter asteroid was maintained after the collision and the final product only contains about 10% mesosiderite-like material by mass. This is equivalent to a 75-150 km diameter object. Mesosiderites that fall on Earth are only small fragments and the 180 kg NWA 2924 is among the largest (Meteorite Bulletin Database[7]). However, the parent body accreted onto GD 362 has a minimum mass of 2.7 $\times$ 10^{22} g, $\sim$260 km in diameter for an assumed density of 3 g cm^{-3}. It is unclear whether the same kind of collision can produce a mesosiderite parent body this big. Second, the mass fraction of hydrogen in mesosiderites is less than 0.2%; it cannot explain how there is 5 $\times$ 10^{24} g hydrogen in the atmosphere of GD 362. Possibly, hydrogen was accreted during earlier events and it has been atop the atmosphere ever since (see Appendix A for

[6]For a couple of meteorites with no reported carbon abundance, we compute the χ^2_{red} for the other 10 elements.

[7]http://www.lpi.usra.edu/meteor/

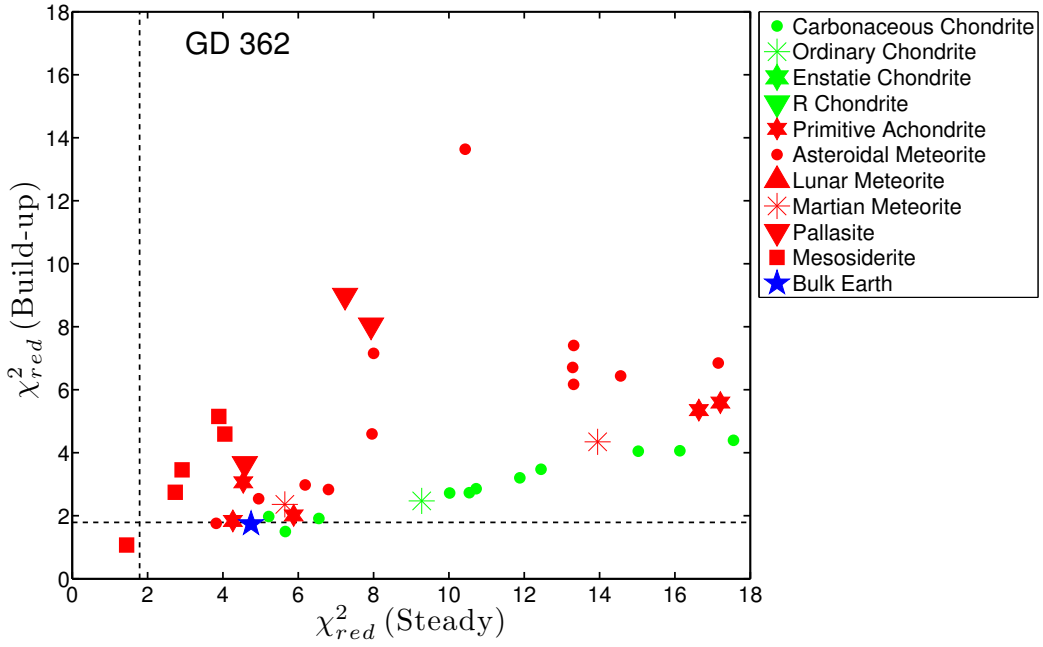

Figure 3.7 This figure shows χ^2_{red} values defined in Equation (3), which compares the abundances of C, Na, Mg, Al, Si, Ca, Ti, Cr, Mn, Fe and Ni in the accreted material in GD 362 with 80 meteorites and bulk Earth. The x-axis denotes χ^2_{red} calculated for the composition under the steady-state approximation while the y-axis is for the build-up phase. The dashed lines represent 95% confidence level. There are a couple of meteorites with a large χ^2_{red} and they are not shown in the current scale. There is no qualitative difference between the steady-state and build-up models. Mesosiderites, particularly ALH 77219, provide the best fit to the abundance pattern observed in GD 362. Notes: "Chondritic" materials include: (i) carbonaceous chondrites: CI, CK, CM, CO, CR and CV; (ii) ordinary chondrites: H, L and LL; (iii) enstatite chondrites: EH and EL; (iv) R chondrite. "Non-chondritic" materials consist of achondrites and stoney-iron meteorites. No iron meteorite is included in our analysis because their bulk composition is dominated by Fe and Ni, with very few trace elements reported. Achondrites include: (i) primitive achondrites: acapulcoites, lodranites, winonaites and ureilites; (ii) asteroidal meteorites: angrites, aubrites, brachinites and howardite-eucrite-diogenite; (iii) Martian meteorites: shergottie, Nakhlites and Chassignites; (iv) Lunar meteorites. For stoney-iron meteorites, we include (i) mesosiderites; (ii) pallasites. Most of the meteorite data are from Nittler et al. (2004) and the compositions for some Martian meteorites are from McSween (1985). The bulk composition of Earth is from Allègre et al. (2001) and the carbon abundance is from a more recent study of Marty (2012), which is a factor of 3 lower than the lower limit reported in Allègre et al. (2001).

more discussion). Third, GD 362 is currently accreting from its circumstellar disk and the disk material should also resemble the composition of mesosiderites. However, the shape of the mid-infrared spectrum for mesosiderite, which is dominated by a sharp peak at 9.13 μm and several other bands at 10.6 μm and 11.3 μm (Morlok et al., 2012), cannot fully account for the broad 10 μm silicate emission feature observed for GD 362 (Jura et al., 2007b). This does not completely exclude the mesosiderite hypothesis but emission from some additional material is required to fully reproduce the observed infrared spectrum for GD 362. Mesosiderites are a good candidate for the parent body accreted onto GD 362 but there are remaining unresolved issues.

3.4.2 PG 1225-079: Accretion from a Planetesimal with No Single Solar System Analog

In Figure 3.8, we show a comparison of the mass fractions of 16 elements, including upper limits between PG 1225-079 and CI chondrites. Though the carbon abundance is approaching the chondritic value, the accreted planetesimal differs a lot from CI chondrites; the mass fraction of S is depleted by at least a factor of 40 while Zn is depleted by at least a factor of 8. In contrast, refractories, such as V, Ca, Ti and Sc are all enhanced. The overall pattern of relatively high carbon abundance and enhanced mass fractions of refractory elements does not follow a single condensation sequence and post-nebular processing is required.

As shown in Figure 3.9, PG 1225-079 has a [C]/[S] value that is no smaller than the solar ratio, which is very different from other polluted white dwarfs and meteorites. Carbon and sulfur are among the most volatile elements that we can measure and their 50% condensation temperatures are 40 K and 655 K, respectively (Lodders, 2003). Most of the meteorites as well as polluted white dwarfs have a [C]/[S] ratio lower than the solar value, which can be explained by condensation at a temperature between 40 and 665 K though this is not necessarily true for all of them. The only solar system analog to PG 1225-079 with similar high carbon, low sulfur pattern is ureilites, a type of primitive achondrites. Ureilites are the second largest achondrite group and it is suggested that its high carbon abundance is derived

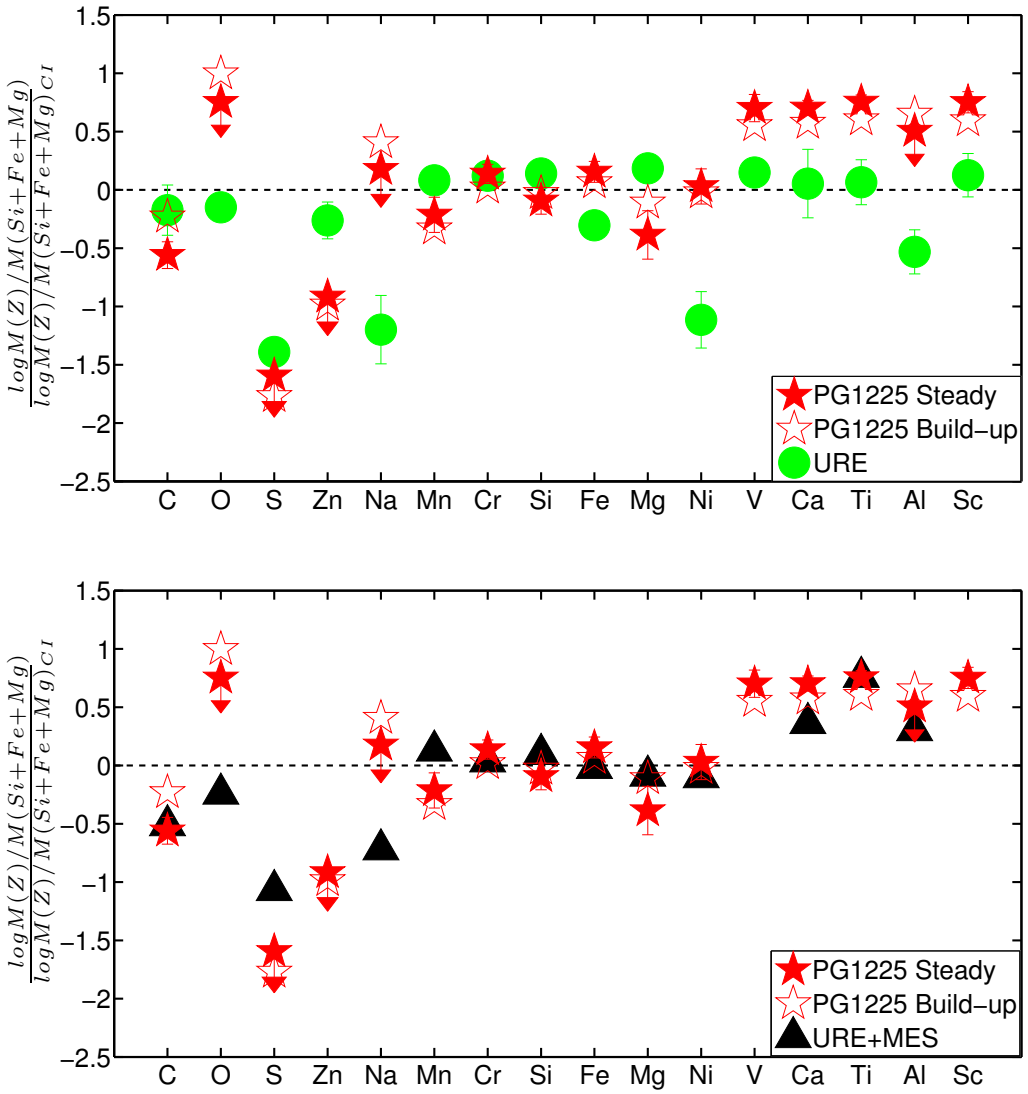

Figure 3.8 Upper panel: similar to Figure 3.6 except for PG 1225-079 with the abundances in Table 3.5. Ureilites can match the high carbon low sulfur pattern in PG 1225-079 but fail with the other elements. The abundances for ureilites are from Warren et al. (2006). Low panel: the best-fit model for the composition in PG 1225-069 under the steady-state approximation is 30% by mass ureilite North Haig and 70% mesosiderite Dyarrl Island. There are no reported bulk compositions of Zn, V or Sc for the North Haig and Dyarrl Island meteorites.

from a carbon-rich parent body, but the exact formation mechanism is not well understood (Goodrich, 1992). However, as can be seen in Figure 3.8(a), ureilites fail to match the overall composition of the parent body accreted onto PG 1225-079.

We performed a χ^2_{red} analysis between solar system objects and the accreted planetesimal in PG 1225-079, comparing 9 elements, C, Mg, Si, Ca, Ti, Cr, Mn, Fe and Ni[8]. The result is shown in Figure 3.10. There is no single solar system object that can match all nine elements; the closest is carbonaceous chondrite. Regardless, as shown in Figure 3.8, the accreted abundance in PG 1225-079 is not at all identical to CI chondrites.

The infrared excess around PG 1225-079 corresponds to ∼500 K dust (Farihi et al., 2010b); so far, only two white dwarfs are known to have such cool dust. The other 28 known disk-host stars all have ∼1000 K dust (Xu & Jura, 2012). One hypothesis is that the inner disk region was recently impacted by another asteroid and all the material was dissipated (Farihi et al., 2010b; Jura, 2008). If that is the case, PG 1225-079 can be accreting from a blend of two planetesimals, rather than one single parent body. After testing different combinations of the 80 meteorites in our database, the best fit model to the steady-state approximation consists of 30% ureilite North Haig and 70% mesosiderite Dyarrl Island by mass. This blend is also marked in Figure 3.10. Detailed abundance comparison is shown in Figure 3.8(b); the abundances of S, Mn and Ca do not agree as well as the other elements but are all within 2σ. A possible scenario is that one extrasolar ureilite (mesosiderite) analog first got tidally disrupted and more recently, another mesosiderite (ureilite) analog impacted the disk and was blended with the previous material.

3.5 Assessing the Formation Mechanisms of Extrasolar Planetesimals

Having established that the parent bodies accreted onto GD 362 and PG 1225-079 are beyond primitive, we now extend our analysis to other extrasolar planetesimals. We are

[8]Similar to the case of GD 362, for the meteorites with no reported carbon abundance, we only calculated χ^2_{red} for the other 8 elements.

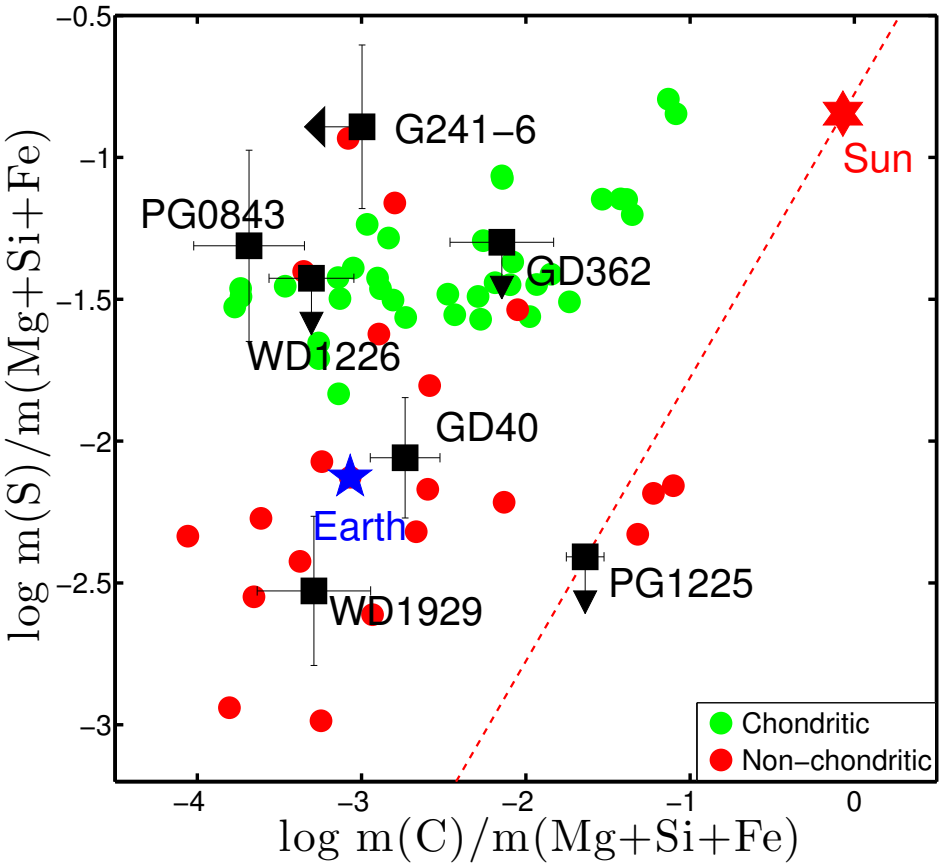

Figure 3.9 Mass fraction of S and C over the sum of Fe, Mg and Si for solar system objects as well as polluted white dwarfs with positive detection of carbon or sulfur or both. Due to the presence of an infrared excess except for G241-6 (see discussion in Appendix B), all white dwarfs are plotted under the steady-state approximation . 1σ uncertainties are plotted. The red dashed line denotes constant solar [C]/[S]. Most meteorites have a lower [C]/[S] than the solar value. However, [C]/[S] in PG 1225-079 is no smaller than solar and the closest solar system analog is ureilites. References: WD 1929+012, PG 0843+517, WD 1226+110: Gänsicke et al. (2012); GD 40, G241-6: Jura et al. (2012); GD 362 and PG 1225-079: this paper; Solar abundance: Lodders (2003); for solar system objects, the references are listed in the caption of Figure 3.7.

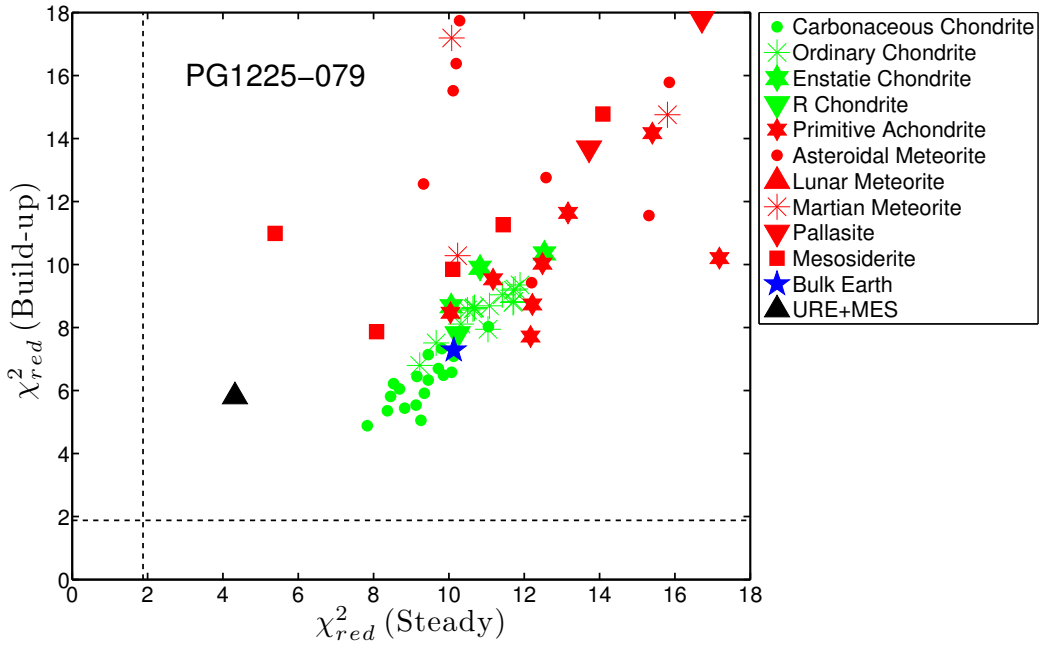

Figure 3.10 Similar to Figure 3.7 except for PG 1225-079 comparing 9 elements, C, Mg, Si, Ca, Ti, Cr, Mn, Fe and Ni. We see that no solar system object comes close to the overall abundance pattern in PG 1225-079. The black triangle represents 30% by mass ureilite and 70% mesosiderite as shown in Figure 3.8(b), which is the best match for the composition of PG 1225-079 in the steady-state approximation.

most interested in understanding the formation mechanisms of extrasolar planetesimals and whether these are dominated by nebular or post-nebular processing. Jura & Xu (2013) suggested collisional rearrangement is important in determining the final composition of extrasolar planetesimals based on the scatter in [Mg]/[Ca] ratios in 60 externally-polluted white dwarfs. Here, we compile a sample of well-studied externally-polluted white dwarfs with abundance determinations of at least 9 elements. There are 9 stars in total, as listed in Table 3.6 and now we assess the formation mechanism for individual objects.

GD 40: As discussed in Jura et al. (2012) and Appendix B, the overall abundance pattern in GD 40 matches with carbonaceous chondrites and bulk Earth. Nebular condensation is sufficient to explain its observed composition.

WD J0738+1835: Dufour et al. (2012) found that there is a correlation between the abundance of an element and its condensation temperature: refractory elements are depleted while volatile elements are enhanced compared to bulk Earth. This indicates that the accreted planetesimal might be formed in a low temperature environment under nebular condensation.

PG 0843+517: This star has the highest mass fraction of iron among all polluted white dwarfs. Gänsicke et al. (2012) found that all core elements, including Fe, Ni, S and Cr are enhanced relative to the values for bulk Earth while lithophile refractory Al is depleted. This star might be accreting from the core of a differentiated object. Nevertheless, considering the uncertainty for each element is at least 0.2 dex, the conclusion is still preliminary.

PG 1225-079: As discussed in section 4.2, this star has a near chondritic carbon abundance but also enhanced mass fractions of refractory elements relative to CI chondrite; it cannot be formed solely under nebular processing.

NLTT 43806: Compared to chondritic values, the accreted planetesimal is depleted in Fe and enhanced in Al. Zuckerman et al. (2011) found that the best fit model corresponds to "30% crust 70% upper mantle". With detections of 9 elements, evidence is strong that NLTT 43806 has accreted the outer layer of a differentiated parent body.

Table 3.6 Summary of Planetesimal Formation Mechanisms in 9 Well-Studied White Dwarfs

star	Dom.	Dust	Volatile	Intermediate	Refractory	Process	Ref
GD 40	He	Y	C,S:,O,Mn, P	Cr,Si,Fe,Mg,Ni	Ca,Ti,Al	primitive	1,2
WD J0738+1835	He	Y	O,Na,Mn	Cr,Si,Fe,Mg,Co,Ni	V,Ca,Ti,Al,Sc	primitive	3,4
PG 0843+517	H	Y	C,S,O,P	Cr,Si,Fe,Mg,Ni	Al	beyond-primitive(?)	5
PG 1225-079	He	Y	C,Mn	Cr,Si,Fe,Mg,Ni	V,Ca,Ti,Sc	beyond-primitive	6,7
NLTT 43806	H	N	Na	Cr,Si,Fe,Mg,Ni	Ca,Ti,Al	beyond-primitive	8
GD 362	He	Y	C,Na,Cu,Mn	Cr,Si,Fe,Mg,Co,Ni	V,Sr,Ca,Ti,Al,Sc	beyond-primitive	7,9
WD 1929+012	H	Y	C,S,O,Mn,P	Cr,Si,Fe,Mg,Ni	Ca,Al	???	5,10,11,12
G241-6	He	N	S,O,Mn,P	Cr,Si,Fe,Mg,Ni	Ca,Ti	primitive	2,6,13
HS 2253+8023	He	N	O,Mn	Cr,Si,Fe,Mg,Ni:	Ca,Ti	primitive	6

Note. This is a compiled sample of externally polluted white dwarfs with detections of at least 9 elements heavier than helium. Columns are defined as follows. "Dom" lists the dominant element in the atmosphere. "Dust" indicates whether a star has an infrared excess ("Y") or not ("N"). Following the classification scheme in Lodders (2003), "Volatile" lists the detected volatile elements, defined as having a 50% condensation temperature lower than 1290 K in a solar-system composition gas (Lodders, 2003); "Intermediate" lists the elements with a condensation temperature between 1290-1360 K –the same range as that of the common elements, Si, Fe and Mg; "Refractory" elements have a 50% condensation temperature higher than 1360 K. The elements are ordered with increasing condensation temperature. "Process" shows our proposed dominant mechanism that determines the final composition of the accreted extrasolar planetesimal (see section 5).

References. (1) Klein et al. (2010); (2) Jura et al. (2012); (3) Dufour et al. (2010); (4) Dufour et al. (2012); (5) Gänsicke et al. (2012); (6) Klein et al. (2011); (7) this paper; (8) Zuckerman et al. (2011); (9) Zuckerman et al. (2007); (10) Vennes et al. (2010); (11) Vennes et al. (2011); (12) Melis et al. (2011); (13) Zuckerman et al. (2010).

GD 362: As discussed in section 4.1, mesosiderite is the best solar system analog to the accreted parent body and post-nebular processing is required.

WD 1929+012: Gänsicke et al. (2012) showed that this star has a high iron content. However, the situation is perplexing in that different analyses yield different stellar parameters and atmospheric abundances. For example, both Melis et al. (2011) and Gänsicke et al. (2012) derived that [Si]/[Fe] is -0.25 but Vennes et al. (2010) found that [Si]/[Fe] is 0.19. No final conclusion can be drawn before resolving such discrepancies.

G241-6: This star is a near twin of GD 40 with a similar abundance pattern but without an infrared excess. One possible scenario is that G241-6 has accreted a planetesimal with a similar composition to GD 40 and now it is at the beginning of a decaying phase; all heavier elements appear to be depleted relative to GD 40 due to their short settling times (Klein et al., 2011; Jura et al., 2012). As discussed in Jura et al. (2012) and Appendix B, the overall abundances resemble those of chondrites and no post-nebular processing is required.

HS 2253+8023: Klein et al. (2011) showed that the composition of its parent body agrees with bulk Earth, except for the enhanced calcium abundance. Nebular processing can produce the observed abundance pattern.

As summarized in Table 3.6, at least 4 out of the 9 white dwarfs have accreted planetesimals that can be formed under nebular processing while post-nebular processing is required for another 3 of them. It should be noted that some objects that we identify as primitive might still have undergone some post-nebular processing. For example, GD 40 has accreted from a planetesimal that has a similar composition as bulk Earth, whose overall abundance pattern is chondritic. However, it is still possible that the parent body was differentiated; when the entire object is accreted, the composition appears to be "chondritic". We can only put an upper limit on the number of objects formed under nebular condensation.

From this sample of 9 stars, we see that post-nebular processing appears to play an important role in determining the final abundance of extrasolar planetesimals; beyond-primitive planetesimals might be as common as primitive planetesimals. In contrast, chondrites comprise more than 90% of all meteorites found on Earth by number (Meteorite

Bulletin Database[9]). Possibly, extrasolar planetesimals around white dwarfs have violent evolutionary histories with more collisions. This difference is not surprising since dynamical rearrangement of planetary systems at white dwarfs is expected to increase the frequency of collisions and produce more beyond-primitive extrasolar planetesimals.

So far, 19 elements heavier than helium, including C, S, O, Na, Cu, Mn, P, Cr, Si, Mg, Fe, Co, Ni, V, Sr, Ca, Ti, Al and Sc, have been detected in the atmospheres of polluted white dwarfs, as shown in Table 3.6. In terms of mass fraction in the accreted planetesimal, the lowest limit is $\sim$5 ppm, for Sc in WD J0738+1835 (Dufour et al., 2012). Studying externally-polluted white dwarfs proves to be a very sensitive probe of the bulk compositions of extrasolar planetesimals.

3.6 Conclusions

We present HST/COS ultraviolet observations for GD 362 and PG 1225-079, two heavily polluted helium white dwarfs. In GD 362, the mass fractions of carbon and sulfur are depleted by at least a factor of 7 and 3 respectively, compared to CI chondrites. In PG 1225-079, a similar volatile depletion pattern is found: C by a factor of 2, S by at least a factor of 40 and Zn by at least a factor of 8. We provide good evidence for the presence of beyond-primitive extrasolar planetesimals:

1. Mesosiderites provide a good match to the composition of the parent body accreted onto GD 362. However, there are several unresolved issues for this hypothesis, especially the apparent difference between the mid-infrared spectrum of mesosiderites and the dust disk around GD 362. Additional material is required.

2. No single meteorite can reproduce the abundance pattern in PG 1225-079. A blend of 30% North Haig ureilite and 70% Dyarrl Island mesosiderite can provide a good fit to the overall composition.

[9]http://www.lpi.usra.edu/meteor/

3. Spectroscopic observations of externally-polluted white dwarfs enable sensitive measurement of the bulk compositions of extrasolar planetesimals, including 19 heavy elements down to a mass fraction of 5 ppm. Based on a sample of 9 well-studied white dwarfs, we find that post-nebular processing is as important as nebular condensation in determining the compositions of extrasolar planetesimals.

3.7 APPENDIX: The Herschel/PACS Observation of GD 362

While hydrogen is detected in some helium-dominated white dwarfs (Voss et al., 2007), GD 362 has an anomalously large amount. The helium-to-hydrogen number ratio is 14 in its convective zone, corresponding to 5×10^{24} g of hydrogen; this is lower than 7×10^{24} g reported in Jura et al. (2009b) because the mass of the convective zone for GD 362 is 0.13 dex lower in the updated calculation (Table 3.3). The origin of the hydrogen is a mystery. Unlike heavy elements which have short settling times compared to the white dwarf cooling age, hydrogen never sinks and can be accumulated over the entire cooling history of the star (Bergeron et al., 2011; Jura & Xu, 2012). If GD 362 has always been a helium-dominated white dwarf and all this hydrogen is from accretion of tidally disrupted objects, it can either be one Callisto-size object or $\sim$100 Ceres-like asteroids (Jura et al., 2009b). In the latter case, likely there would be many more asteroids orbiting the star and mutual collisions among them would generate a cloud of cold dust.

We were awarded 1.1 hours of Herschel/PACS (Poglitsch et al., 2010) observation time to look for cold dust around GD 362. The "mini-scan map" mode was used to observe in "blue" (85-125 μm) and "red" (125-210 μm) bands simultaneously with a medium scan speed of $20''$ s^{-1} and a scan leg length of $4'$. The scan map size is $345'' \times 374''$ and the repetition number is 25. Two different scan angles, 45 degrees and 135 degrees were used and the total integration time was 1200 sec.

Data reduction was performed using HIPE (Herschel Interactive Processing Environment) on a combined mosaic of level 2 products from pipeline SPG 7.1.0. The pixel scale is $1''$ pixel^{-1} and $2''$ pixel^{-1} for the blue and red band, respectively. Correcting for its proper

motion, we expect GD 362 at α = 17:31:34.355, δ = +37:05:18.331 on the date of the observation. Because there is no detection, aperture photometry was performed at 25 locations within 5 pixels of the nominal position of GD 362. The aperture radius was 20″ with a sky annulus between 61″ and 70″. The background intensity was estimated using the median sky estimation algorithm (Herschel Data Analysis Guide[10]). Aperture correction factors are 0.949 for blue and 0.897 for red (PACS Observer's Manual[11]). Based on the dispersion of the 25 measurements, 3σ upper limits are 5.1 mJy for blue and 5.6 mJy for red.

What does this imply about dust mass? GD 362 has shrunk in mass from 3 $M_\odot$ on the main-sequence to its current mass of 0.72 $M_\odot$ (Kilic et al., 2008b). Consequently, asteroids initially at 3-5 AU are now orbiting at 13-21 AU. Currently, GD 362 has a stellar temperature of 10,540 K and cooling age $\sim$ 0.9 Gyr (Farihi et al., 2009). Extrapolating from white dwarf cooling models[12] (Bergeron et al., 2011), for GD 362, its stellar temperature is lower than 20,000 K for 90% of its cooling time. We approximate the stellar luminosity as a time-averaged luminosity of 0.01 $L_\odot$. Poynting-Robertson drag was able to remove particles smaller than 20 μm at a distance of 15 AU for a grain density of 3 g cm^{-3}. We therefore assume a dust particle radius of 20 μm in the putative asteroid belt orbiting GD 362.

If the grains function as blackbodies with negligible albedo, then their temperature can be calculated as

$$T_d = T_* \sqrt{\frac{R_*}{2D_{orb}}} \tag{3.4}$$

T_*, R_* are the stellar temperature and radius; D_{orb} is the orbital distance. The dust temperature is 14-11 K between 13-21 AU.

The mass of the dust disk is

$$M_d = \frac{F_\nu D_*^2}{\chi B_\nu(T)} \tag{3.5}$$

[10]http://herschel.esac.esa.int/hcss-doc-8.0/print/howtos/howtos.pdf
[11]http://herschel.esac.esa.int/Docs/PACS/pdf/pacs_om.pdf
[12]http://www.astro.umontreal.ca/ bergeron/CoolingModels/

where D_* is the distance to GD 362, 51 pc (Kilic et al., 2008b) and χ is the dust opacity. For a particle radius of 20 μm, $\chi = 100$ cm^2 g^{-1} in the geometric optics limit. As shown in Figure 3.11, the upper limit of dust mass is between 10^{25} g and 10^{26} g at 13-21 AU; this mass is at least twice the hydrogen mass in the atmosphere of GD 362 and one order of magnitude larger than the mass of solar system's asteroid belt (Krasinsky et al., 2002). The upper limit is not stringent enough to rule out the hypothesis that hydrogen in GD 362 is from accretion of multiple asteroids. So, the large hydrogen abundance in GD 362 remains an unsolved puzzle.

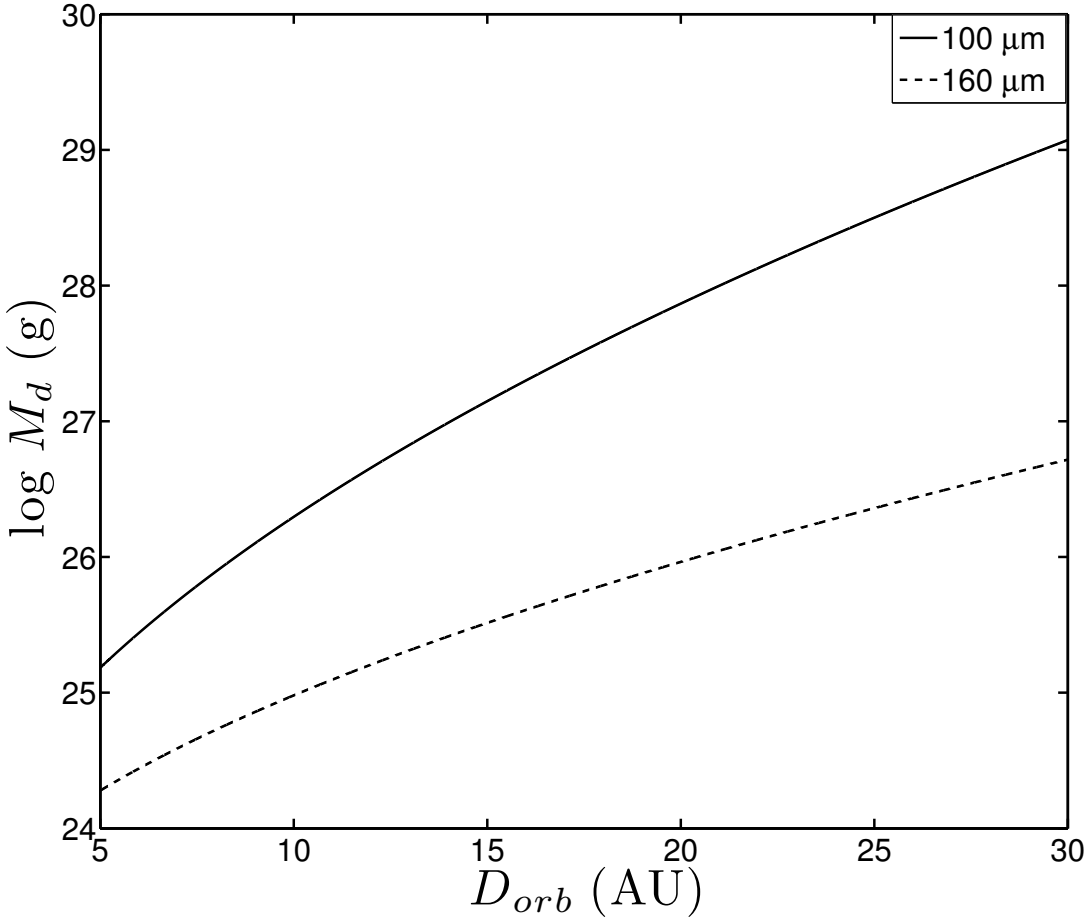

Figure 3.11 Upper limit for the mass of cold dust around GD 362 derived from PACS blue and red data, as a function of orbital radius. Given the hydrogen mass of 5×10^{24} g, the upper limit of dust mass 10^{25}-10^{26} g at 13-21 AU is not stringent enough to rule out the accretion of multiple asteroids.

3.8 APPENDIX: Looking for Solar System Analogs to Extrasolar Planetesimals

The χ^2_{red} analysis has proven to be an effective way to look for solar system analogs to the compositions of extrasolar planetesimals. Two other helium-dominated white dwarfs have reported volatile and refractory abundances from high-resolution optical and ultraviolet observations that are suitable for this kind of analysis[13] – GD 40 and G241-6. Updated settling times and accretion rates are listed in Table 3.7 while the mass of the convective zone stays the same. Since all the major elements are determined, we compare the mass fraction of an element relative to the sum of O, Mg, Si and Fe.

Table 3.7 Updated Settling Times and Accretion Rates for GD 40 and G241-6

Z	t_{set}[a] (10^6 yr)	$\dot{M}(Z)_{GD40}$ (g s^{-1})	$\dot{M}(Z)_{G241-6}$ (g s^{-1})
C	1.1	2.2×10^6	$< 4.4 \times 10^5$
N	1.1	$< 2.6 \times 10^5$	$< 2.1 \times 10^5$
O	1.1	4.5×10^8	4.3×10^8
Mg	1.2	1.7×10^8	1.5×10^8
Al	1.2	1.4×10^7	$< 6.1 \times 10^6$
Si	1.0	1.3×10^8	8.7×10^7
P	0.79	1.1×10^6	4.7×10^5
S	0.64	1.0×10^7:	5.6×10^7
Cl	0.51	$< 8.0 \times 10^5$	$< 5.8 \times 10^5$
Ca	0.51	1.3×10^8	5.1×10^7
Ti	0.49	3.2×10^6	1.4×10^6
Cr	0.53	6.4×10^6	4.5×10^6
Mn	0.53	3.1×10^6	2.4×10^6
Fe	0.56	4.4×10^8	2.0×10^8
Ni	0.61	1.8×10^7	8.9×10^6
Cu	0.58	$< 1.8 \times 10^5$	$< 1.8 \times 10^5$
Ga	0.50	$< 2.9 \times 10^4$	$< 2.9 \times 10^4$
Ge	0.43	$< 1.4 \times 10^5$	$< 1.4 \times 10^5$
Total		1.4×10^9	9.9×10^8

[a] This column is for both GD 40 and G241-6 because their atmospheric conditions are similar.

[13] GD 61 also has high-resolution optical and ultraviolet observations (Desharnais et al., 2008; Farihi et al., 2011). However, with a total of 5 detected elements, it is hard to make a comparison using the χ^2_{red} analysis.

The total accretion rate for GD 40 is a factor of 2 lower than the value derived in Klein et al. (2010), but the relative abundances change much less. The result of a χ^2_{red} analysis is presented in Figure 3.12. When including all 13 detected elements, both carbonaceous chondrites and bulk Earth can match the composition to 95% confidence level for both steady-state and build-up approximations. The accreted planetesimal appears to be primitive and can be formed under nebular condensation, similar to what was concluded by Jura et al. (2012).

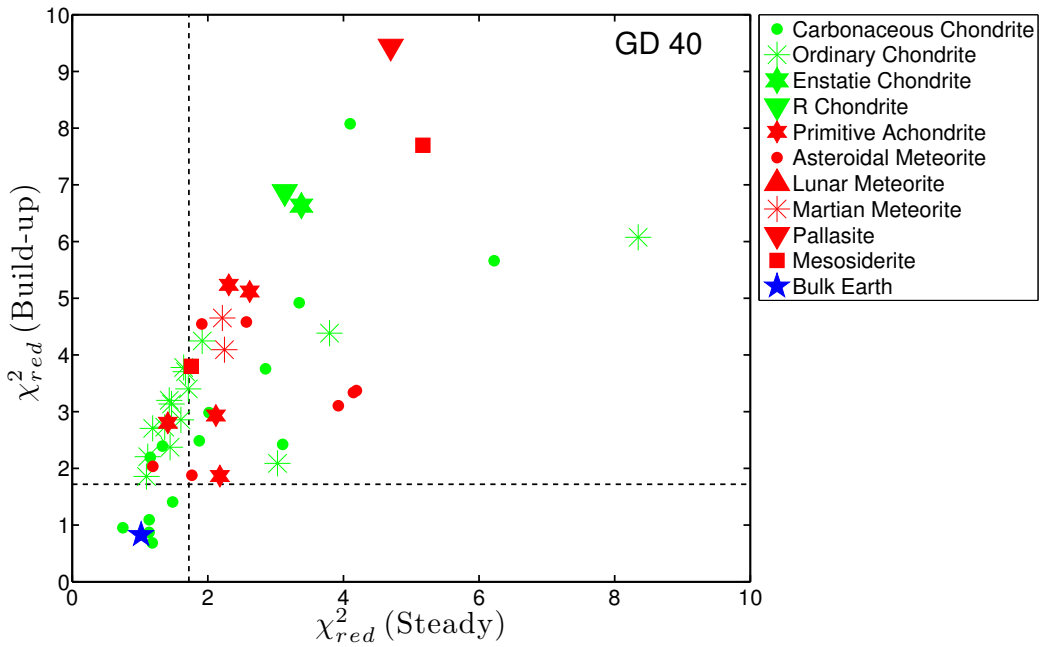

Figure 3.12 Similar to Figure 3.7 except for GD 40 comparing the mass fraction of 13 elements, including C, O, Mg, Al, Si, P, S, Ca, Ti, Cr, Mn, Fe and Ni, relative to the sum of Mg, Si, Fe and O. Both carbonaceous chondrites and bulk Earth are a good match to the parent body accreted onto GD 40.

The newly-derived total accretion rate for G241-6 is about a factor of 2 lower than previously reported (Zuckerman et al., 2010). The non-detection of an infrared excess and the slight depletion of heavier elements suggest that it may be at the beginning of a decay phase (Xu & Jura, 2012; Klein et al., 2011). We assess both steady-state and decay phase for the χ^2_{red} analysis; in the latter case, we assume that accretion stopped 0.6×10^6 yr ago, approximately one settling time for Fe because its mass fraction is depleted by a factor

of 2 relative to CI chondrites. The composition of the parent body is calculated following Zuckerman et al. (2011) and Equation (5) in Koester (2009). A fuller exploration of different time-varying models will be presented in the future in the spirit of Jura & Xu (2012). As shown in Figure 3.13, both carbonaceous chondrites and ordinary chondrites provide good matches to all 11 elements, including O, Mg, Si, P, S, Ca, Ti, Cr, Mn, Fe and Ni. However, the carbon upper limit in G241-6, which is not included in the χ^2_{red} analysis, is at least one order of magnitude lower than most carbonaceous chondrites (Jura et al., 2012). Thus, ordinary chondrites are a more promising solar system analog to the parent body accreted onto G241-6 and nebular condensation is sufficient to produce the observed abundance pattern.

The χ^2_{red} analysis for GD 40 and G241-6 confirms the previous results (Jura et al., 2012); the accreted extrasolar planetesimals can be formed under nebular condensation and their compositions resemble primitive chondrites in the solar system.

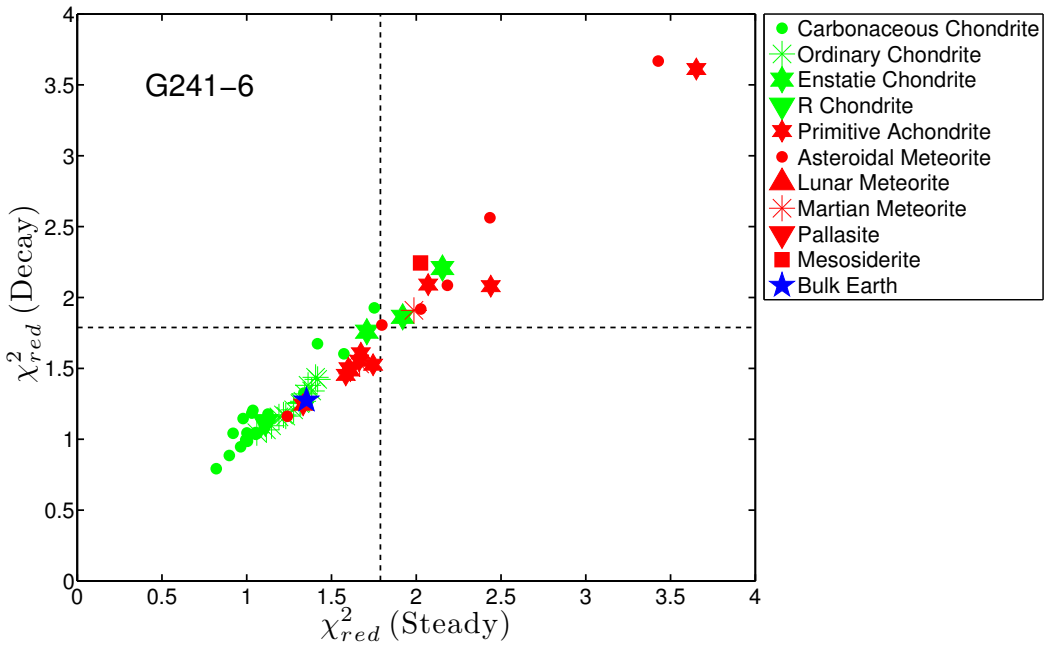

Figure 3.13 Similar to Figure 3.12 except for G241-6 comparing 11 elements – O, Mg, Si, P, S, Ca, Ti, Cr, Mn, Fe and Ni for steady-state versus decay phase when the accretion stopped 0.6×10^6 yr ago. Both carbonaceous chondrites and ordinary chondrites produce a good fit to the parent body accreted onto G241-6. Ordinary chondrites are a relatively better match because of the low carbon abundance, which is not considered in this χ^2_{red} plot because only an upper limit was reported for G241-6 (Jura et al., 2012).

CHAPTER 4

Elemental Compositions of Two Extrasolar Rocky Planetesimals

Reproduced by permission of the AAS (Xu, S., Jura, M.,Koester, D., Klein, B., & Zuckerman, B., 2014, Astrophysical Journal, 783, 79).

4.1 Introduction

Based upon models of planet formation, we understand the variety of elemental compositions of planetesimals as a familiar three step process (McSween & Huss, 2010). (i) Under nebular condensation, incorporation of an element into the planetesimal is a function of local temperature and pressure. (ii) Differentiation often occurs, redistributing all elements within the planetesimal; lithophile elements (Al, Ca, Ti) are enhanced in the crust while siderophile elements (Fe, Mn, Cr, Ni) settle into the core. (iii) Collisions lead to stripping and blending of cores and crust, redistributing elements within the entire planetary system. In the solar system, chondrites are a direct consequence of nebular condensation, i.e. step (i); achondrites and primitive achondrites have experienced post-nebular processing, i.e. steps (ii) and (iii) (O'Neill & Palme, 2008). The study of externally-polluted white dwarfs provides invaluable information about the elemental compositions of extrasolar rocky planetesimals, directly testing these models and contrasting with solar system objects (Jura, 2013; Jura & Young, 2014).

The current picture is that beyond a few AUs, a large fraction of extrasolar planetesimals can survive to the white dwarf phase (Jura, 2008). From dynamical rearrangement during the post-AGB phase, some planetesimals can be perturbed into the tidal radius of the white dwarf

and subsequently "pollute" its pure hydrogen or helium atmosphere (Debes & Sigurdsson, 2002; Jura, 2003; Bonsor et al., 2011; Debes et al., 2012b; Veras et al., 2013). Calcium, the most easily detected element from optical surveys, has been identified in over 200 white dwarfs (Zuckerman et al., 2003, 2010; Koester et al., 2005a; Dufour et al., 2007; Koester et al., 2011). So far, 30 heavily polluted white dwarfs have been found to show excess infrared radiation coming from the debris of these pulverized planetesimals [e.g. Mullally et al. (2007); Farihi et al. (2009); Xu & Jura (2012), and references therein]. These stars always show 10 μm circumstellar silicate emission features when observed spectroscopically (Reach et al., 2005, 2009; Jura et al., 2009a). Orbiting gaseous material has been detected in 9 polluted white dwarfs (Gänsicke et al., 2006, 2007, 2008; Gänsicke, 2011; Gänsicke et al., 2012; Melis et al., 2010, 2012; Farihi et al., 2012a; Debes et al., 2012a). With high-resolution spectroscopic observations, 19 heavy elements have been detected in white dwarf atmospheres, including C, O, Na, Mg, Al, Si, P, S, Ca, Sc, Ti, V, Cr, Mn, Fe, Co, Ni, Cu and Sr (Zuckerman et al., 2007; Klein et al., 2010, 2011; Dufour et al., 2010, 2012; Farihi et al., 2010b; Melis et al., 2010; Vennes et al., 2010, 2011; Zuckerman et al., 2011; Jura et al., 2012; Gänsicke et al., 2012; Xu et al., 2013a).

Theoretical calculations show that extrasolar planetesimals with internal water can survive the red giant stage of their parent star (Jura & Xu, 2010). We can constrain the water mass fraction in extrasolar planetesimals by determining the abundance of accreted hydrogen and/or oxygen in polluted white dwarfs (Klein et al., 2010). By analyzing the hydrogen abundance in an ensemble of helium dominated white dwarfs, Jura & Xu (2012) found that water is less than 1% of the total accreted material. Recently, Farihi et al. (2013) identified a white dwarf which has accreted a large amount of oxygen, in excess of what can be combined into MgO, SiO_2, FeO, CaO and Al_2O_3; they concluded that the accreted asteroid is at least 26% water by mass. In addition, if there is enough water in the disk, molecular water emission lines might be detectable in the near-infrared, similar to those around T Tauri stars (Carr & Najita, 2008).

In this paper, we focus on two pulsating ZZ Ceti hydrogen white dwarfs, G29-38 (WD 2326+049) and GD 133 (WD 1116+026). G29-38 is a fascinating white dwarf and a record

holder. It is the first and also the closest white dwarf identified with an infrared excess (Zuckerman & Becklin, 1987) and a 10 μm circumstellar silicate emission feature (Reach et al., 2005, 2009). It is among the very first few hydrogen white dwarfs that were found to be polluted (Koester et al., 1997), which led to the identification of a white dwarf subclass "DAZ" (Zuckerman et al., 2003). Very recently, G29-38, together with GD 133 and GD 31 are the first white dwarfs with photospheric detections of molecular hydrogen (Xu et al., 2013b). The atmospheric pollution in GD 133 was first reported in the SPY survey (Koester et al., 2005a; Koester & Wilken, 2006). It also has an orbiting dust disk as well as a 10 μm silicate feature (Jura et al., 2007a, 2009a).

The paper is organized as follows. In Section 2, we report data acquisition and reduction methods. In Section 3, we determine stellar parameters for G29-38 and GD 133. The heavy element abundances are reported in Section 4. In Section 5, we compare the composition of the parent body accreted onto G29-38 and GD 133 with solar system objects. In Section 6, we put our results in perspective and conclusions are given in Section 7.

4.2 Observations

We performed spectroscopic studies of G29-38 and GD 133 with the High Resolution Echelle Spectrometer (HIRES) on the Keck telescope and the Cosmic Origins Spectrograph (COS) on the Hubble Space Telescope. G29-38 was also observed with the NIRSPEC on the Keck Telescope. The observation logs are presented in Table 4.1 and described in detail below.

4.2.1 Keck/HIRES Optical Spectroscopy

The optical data were acquired with HIRES (Vogt et al., 1994) on the Keck I telescope at Mauna Kea Observatory under good weather conditions except for the night of Aug 7, 2008, where high cirrus clouds were present that caused 2-3 magnitudes of extinction. The C5 slit with a width of $1\farcs148$ was used for all observations. The spectral resolution is $\sim$ 40,000 as measured from the Th-Ar lamps.

The MAKEE software[1] was used to extract the spectra from the flat-fielded two-dimensional image of each exposure with the trace of a bright calibration star. Wavelength calibration was performed using the standard Th-Ar lamps. Following Klein et al. (2010, 2011), we used IRAF to normalize the spectra and combine echelle orders. When multiple exposures were present, each exposure was processed separately based on steps outlined above and combined afterwards, weighted by their count rate. For GD 133, there was second order contamination in 8200-9000 Å region and we followed Klein et al. (2010) to calibrate and extract that part of the spectrum. For both stars, the final spectra were continuum-normalized but not flux calibrated. The signal-to-noise ratio (S/N) for G29-38 is 50-90 shortward of 3850 Å and 90-210 for longer wavelengths. For GD 133, the S/N is 30-60 shortward of 3900 Å and longward of 6000 Å and 60-110 for the rest.

4.2.2 HST/COS Ultraviolet Spectroscopy

G29-38 and GD 133 were observed as part of the HST cycle 18 program 12290, "Do Rocky Extrasolar Minor Planets Have a Composition Similar to Bulk Earth?". G29-38 was observed at two different times due to the malfunction of a gyro during part of the first observation. Instrument configuration and data reduction procedures were described in Xu et al. (2013b). Following Jura et al. (2012), we extracted night-time portions of the data to remove geocoronal O I emission lines near 1304 Å. For GD 133, there were 4711 sec of useful night time data and the S/N of the unsmoothed spectrum is 8 around O I 1304 Å. For G29-38, there are only 400 sec of effective night time exposure and the data were not used for the analysis.

4.2.3 Keck/NIRSPEC Infrared Spectroscopy

G29-38 was observed with the NIRSPEC (McLean et al., 1998, 2000) on the Keck II telescope in low resolution R $\sim$ 2000 spectroscopy mode and a central wavelength of 3 μm. The slit size was chosen to be $42 \times 0\farcs57$, matching the average seeing of the night around $0\farcs6$. Exposures were 60 sec each; 60 co-added images with a 1 sec frame time. The target was observed at

[1]MAKEE Keck Observatory HIRES Data Reduction Software, http://www2.keck.hawaii.edu/inst/common/makeewww/

two nod positions; a complete set includes an ABBA nod pattern and has a total on target time of 4 minutes. After 3-5 sets of observations on G29-38, an equal number of sets were taken on the calibration star HD 222749 (B9V) to remove telluric features and instrument transmission features.

All spectroscopic reductions were made using the REDSPEC software[2] following procedures outlined in McLean et al. (2003), which includes corrections of nonlinearity in the spatial and spectral dimensions, wavelength calibrations with the Ne and Ar lamps, extraction of the spectra and removal of telluric features and the instrument response function. To restore the spectral slope, the spectrum is multiplied by a black body curve of 9150 K, the temperature of the calibration star. The last step is to flux calibrate the spectrum to the IRAC 3.6 μm flux (Farihi et al., 2008a). The final spectrum is shown in Figure 4.1; it has a higher spectral resolution and S/N than previous near-infrared data from the IRTF (Tokunaga et al., 1990) and Gemini (Farihi et al., 2008a).

4.3 Model Atmosphere and Stellar Parameters

Synthetic white dwarf model atmospheres were computed with basic input parameters including effective temperature, T_{eff}, surface gravity, g, and atmospheric abundances of heavy elements. The computed model spectra presented here are a new grid with two major changes compared to previous work in Koester (2009, 2010). (i) The mixing-length parameter ML2/α is taken as 0.8, which is now the preferred value of the Montreal group (Tremblay et al., 2010). (ii) New Stark broadening data are used (Tremblay & Bergeron, 2009). The adopted T_{eff} and g are shown in Table 4.2 and elemental abundances in Table 4.3. Below we describe the fitting process in detail. Fortunately, precise stellar parameters are not essential for our analysis because we are most interested in the relative abundance ratios, which are fairly insensitive to particular models (Klein et al., 2011).

[2]NIRSPEC Data Reduction with REDSPEC, http://www2.keck.hawaii.edu/inst/nirspec/redspec.html

Table 4.1 Observation Logs for G29-38 and GD 133

Star	UT Date	Instrument	λ range (Å)	Exposure (sec)
G29-38	2006 Jun 11	HIRES/red	5690-10160	7,200
	2008 Aug 7	HIRES/blue	3115-5950	2,000
	2010 Oct 17	COS	1145-1445	1,999
	2011 Jan 19	COS	1145-1445	7,035
	2011 Aug 15	NIRSPEC	27,500-36,000	2,160
GD 133	2008 Feb 13	HIRES/blue	3135-5965	2,700
	2008 Feb 26	HIRES/red	4600-8995	2,400
	2011 May 28	COS	1145-1445	13,460

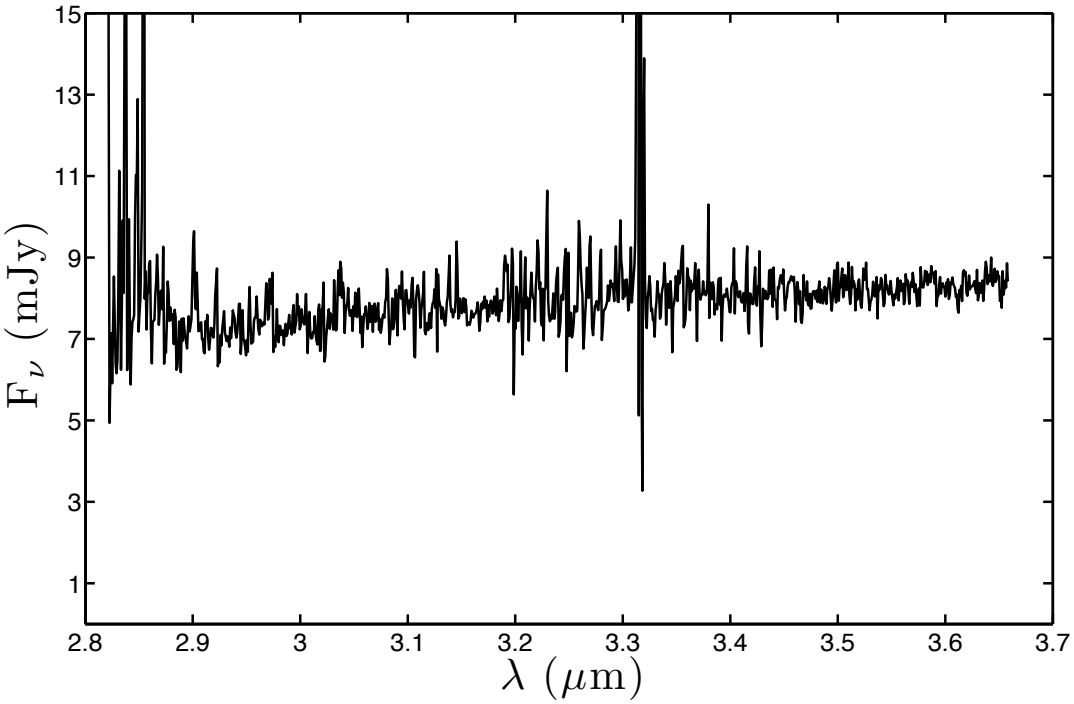

Figure 4.1 Keck/NIRSPEC KL band spectrum for G29-38 and flux calibrated to IRAC 3.6 μm photometry. The spectral resolution is 2000 and the data are neither binned nor smoothed. The noisy region shortward of 2.9 μm is due to bright sky background and the emission around 3.3 μm is from an instrumental artifact. The spectrum is generally featureless with a gentle increase towards longer wavelength, consistent with the dust disk model.

Table 4.2 Adopted Stellar Parameters for G29-38 and GD 133

Star	M_* ($M_\odot$)	T_{eff} (K)	log g (cm s^{-2})	D (pc)	log M_{cvz}/M_* [a]
G29-38	0.85	11820 ± 100	8.40 ± 0.10	13.6 ± 0.8	-13.9
GD 133	0.66	12600 ± 200	8.10 ± 0.10	36.6 ± 3.2	-16.2

Notes. [a] M_{cvz} is the mass of the convection zone. The convection zone of GD 133 is within a Rosseland mean opacity ~ 8, considerably shallower than that of G29-38.

4.3.1 G29-38

G29-38 has a parallax π= 0.0734 ± 0.0040 arcsec (van Altena et al., 2001) as well as UBVRI photometry (Holberg et al., 2008). Its infrared photometry was not used for the fitting due to contamination from the dust disk (Zuckerman & Becklin, 1987). Additional data were also used for the analysis, including the HST/FOS spectra, two optical spectra from the 2.2m Calar Alto telescope (Koester et al., 1997) and two spectra from the VLT/UVES (Koester et al., 2005a; Koester, 2009).

The surface gravity of G29-38 can be tightly constrained from the parallax. For any reasonable effective temperature within the instability strip the gravity has to be in the interval 8.30-8.50 with the most consistent solution of 8.40. Varying the parallax within the quoted error of 0.004 arcsec shifts the optimum log g value by 0.05 dex. Holding gravity as a fixed value, we are able to derive T_{eff}; with all available observing data, the best solution is listed in Table 4.2. The fits to Balmer lines from Hα to Hη are shown in Figure 4.2. The higher order Balmer lines in the model are not as deep as observed. G29-38 is a pulsating ZZ Ceti white dwarf and the velocity fields tend to cause line profiles to be broader and shallower (Koester & Kompa, 2007). But this effect is only relevant for the innermost cores within 1 Å and does not influence the parameter determinations. The problem can be solved by adopting a lower surface gravity but this contradicts the parallax measurement. Assuming the parallax is correct, the disagreement could indicate a problem with our implementation of the Balmer line broadening theory (Tremblay & Bergeron, 2009) and/or the calculation of occupation

Table 4.3 Final Atmospheric Abundances for G29-38 and GD 133

	G29-38			GD 133		
Z	[Z/H][a]	t_{set} (10^{-1} yr)	$\dot{M}(Z_i)$[b] (g s^{-1})	[Z/H][a]	t_{set} (10^{-3} yr)	$\dot{M}(Z_i)$[b] (g s^{-1})
C	-6.90 ± 0.12	7.8	1.2×10^6	< -7.9	5.3	$< 7.6 \times 10^4$
N	< -5.7	6.4	$< 2.6 \times 10^7$	< -5.8	3.4	$< 1.7 \times 10^7$
O	-5.00 ± 0.12	4.5	2.2×10^8	-6.00 ± 0.11	2.4	1.8×10^7
Na	< -6.7	2.1	$< 1.3 \times 10^7$	< -6.3	3.7	$< 8.2 \times 10^6$
Mg	-5.77 ± 0.13	2.5	9.8×10^7	-6.5:	9.2	2.2×10^6:
Al	< -6.1	3.4	$< 3.8 \times 10^7$	< -5.7	6.4	$< 2.3 \times 10^7$
Si	-5.60 ± 0.17	4.6	9.4×10^7	-6.60 ± 0.13	5.5	3.4×10^6
S	< -7.0	4.1	$< 4.8 \times 10^6$	< -7.0	2.9	$< 3.0 \times 10^6$
Ca	-6.58 ± 0.12	2.0	3.1×10^7	-7.21 ± 0.13	6.2	1.1×10^6
Ti	-7.90 ± 0.16	2.7	1.4×10^6	< -8.0	5.3	$< 2.4 \times 10^5$
Cr	-7.51 ± 0.12	2.4	4.0×10^6	< -6.8	4.3	$< 5.1 \times 10^6$
Mn	< -7.2	2.2	$< 9.5 \times 10^6$	< -7.0	4.2	$< 3.5 \times 10^6$
Fe	-5.90 ± 0.10	2.1	2.0×10^8	< -5.9	3.6	$< 5.2 \times 10^7$
Ni	< -7.3	1.9	$< 9.6 \times 10^6$	< -7.0	3.1	$< 5.1 \times 10^6$
Total[c]			6.5×10^8			2.4×10^7

Notes. See Table 4.4 for details.

[a] [X/Y] = log n(X)/n(Y), the logarithmic number ratio of the abundance of element X relative to the abundance of Y.

[b] The instantaneous mass accretion rate of an element into the white dwarf's atmosphere (see section 5). This is calculated by dividing the mass of an element currently in the convection zone with its settling time.

[c] The total accretion rate including all elements with positive detections.

probabilities based on the prescription of Hummer & Mihalas (1988)[3]. Our newly derived stellar mass is 0.85 $M_{\odot}$, significantly higher than all previous analysis (Koester et al., 1997; Giammichele et al., 2012) but close to the value of 0.79 $M_{\odot}$ derived from asteroseismology (Chen & Li, 2013).

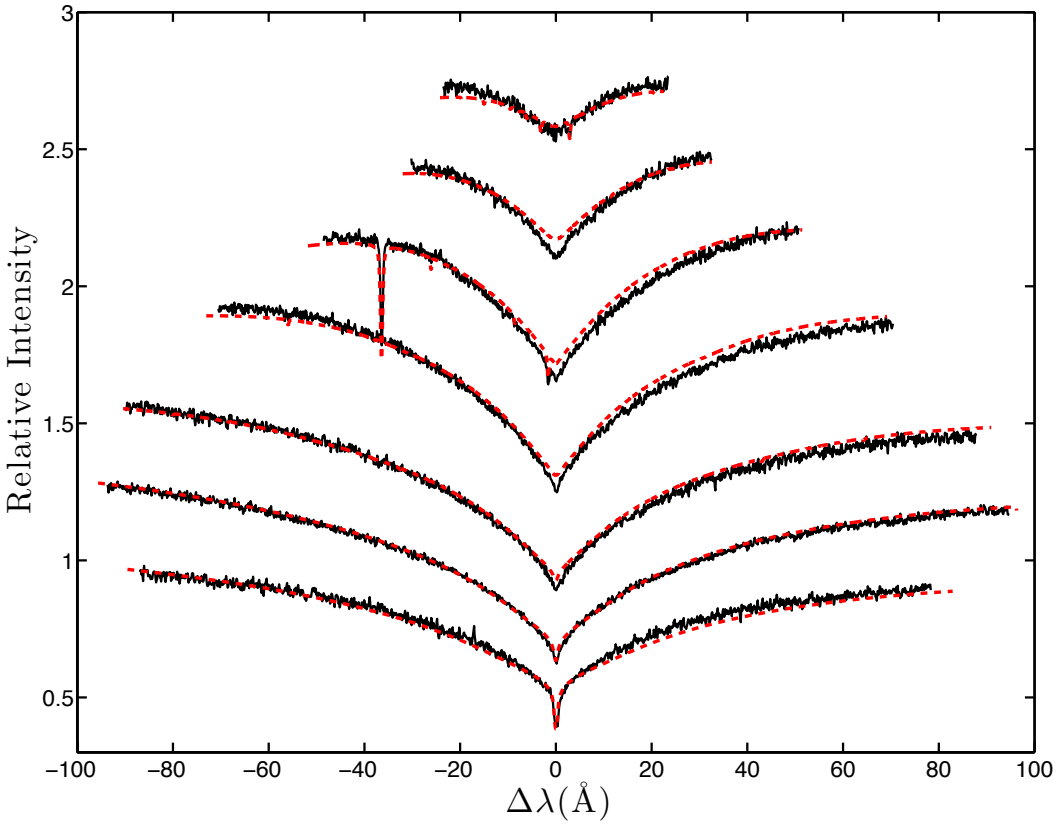

Figure 4.2 Model fits (red dashed lines) to Balmer lines, including Hα to Hη from bottom to top with T_{eff} = 11,820 K, log g=8.40 for G29-38. Each line is offset by 0.3 in relative intensity for clarity. The underlying spectrum in black is from the SPY survey (Koester et al., 2005a; Koester, 2009). Ca II K-line is seen at the left wing of Hϵ with $\Delta\lambda$ of -37 Å.

[3]The real issue is that G29-38 is in the parameter range where the Balmer line strengths reach their maximum and are rather insensitive to changes in stellar parameters. As a result, we use all available data to derive the stellar parameters. In addition, relative abundance ratios are not strongly dependent on stellar parameters. As illustrated in Klein et al. (2011), for PG 1225-079, simultaneous changes of 1500 K in temperature and 0.6 dex in log g lead to a mixmum change of 0.1 dex for relative abundances.

4.3.2 GD 133

There is no known parallax for GD 133 and we rely completely on spectroscopic method to derive its stellar parameters. Refitting the SPY spectra (Koester et al., 2005a) with our latest model grid gives T_{eff} = 12,729 K and log g = 8.02. GD 133 was also studied by Gianninas et al. (2011); with a different set of data and model, they derived T_{eff} = 12,600 K and log g = 8.17. The average of the two log g from optical studies is 8.10 and we can derive T_{eff} from fitting the Lyman α profile in the COS spectrum. The formal error of this fitting is extremely small ($\sim$ 10 K) and the quoted error is dominated by the error in log g. The errors listed in Table 4.2 for log g and T_{eff} include systematic and statistical errors. The final parameters are close enough to previous values that the new fits are not shown here.

4.4 Atmospheric Abundance Determinations

To reflect instrumental broadening, the computed model spectra are convolved with the Line Spread Function of COS (Kriss, 2011) or a Gaussian profile for the HIRES data. Then the abundances of individual elements are determined by comparing the equivalent width (EW) of each spectral line with that from the model spectra (Klein et al., 2010, 2011). Compared to helium atmosphere white dwarfs with the same amount of pollution [e.g. Dufour et al. (2012)], the analysis in hydrogen atmosphere white dwarfs is less affected by blending of different absorption lines due to the high continuum opacity of hydrogen atoms. However, molecular hydrogen lines are pervasive in the COS data for both stars. The analysis for GD 133 is less affected because the number density of molecular hydrogen in GD 133 is about 0.4 dex smaller than that in G29-38 (Xu et al., 2013b). For both stars, we present model spectra with and without the contribution from molecular hydrogen.

Following Xu et al. (2013a), upper limits to the abundances of elements were estimated by varying the input abundance of an element and comparing the model spectra with data. The presence of numerous molecular hydrogen lines in the COS data complicates this process and

the model is not ideal for computing the line strength of individual H_2 lines due to the lack of accurate broadening parameters (Xu et al., 2013b). To be conservative, all upper limits obtained from the ultraviolet data were determined by using the model spectra without contributions from H_2; the numbers can be lower if molecular hydrogen contributes to a significant portion of the total EW.

All detailed measurements are presented in Table 4.4 and the final abundances in Table 4.3. For G29-38, there are 27 optical spectral lines identified from 5 different elements and 8 ions, including Mg I, Mg II, Ca I, Ca II, Cr II, Fe I, Fe II and Ti II. The average velocity of all absorption lines, including Doppler shift and gravitational redshift, is 36 $\pm$ 2 km s^{-1}. The COS data reveal photospheric detection of C I, O I and Si II with an average velocity of 40 $\pm$ 4 km s^{-1}, which agrees with the optical value. We have also detected an interstellar line of Si II at 1260.4 Å and C II at 1334.5 Å with an average velocity of 11 km s^{-1}. This is very close to the radial velocity of 9.5 km s^{-1} measured in the Hyades cloud[4] (Redfield & Linsky, 2008), which lies within 15 pc of the Sun. For GD 133, there are 5 optical spectral lines identified from Ca II and the marginal detection of Mg II as well as 4 ultraviolet lines from Si II and O I. The average velocity shift is 49 $\pm$ 2 km s^{-1} and 58 $\pm$ 4 km s^{-1} for the optical and ultraviolet data, respectively. The difference between these two velocities are most likely due to the absolute wavelength uncertainty of 15 km s^{-1} for the medium resolution grating G130M on COS (COS Instrument Handbook). Interstellar lines at Si II 1260.4 Å, O I 1302.2 Å and C II 1334.5 Å are also detected with an average velocity of 15 km s^{-1}, close to the radial velocities of several nearby clouds, including the Gem Cloud and NGP Cloud. (Redfield & Linsky, 2008). In both stars, upper limits were derived for a few elements.

[4]According to the dynamical model of the local interstellar medium: http://lism.wesleyan.edu/LISMdynamics.html

Table 4.4: Measured Equivalent Widths of Photospheric Lines and Abundance Determinations for G29-38 and GD 133

				G29-38		GD 133	
Ion	λ^a (Å)	E_{low} (eV)	log gf	EW (mÅ)	[Z/H]	EW (mÅ)	[Z/H]
C I	1277.6	0.01	-0.40	$52 \pm 9^{b-H_2}$	-6.96 ± 0.08	...	...
C I	1329.6	0.01	-0.62	$42 \pm 8^{b-H_2}$	-6.85 ± 0.08	...	...
C II	1335.7	0.01	-0.34	...	...	$< 20^{b-H_2}$	< -7.9
C					-6.90 ± 0.12		< -7.9
N I	1411.9	3.58	-1.3	< 27	< -5.7	< 25	< -5.8
O I	1152.2	1.97	-0.27	$81 \pm 22^{b-H_2}$	-5.00 ± 0.12	...	...
O I	1304.9	0.02	-0.84	...	...	63 ± 16	-6.00 ± 0.11
O					-5.00 ± 0.12		-6.00 ± 0.11
Na I	5891.6	0	0.12	< 24	< -6.7	< 30	< -6.3
Mg I	3830.4	2.71	-0.23	14 ± 3	-5.62 ± 0.09	...	...
Mg I	3833	2.71	0.12, -0.36	21 ± 5	-5.89 ± 0.10	...	...
Mg I	3839.4	2.72	0.39	35 ± 4	-5.86 ± 0.05	...	...
Mg I	5174.1	2.71	-0.39	31 ± 4	-5.65 ± 0.06	...	...
Mg I	5185.0	2.71	-0.17	42 ± 4	-5.72 ± 0.04	...	...
Mg II	4482	8.86	0.74, 0.59	41 ± 7	-5.91 ± 0.08	14 ± 4	-6.5:
Mg					-5.77 ± 0.13	...	-6.5:
Al I	3945.1	0	-0.62	< 16	< -6.1	< 19	< -5.7

Table 4.4 — *Continued*

				G29-38		GD 133	
Ion	λ^a (Å)	E_{low} (eV)	log gf	EW (mÅ)	[Z/H]	EW (mÅ)	[Z/H]
Si II	1260.4	0	0.387	...	...	93 ± 26	-6.67 ± 0.11
Si II	1264.7	0.04	0.64	320 ± 64^{b-SiII}	-5.76 ± 0.09	115 ± 20	-6.70 ± 0.07
Si II	1265.0	0.04	-0.33	320 ± 64^{b-SiII}	-5.76 ± 0.09	51 ± 12	-6.60 ± 0.13
Si II	1309.3	0.04	-0.43	106 ± 11$^{b-H_2}$	-5.48 ± 0.05	61 ± 12$^{b-H_2}$	-6.42 ± 0.05
Si					-5.60 ± 0.17		-6.60 ± 0.13
S I	1425.0	0	-0.12	$< 55^{b-H_2}$	< -7.0	$< 38^{b-H_2}$	< -7.0
Ca I	4227.9	0	0.27	17 ± 3	-6.67 ± 0.07	...	...
Ca II	3159.8	3.12	0.24	67 ± 5	-6.69 ± 0.03	...	...
Ca II	3180.3	3.15	0.50	109 ± 5	-6.61 ± 0.02	37 ± 4	-7.23 ± 0.05
Ca II	3182.2	3.15	-0.46	40 ± 4	-6.46 ± 0.04	...	...
Ca II	3707.1	3.12	-0.48	24 ± 4	-6.65 ± 0.07	...	...
Ca II	3934.8	0	0.11	294 ± 6	-6.65 ± 0.01	154 ± 13	-7.08 ± 0.04
Ca II	3969.6	0	-0.2	78 ± 7	-6.58 ± 0.04	27 ± 6	-7.07 ± 0.09
Ca II	8500.4	1.69	-1.4	84 ± 6	-6.34 ± 0.03	...	...
Ca II	8544.4	1.69	-0.46	185 ± 16	-6.54 ± 0.04	42 ± 7	-7.33 ± 0.07
Ca II	8664.5	1.69	-0.72	No Data	No Data	28 ± 4	-7.34 ± 0.07
Ca					-6.58 ± 0.12		-7.21 ± 0.13
Ti II	3235.4	0.05	0.43	13 ± 2	-8.06 ± 0.06	...	...
Ti II	3237.5	0.03	0.24	16 ± 6	-7.88 ± 0.15	...	...
Ti II	3350	0.61,0.05	0.43,0.53	31 ± 4	-7.95 ± 0.05	...	...
Ti II	3362.2	0.03	0.43	11 ± 2	-8.12 ± 0.08	< 12	< -8.0

Table 4.4 — *Continued*

				G29-38		GD 133	
Ion	λ^a (Å)	E_{low} (eV)	log gf	EW (mÅ)	[Z/H]	EW (mÅ)	[Z/H]
Ti II	3373.8	0.01	0.28	19 ± 3	-7.79 ± 0.05	...	...
Ti II	3384.7	0	0.16	19 ± 4	-7.70 ± 0.09	...	...
Ti II	3686.3	0.61	0.13	11 ± 2	-7.87 ± 0.08	...	...
Ti					-7.90 ± 0.16	...	< -8.0
Cr II	3125.9	2.46	0.30	13 ± 4	-7.42 ± 0.11	No Data	No Data
Cr II	3133.0	2.48	0.42	10 ± 4	-7.61 ± 0.17	No Data	No Data
Cr II	3369.0	2.48	-0.09	...	...	< 14	< -6.8
Cr					-7.51 ± 0.12		< -6.8
Mn II	3443.0	1.78	-0.36	< 14	< -7.2	< 15	< -7.0
Fe I	3582.2	0.86	0.41	12 ± 2	-5.97 ± 0.06	...	...
Fe I	3735.9	0.86	0.32	13 ± 3	-5.82 ± 0.09	...	...
Fe II	1361.4	1.67	-0.52	...	...	< 17	< -5.9
Fe II	3228.7	1.67	-1.18	12 ± 3	-5.79 ± 0.09	...	...
Fe					-5.90 ± 0.10		< -5.9
Ni II	1335.2	0.19	-0.19	$< 20^{b-H_2}$	< -7.3	$< 24^{b-H_2}$	< -7.0

Notes. The adopted abundances are also presented in Table 4.3.

[a] Wavelengths are in vacuum. Atomic data for absorption lines are taken from the Vienna

Atomic Line Database (Kupka et al., 1999).

[b] Blended line. The contributing element is noted in the superscript and the EW is the sum of the blend.

4.4.1 Carbon

The carbon lines in the observed wavelength interval can be contaminated by interstellar absorption because they arise from low lying energy levels. In a stellar environment, the C II 1335.7 line is always stronger than the C II 1334.5 line due to its larger statistical weight. However, as shown in Figure 4.3, the observed C II 1335.7 line is relatively weaker in both stars; we conclude that these C II lines are mostly interstellar. In addition, the measured velocity for the C II 1334.5 Å line is offset from all other photospheric lines in G29-38 and GD 133. This line also suffers from additional contamination from H_2.

There are C I lines at 1277.6 Å and 1329.6 Å detected in G29-38, as shown in Figures 4.3 and 4.4. The detection is nominally at least 5 σ and, in the absence of H_2, the derived abundance [C/H] would be -6.90 $\pm$ 0.08. However, due to their proximity to H_2 lines, the EW of the C I lines are less certain and we assign a conservative final abundance of -6.90 $\pm$ 0.12. For GD 133, the C II line at 1335.7 Å was used to place the upper limit, which is consistent with the upper bound from the C I 1329.6 Å line in Figure 4.3.

4.4.2 Oxygen

As presented in Figure 4.5, we have detected O I 1152.2 Å in G29-38, which can be reproduced by a model with an oxygen abundance of -5.00. The upper bound from O I triplet lines around 7775 Å also agrees with this result.

In the wavelength coverage of COS, there are several O I lines around 1300 Å, which can be contaminated from geocoronal emissions. When extracting the night time portions of the data for GD 133, we detected O I lines at 1302.1 Å and 1304.9 Å, as shown in Figure 4.6. The O I 1302.1 Å line comes from the ground state and there were at least two components, which agree with the interstellar and photospheric contributions, respectively. We use the O

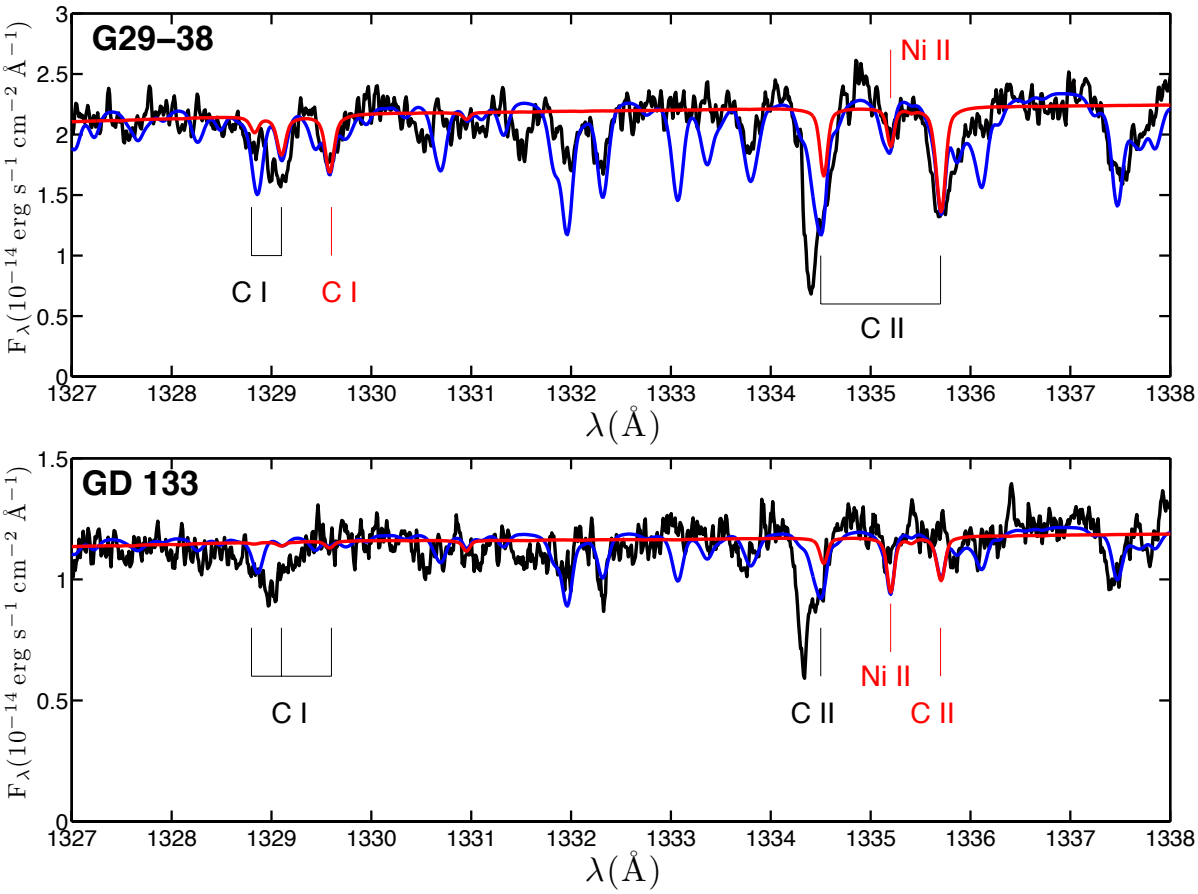

Figure 4.3 Carbon and nickel spectral line region for G29-38 and GD 133. The black line represents HST/COS data smoothed with a 3 pixel boxcar. The red and blue lines represent the model spectra without and with contributions from molecular hydrogen respectively, and with abundances from Table 4.3. Red labels represent lines that are used for abundance determinations in Table 4.4. Wavelengths are given in vacuum and the heliocentric reference frame.

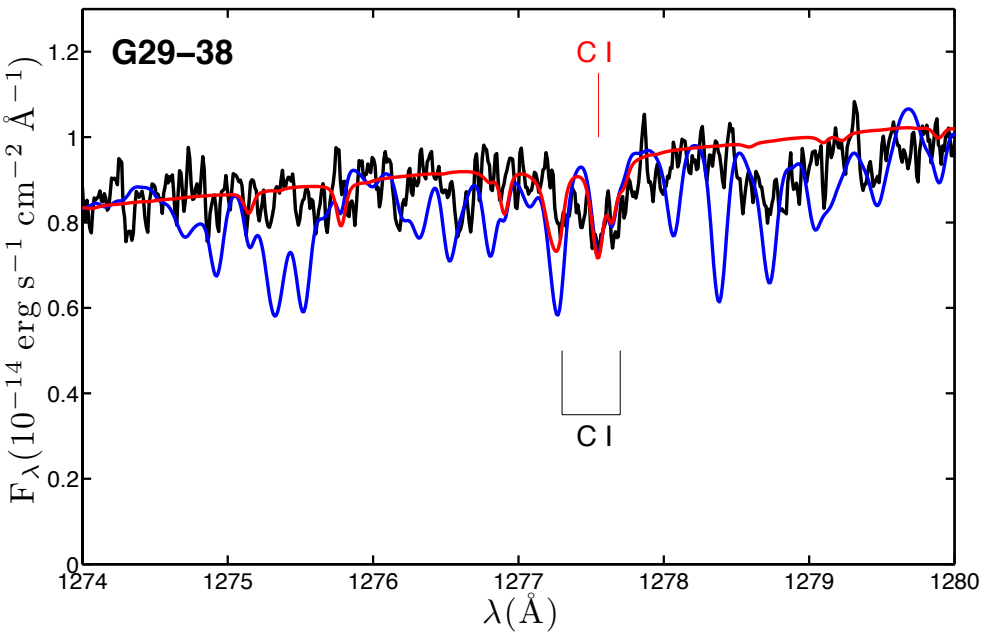

Figure 4.4 Similar to Figure 4.3 except for C I lines in G29-38.

I 1304.9 Å line and a model with [O/H] = -6.00 can successfully reproduce the data. This derived abundance is consistent with the strength of the O I 1302.1 Å and O I 1306.0 Å lines in Figure 4.6.

4.4.3 Magnesium

Magnesium is detected only in the optical data, as shown in Figure 4.7. In G29-38, the magnesium abundance was derived from a total of 7 spectral lines from both Mg I and Mg II. In GD 133, only the Mg II 4482 Å doublet is marginally seen and we were able to derive a tentative magnesium abundance.

4.4.4 Silicon

Several ultraviolet silicon lines are used for the analysis, as shown in Figure 4.8. Si II 1260.4 Å was not used for G29-38 because it is blended with an interstellar line. For G29-38, because Si II 1264.7 Å and 1265.0 Å lines are blended with each other, we report the total EW of this feature in Table 4.4. Si II 1309.3 Å can be blended with adjacent H_2 lines but the silicon

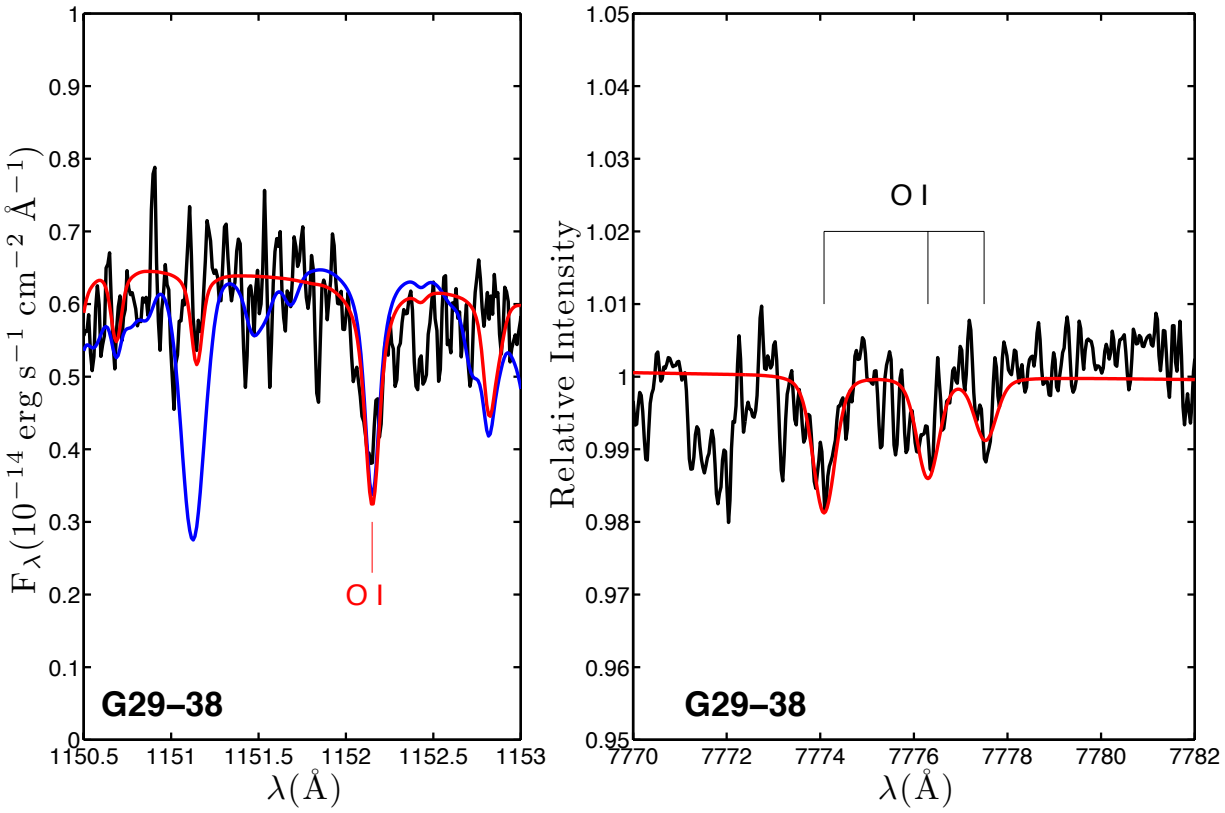

Figure 4.5 Similar to Figure 4.3 except for the detection of O I in G29-38. The right panel shows Keck/HIRES data smoothed with a 3 pixel boxcar and the spectrum is not flux calibrated. Only one model is plotted for the optical data, which are free from H_2 contamination.

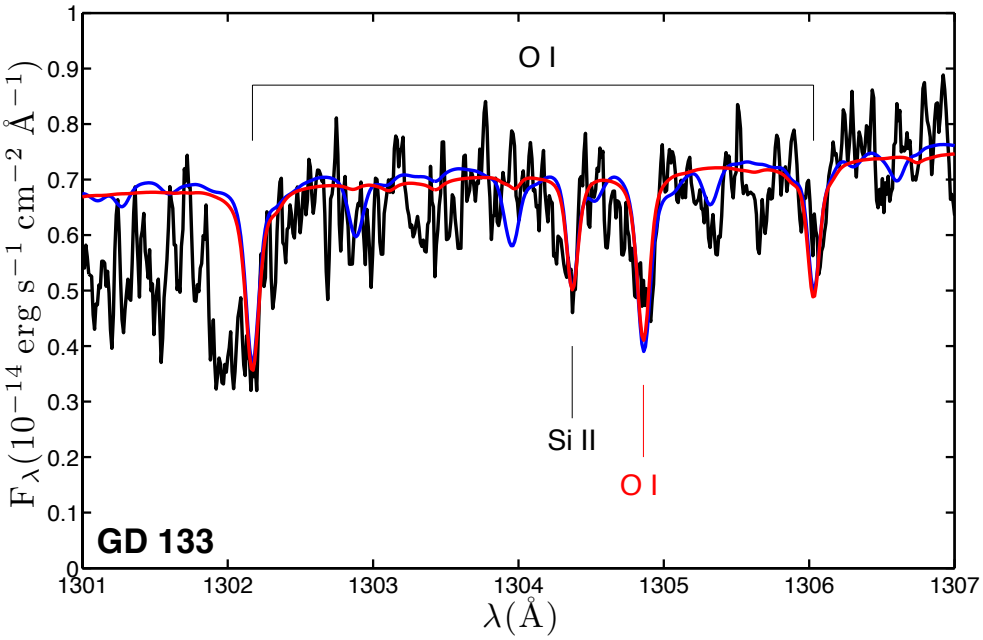

Figure 4.6 Similar to Figure 4.3 except for the night time portions of COS data of GD 133. The spectrum was smoothed with a 3 pixel boxcar.

line was readily detected and used in the analysis. For GD 133, the photospheric lines are weaker and easier to deblend. We were able to measure the EW of Si II lines at 1260.4 Å, 1264.7 Å and 1265.0 Å individually to derive the final abundance.

The Si II line at 1260.4 Å in GD 133 is the only readily detected interstellar line that is well separated with the photospheric line. And the EW is 48 $\pm$ 21 mÅ, corresponding to a Si II column density of 3.8 $\times$ 10^{12} cm^{-2} in that direction, which is comparable to typical ISM values (Lehner et al., 2003).

4.4.5 Calcium

von Hippel & Thompson (2007) found the EW of the Ca II K-line in G29-38 increased by 70% in 3 months, which they attributed to a variable mass accretion rate. However, a follow-up study of monitoring the Ca II H & K, Ca I 4227.9 Å and Mg II 4482 Å lines found no significant variability (Debes & López-Morales, 2008). Subsequently, Thompson et al. (2010) found that the EW of the Ca II K-line might be variable by a few percent and concluded

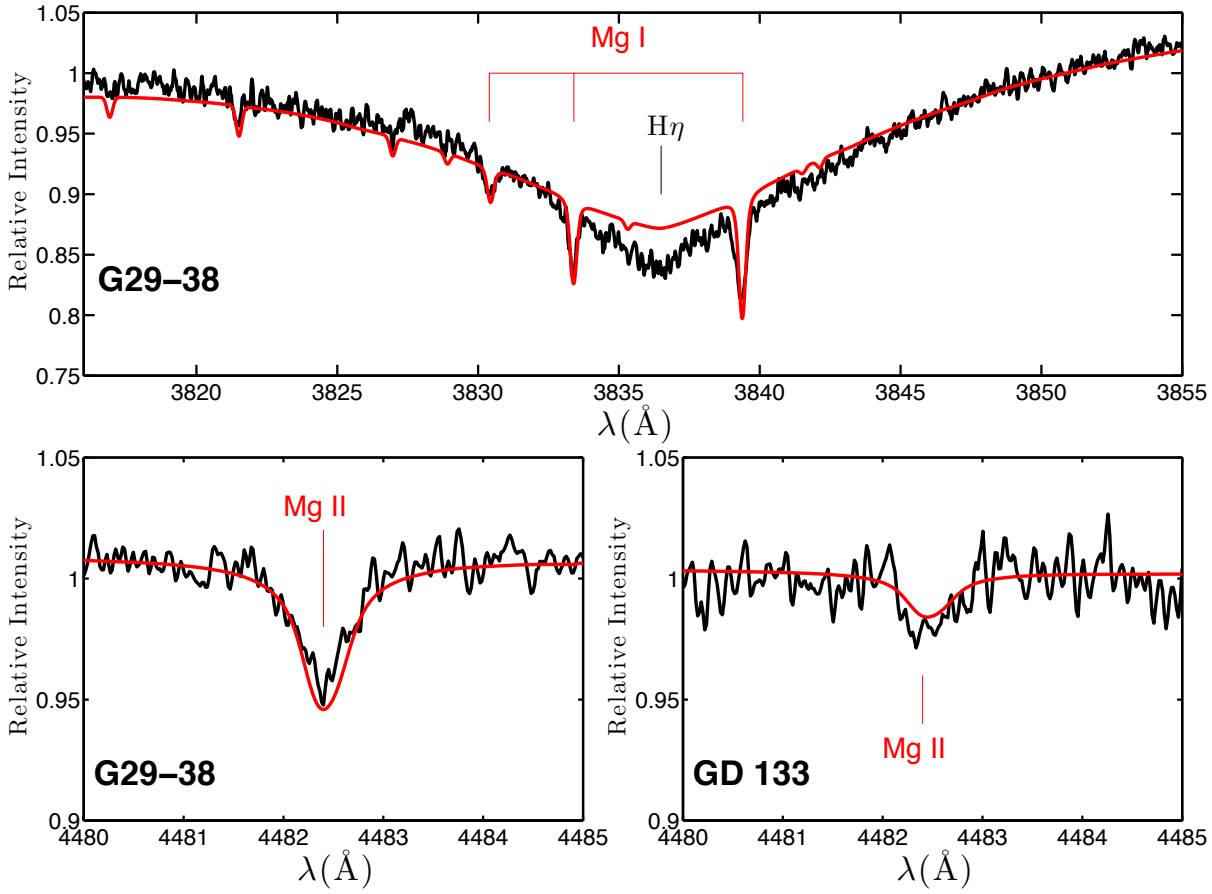

Figure 4.7 Similar to Figure 4.3 except for magnesium lines in the Keck spectra for G29-38 and GD 133. The spectrum in the top panel was smoothed with a 7 pixel boxcar while the ones in the lower panels are averaged by a 3 pixel boxcar. The fit to Hη in G29-38 is not ideal (see discussion in section 3.1) but we were still able to directly compare the EWs of Mg I lines in the data with the model. Detection of Mg in GD 133 is marginal.

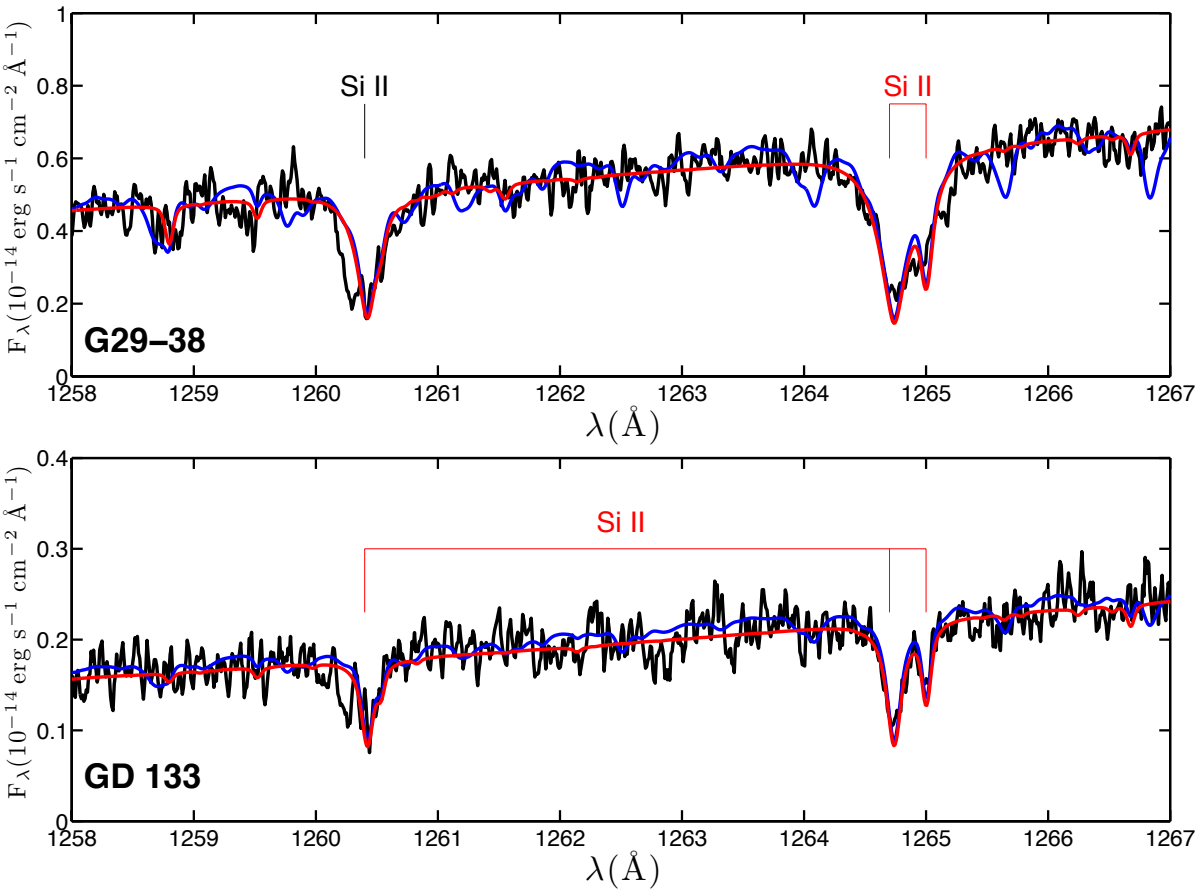

Figure 4.8 Similar to Figure 4.3 except for silicon lines. The Si II line at 1260.4 Å comes from the ground state and can be only used for the analysis of GD 133 because it is well separated from the interstellar absorption line.

that the pulsation model favors polar rather than equatorial accretion. In the present study, we are not concerned about EW uncertainty on a few percent level. There are quite a few calcium lines present in the HIRES spectra in both stars, as listed in Table 4.4 and shown in Figure 4.9. Our measured EWs of the Ca II H & K and Ca I 4227.9 lines agree within the uncertainties reported in Debes & López-Morales (2008) and Thompson et al. (2010). In GD 133, there are five Ca II lines detected and [Ca/H] = -7.21. We measured an EW of 154 ± 13 mÅ for the Ca II K-line, which lies within the uncertainty of the EW of 135 mÅ from VLT/UVES data but the derived abundance is different due to the updated model atmosphere calculations (Koester et al., 2005a; Koester & Wilken, 2006).

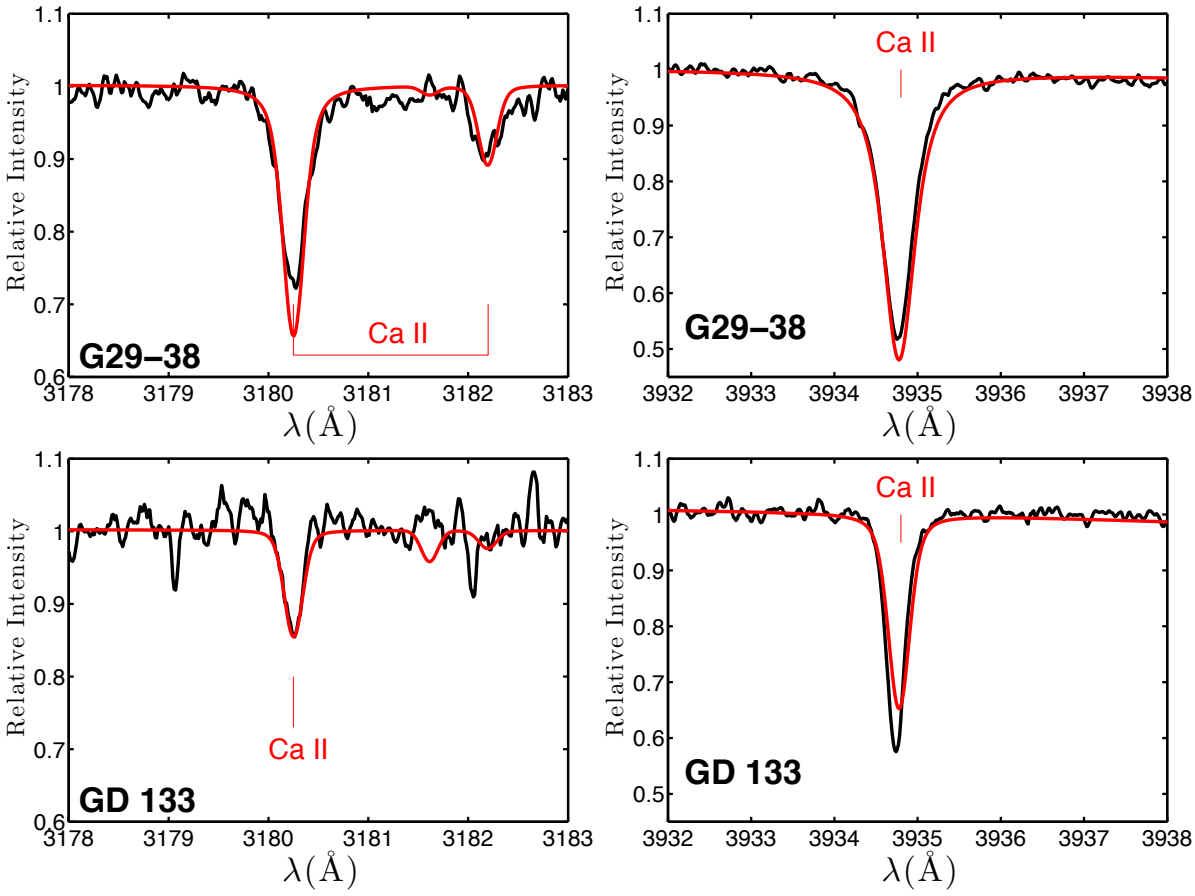

Figure 4.9 Similar to Figure 4.3 except for calcium lines in the Keck/HIRES data. All spectra were smoothed by a five-point boxcar average.

4.4.6 Titanium

Seven titanium lines were detected in the Keck/HIRES spectrum of G29-38 and three are displayed in Figure 4.10. Although most titanium lines have EWs smaller than 20 mÅ, they are readily detected due to the high S/N of the data. In GD 133, the Ti II 3362.2 Å line was used to derive the upper limit.

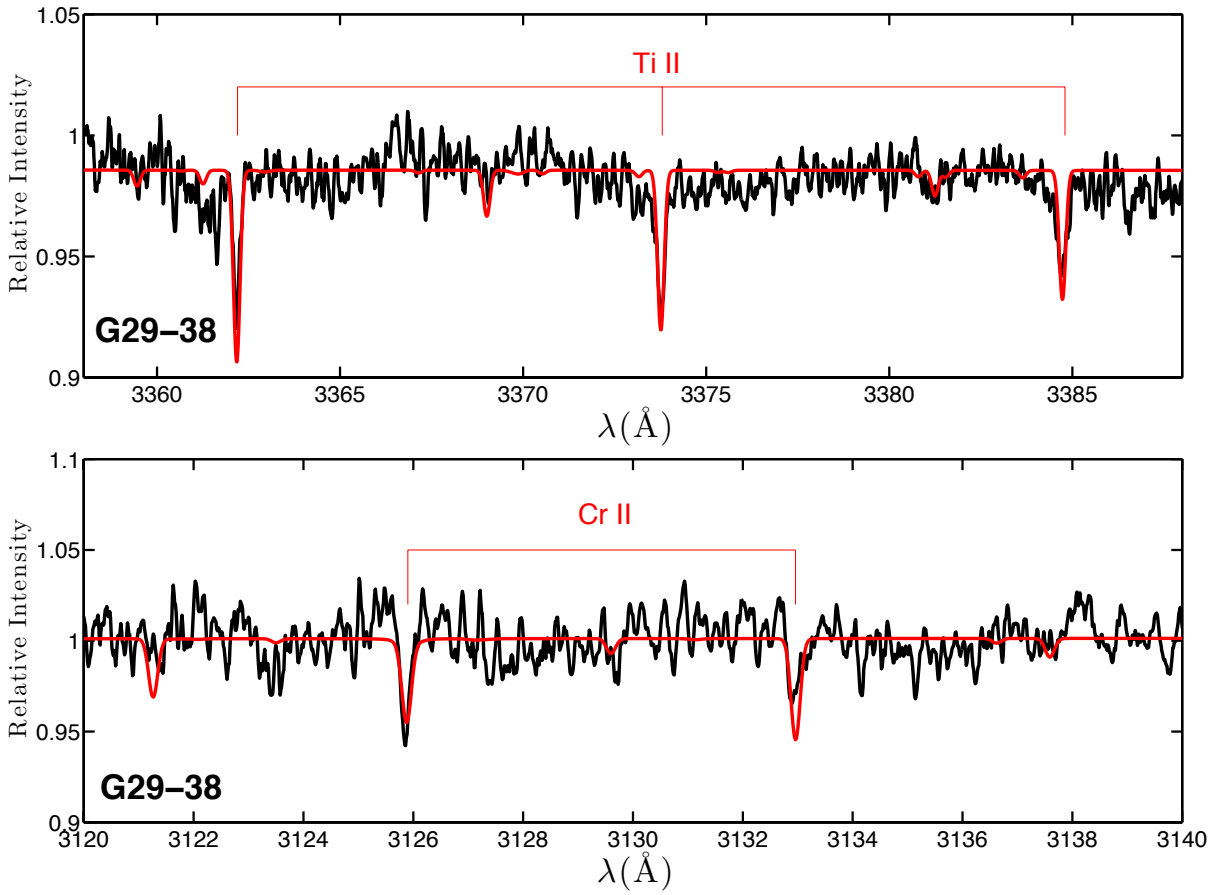

Figure 4.10 Similar to Figure 4.3 except for titanium and chromium lines. Both spectra were smoothed by a seven-point boxcar average.

4.4.7 Chromium

In G29-38, there are two chromium lines at 3125.9 Å and 3133.0 Å in the observed wavelength interval as shown in Figure 4.10. The detection of each individual line is marginal but the presence of lines at two correct wavelengths makes the identification more convincing. In

GD 133, these two chromium lines fall off the edge of echelle orders and the next strongest chromium line at 3369.0 Å was used to derive the upper limit.

4.4.8 Iron

Three optical iron lines are detected in G29-38 and two of them are presented in Figure 4.11. Iron is not detected in GD 133. Since molecular hydrogen does not significantly interfere near the Fe II 1361.4 Å region in GD 133, we use the absence of this strong Fe line to derive an upper limit to the abundance.

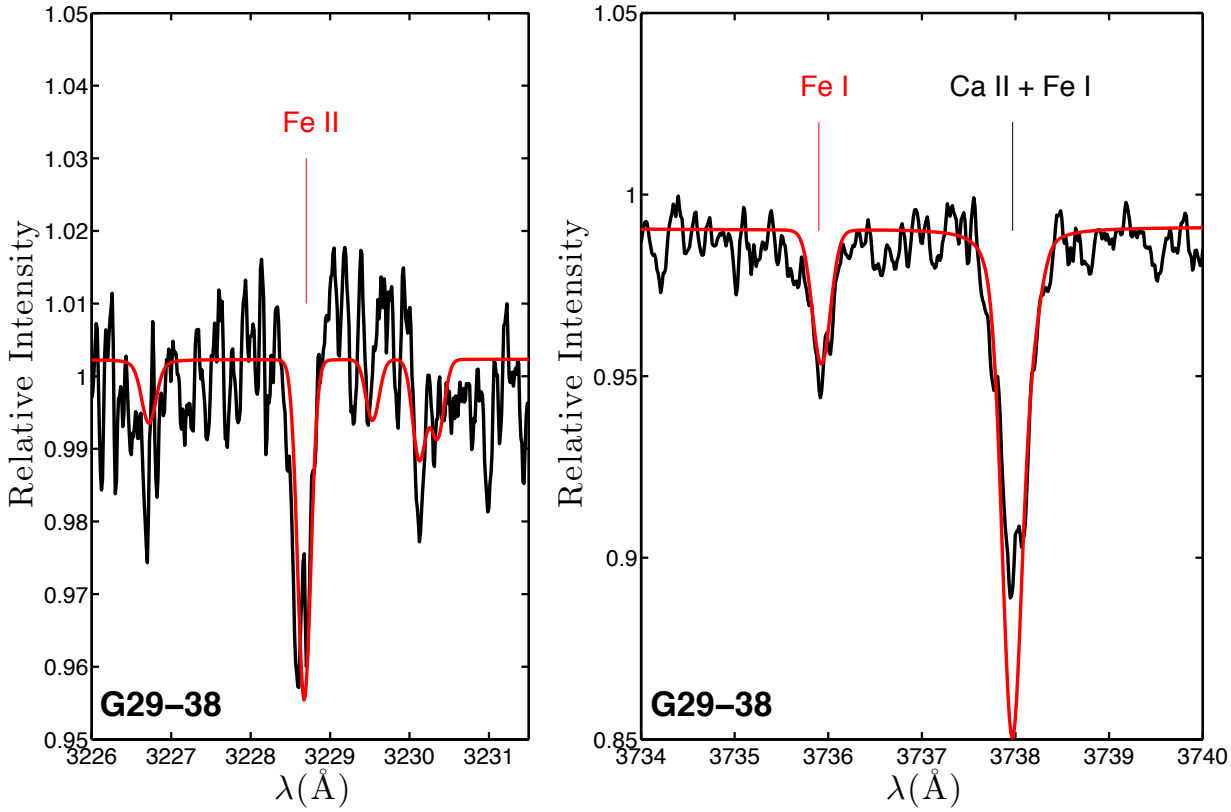

Figure 4.11 Similar to Figure 4.3 except for iron lines in G29-38. Both spectra were smoothed by a five-point boxcar average. The absorption feature around 3738 Å is a blend of Ca II and Fe I lines, which is dominated by Ca II.

4.4.9 Additional Upper Limits

Nitrogen, Sulfur, Nickel: The nitrogen triplet around 1200 Å is in the wing of Lyman α and the S/N of the spectrum is very low, making N I 1411.9 Å the best nitrogen line in our data set, as shown in Figure 4.12. To derive the sulfur upper limit, S I 1425.03 Å was used and the fit is presented in Figure **??**. Due to the presence of adjacent molecular hydrogen lines, the sulfur upper limit is less constraining in G29-38 than in GD 133. We also used Ni II 1335.2 Å to determine the upper limit as shown in Figure 4.3.

Sodium, Aluminum, Manganese: Optical spectral lines were used to determine the upper limits for these elements. The details are listed in Table 4.4 and their spectra are not presented.

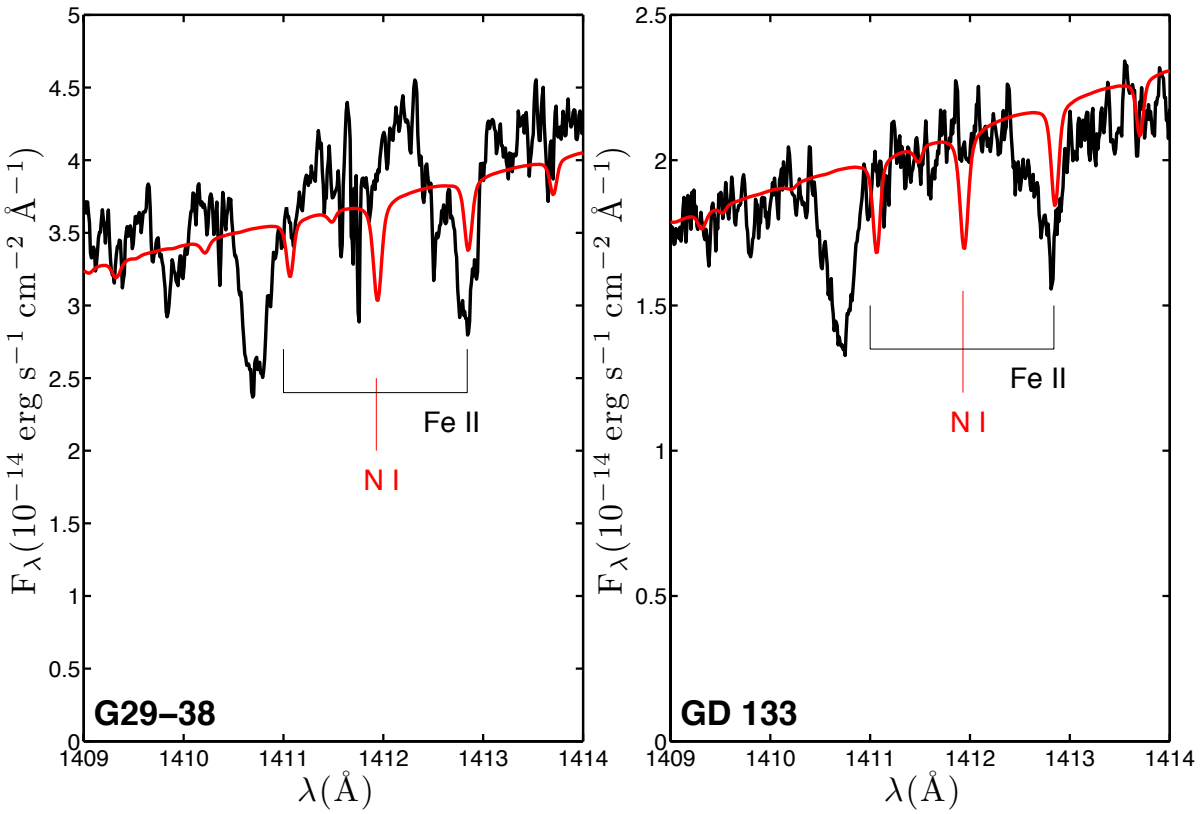

Figure 4.12 Similar to Figure 4.3 except for N I 1411.9 Å, which is used to derive nitrogen upper limits. Only a model without molecular hydrogen is shown and used for the analysis. All the unlabeled features in the data are from molecular hydrogen.

4.5 Discussion

We have determined the abundances of 8 elements in G29-38, including C, O, Mg, Si, Ca, Ti, Cr, Fe and placed stringent upper limits on S and Ni. There are only three hydrogen dominated white dwarfs with more than 8 elements determined, i.e. 11 for WD 1929+012, 10 for WD 0843+516 (Gänsicke et al., 2012) and 9 for NLTT 43806 (Zuckerman et al., 2011). In GD 133, we have detected O, Si and Ca, marginally detected Mg, and placed a meaningful upper limit on the carbon abundance.

Both G29-38 and GD 133 show excess infrared radiation coming from an orbiting dust disk (Zuckerman & Becklin, 1987; Reach et al., 2005, 2009; Jura et al., 2007a). The source of accretion in both G29-38 and GD 133 is likely to come from one large parent body rather than a blend of several small ones, mainly because collisions among different objects will evaporate all the dust particles and destroy the dust disk (Jura, 2008). Because the settling times of heavy elements in these white dwarfs are less than a year (Koester, 2009), much shorter than the disk lifetime of $\sim 10^5$ yr (Farihi et al., 2012b), the accretion is likely to be in a steady state, wherein the rate of material falling on the white dwarf atmosphere is balanced by the settling out of the convection zone (Koester, 2009). We can infer the composition of the accreted extrasolar planetesimals based on the accretion flux, which is dependent on the settling times of each element.

4.5.1 Calculation of Settling Times

Very recently, Deal et al. (2013) have drawn attention to the fingering or thermohaline instability; they find that this effect is important in hydrogen dominated white dwarfs and can change the derived accretion rates by orders of magnitude. Unfortunately they do not publish enough details for us to draw conclusions about the relevance of the effect for the white dwarfs studied here. Some problems we see in Deal et al. (2013) are:

- Deal et al. (2013) use a prescription for the thermohaline diffusion coefficient from Vauclair & Théado (2012), which is claimed to be physically more realistic than pre-

vious methods. However, their formula leads to an infinite value for the coefficient at the bottom of the convection zone, which is unrealistic.

- In our model for G29-38 the bottom of the convection zone is at log (M_{cvz}/M_{star}) = -13.9 (see Table 4.2) and the layers above this will be homogeneously mixed in a matter of seconds. In Deal et al. (2013), the model 3 presented in both Figure 1 and 2 has no convection at all. The model 2, with parameters closest to G29-38 has a convection zone a factor of 100 smaller than G29-38. None of these models can represent our current objects.

- The H/He interface at log (M_{cvz}/M_{star}) = -5 is not a sharp boundary, but a transition zone. The helium will mix upward into the hydrogen and a significant helium fraction will still be present several pressure scale heights above this layer. This will lead to an increasing molecular weight, an effect apparently not considered in Deal et al. (2013).

- Their main argument is the fact that in previous determinations the accretion rates for helium white dwarfs seemed to be systematically higher than in hydrogen white dwarfs. In our opinion, a much more likely reason is the uncertainty in the depth of the convection zones in helium white dwarfs, which is described in corrected diffusion times[5] as well as possibly non-steady state accretion (see section 5.3 for more discussion).

For the time being, we do not believe that the Deal et al. (2013) calculations are applicable to G29-38 or GD 133; but we will reconsider our conclusions, once more details become available.

4.5.2 G29-38

The abundances in the parent body that accreted onto G29-38 are calculated by correcting for the settling effect of each element in the atmosphere, as shown in Table 4.3. In addition, the abundances can also be derived by fitting the infrared spectrum of the dust disk, which is composed of pulverized extrasolar planetesimals prior to accretion onto the white dwarf.

[5]see www.astrophysik.uni-kiel.de/∼koester

G29-38 has the brightest known dust disk due to its proximity to the Earth and Reach et al. (2005, 2009) found that the dominant minerals are amorphous carbon (C), amorphous and crystalline silicates ($MgFeSiO_4$, Fe_2SiO_4, $Fe_2Si_2O_6$, $CaMgSi_2O_6$, $Mg_2Si_2O_6$), water ice (H_2O) and metal sulfides ($Mg_{0.1}Fe_{0.9}S$). A comparison is shown in Figure 4.13 where we see that the derived number ratios of n(O)/n(Mg), n(Si)/n(Mg), n(Ca)/n(Mg) and n(Fe)/n(Mg) are in rough agreement in the atmosphere and in the surrounding dust disk. The biggest discrepancy is the abundances of carbon and sulfur.

While Reach et al. (2005, 2009) simulated the disk as an optically thin dust torus, we argue that it is more likely to be mostly opaque as described in Jura (2003); Jura et al. (2009a), for the following reasons. (i) In the optically thin disk model around G29-38, Reach et al. (2009) derived a total disk mass of 2×10^{19} g, which is three orders of magnitude smaller than the lower limit of the mass of heavy elements in the atmosphere of dusty helium dominated white dwarf [see, for example Jura et al. (2012)]. Assuming there is no difference between dusty hydrogen and helium white dwarfs, the disk must be much more massive and therefore optically thick. (ii) For dusty white dwarfs hotter than 20,000 K, the entire optically thin disk would be located outside of the tidal radius (Xu & Jura, 2012). There is no viable mechanism to explain the presence of so much hot dust outside the tidal radius of the white dwarf. In the opaque disk model, the radiation from the disk in the main contributor to the continuum, rather than from featureless emissions of minerals. This explains the discrepancy in carbon abundance because the emissivity spectrum of amorphous carbon is featureless (Reach et al., 2009). To account for the strong 10 μm silicate emission feature, Jura et al. (2009a) proposed the presence of an outer optically thin region or emission from a hot region on top of the opaque disk. Thus, the optically thin model from Reach et al. (2009) for the 10 μm emission features should work and most of their derived abundances agree with the values in the photosphere. However, the inclusion of niningerite ($Mg_{0.1}Fe_{0.9}S$) as the metal sulfide led Reach et al. (2009) to derive a high sulfur abundance; this is inconclusive due to the low S/N of the infrared spectrum (see Figure 5 in Reach et al. (2009)). This is the first direct comparison of elemental abundances derived from fitting the infrared spectrum of a dust disk with the spectroscopic analysis of a white dwarf atmosphere; the overall

agreement is respectable.

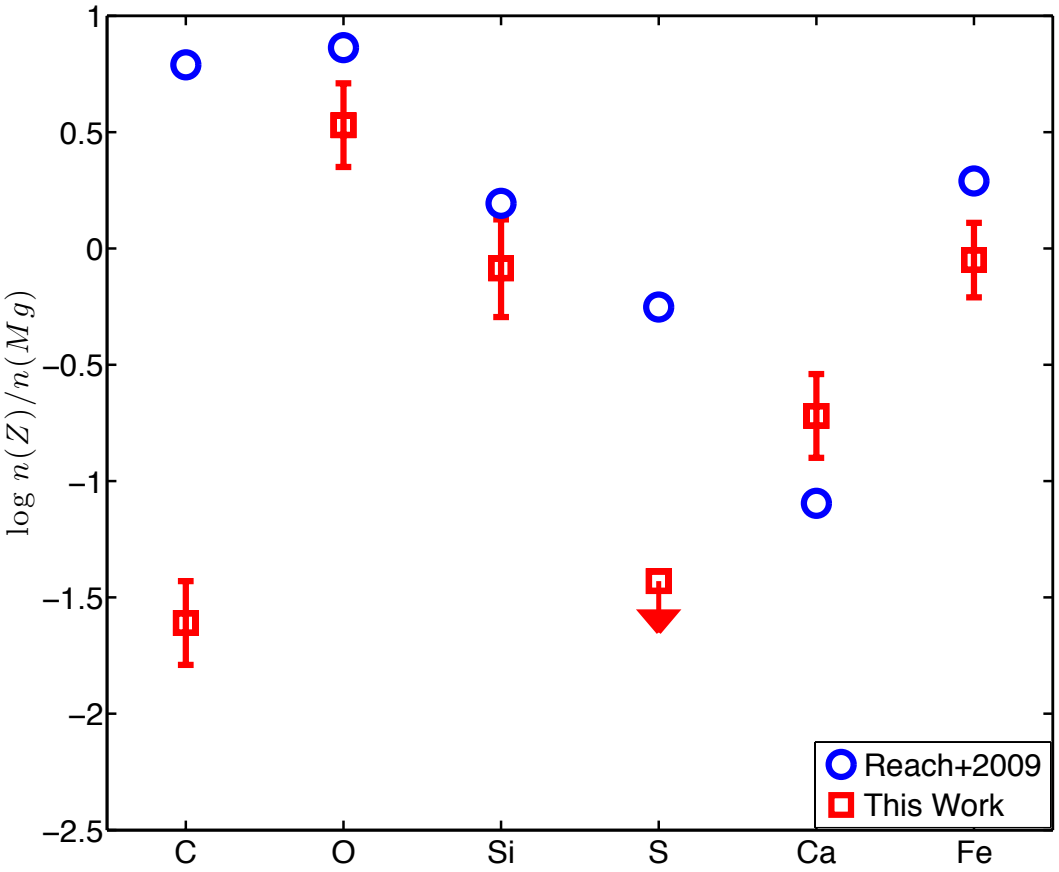

Figure 4.13 A comparison between the composition of the extrasolar planetesimal accreted onto G29-38 derived from atmospheric analysis (from Table 4.3, this work) and fitting the infrared spectrum of the dust disk (Reach et al., 2005, 2009). The atoms are arranged with increasing atomic weight. The ordinate represents the logarithmic value of the number ratios between an element and magnesium, one of the dominant elements. One sigma error bars are plotted. The overall agreement is respectable except for the carbon and sulfur abundances; see section 5.2 for details.

To find the best solar system analog to the composition of the parent body accreted onto G29-38, we follow Xu et al. (2013a) and perform a reduced chi-squared analysis with different types of meteorites. We consider 10 elements in total, including C, O, Mg, Si, S, Ca, Ti, Cr, Fe and Ni. We assigned the uncertainty in number ratios for S and Ni to be 0.17 dex, the biggest uncertainty from elements with a detection in G29-38. Therefore, these

two elements contribute to the reduced chi-squared value but with relatively low weight. As shown in Figure 4.14, several single meteorites fall within the 95% confidence level, including bulk Earth, CR chondrites, primitive achondrites and mesosiderites, a type of stoney-iron meteorites. Mesosiderites are a less promising candidate because the mass fraction of one of the major elements, Mg is 0.3 dex less in mesosiderite than in G29-38.

A detailed comparison of all the elements scaled to CI chondrites, the most primitive material in the solar system, is shown in Figure 4.15. We see that the mass fraction of volatile elements, such as carbon and sulfur, are depleted by at least a factor of 9 while the refractory elements, including calcium and titanium, are enhanced. The composition of the best-match solar system object – bulk Earth – is also plotted for comparison. The largest discrepancies between the compositions of the object accreted onto G29-38 and bulk Earth are Ca and Ti, two refractory elements.

When considering a blend of two meteorites, several combinations can all provide a good fit to the composition observed in G29-38. One example includes 60% H chondrite and 40% howardite, as shown in Figures 4.14 and 4.15. In general, some refractory-enhanced achondrites, such as howardites or mesosiderites, are required to reproduce the refractory abundance and chondritic material is needed to adjust the overall abundance pattern. Though the exact mechanism is not known, it is clear that the parent body accreted onto G29-38 has experienced post-nebular processing, such as differentiation and collision, which is found to be common for extrasolar planetesimals (Xu et al., 2013a).

G29-38 has accreted from an extrasolar planetesimal which is enhanced in both calcium and titanium, which is less frequently seen than enhancement of only calcium. In a sample of well studied polluted white dwarfs compiled in Jura & Young (2014), 6 out of 12 stars have [Ca/Mg] at least a factor of two higher than the value for CI chondrites; in comparison, only 3 out of 9 stars have a factor of two [Ca/Mg] and [Ti/Mg] enhancement, including PG 1225-079, GD 362 and G29-38. These three stars are the best candidates for accretion of a "normal" object and a refractory-dominated planetesimal (Jura & Xu, 2013). In addition, both G29-38 and GD 362 have well constrained stellar masses from parallax measurements (van Altena et al., 2001; Kilic et al., 2008b). Using the initial mass to final mass relationship (Williams

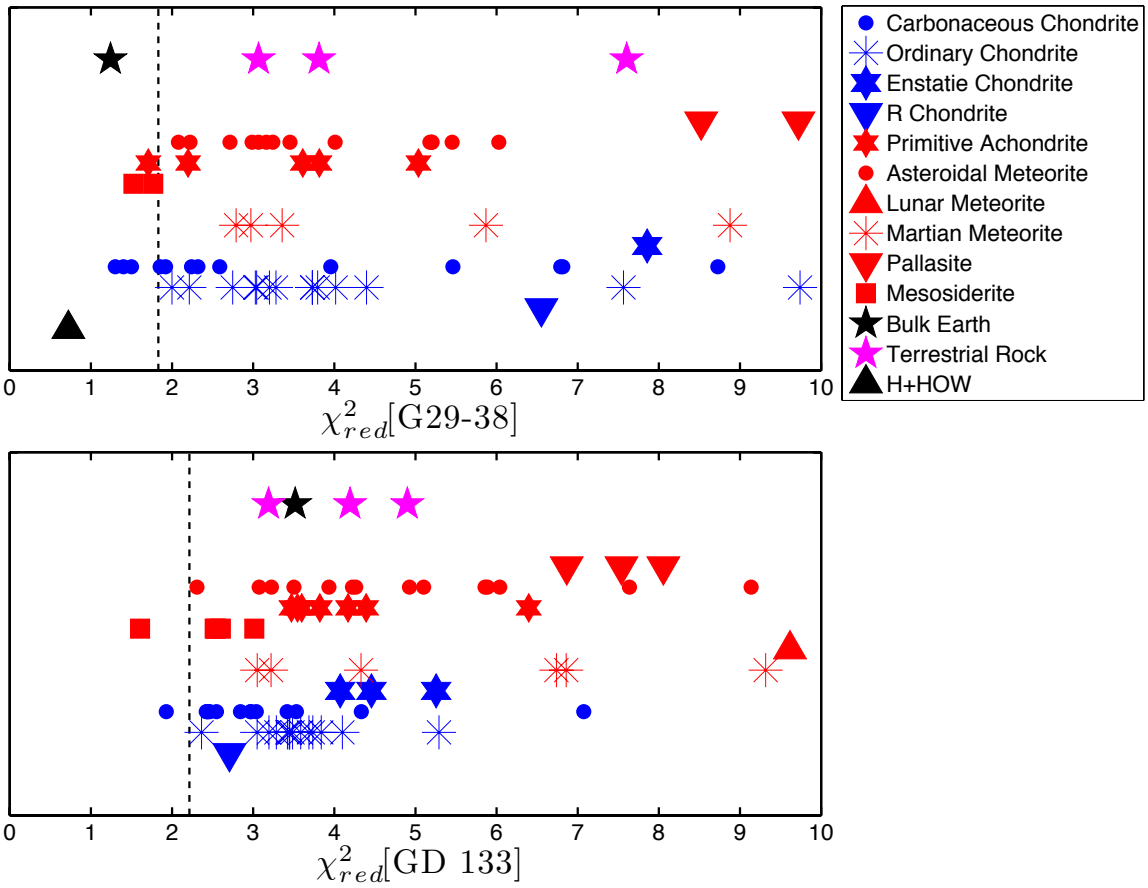

Figure 4.14 Computed reduced chi-squared values between the observed composition and meteorites. Different meteorite groups are offset in position in the ordinate for clarification. The upper panel is for G29-38 and lower panel for GD 133. For G29-38, we compare the mass fraction of 10 elements (C, O, Mg, Si, S, Ca, Ti, Cr, Fe and Ni) relative to the summed mass of O, Mg, Si and Fe; for GD 133, 5 elements (C, O, Mg, Si and Ca) are considered relative to the summed mass of O, Mg and Si because only an upper limit is obtained for Fe. The dashed lines represent 95% confidence level. The black triangle represents one of the blends that can best match the abundances observed in G29-38; it consists of 60% H chondrite and 40% of howardite. The meteorite database is described in Xu et al. (2013a) with most data from Nittler et al. (2004) and some Martian meteorites data from McSween (1985). The carbon abundance in CR chondrites and lodranite is from Alexander et al. (2007) and Grady & Wright (2003), respectively. The bulk composition of Earth is from Allègre et al. (2001). Terrestrial rocks include data from continental crust, upper mantle and lower mantle (Anderson, 2007).

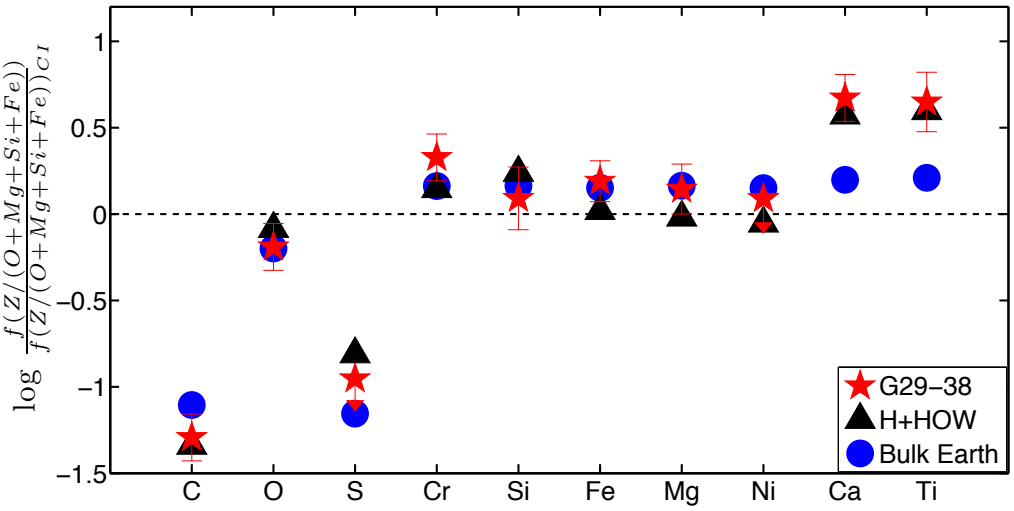

Figure 4.15 For G29-38, mass fraction of an element with respect to the sum of oxygen, magnesium, silicon and iron normalized to that of CI chondrites (Wasson & Kallemeyn, 1988). Arrows denotes upper limits. The elements are ordered by increasing condensation temperature. Also plotted is the best match single solar system object, bulk Earth as well as one of the best match when considering a blend – 60% H chondrite and 40% howadrite. Abundances for G29-38 are taken from Table 4.3.

et al., 2009), we derive a progenitor mass of 3.95$M_{\odot}$ and 2.95$M_{\odot}$ for G29-38 and GD 362, respectively, which are higher than the average white dwarf progenitor mass (Kleinman et al., 2013). Unfortunately, PG 1225-079 is in the stellar parameter region where temperature and surface gravity are coupled when using only the spectroscopic method (Klein et al., 2011). At least 2 out of the 3 stars that have accreted from refractory-dominated planetesimals have high progenitor mass; this is consistent with the model that refractory-dominated planetesimals are more likely to survive the red giant stage of stars with relatively high main-sequence masses (Jura & Xu, 2013).

As shown in Figure 4.15, the oxygen abundance in G29-38 is depleted by a factor of 1.5 compared to that in CI chondrites. The total amount of oxygen is barely enough to combine with all the heavy elements into the oxides; there might have been some metallic iron in the accreted planetesimal. No excess oxygen is left to be in the form of H_2O and water is very depleted in the planetesimal accreted onto G29-38.

Though Reach et al. (2009) derived a high water abundance, it is not supported by the

NIRSPEC data shown in Figure 4.1. No emission lines from water are detected. We see a gentle slope towards longer wavelength, which is consistent with the dust disk model, peaking longward of 4 μm. The IRAC 3.6 μm flux of G29-38 is $\sim$ 10% higher than predicted by the model and Farihi et al. (2008a) hypothesized contributions from some PAH features. A subsequent study by Reach et al. (2009) found that there is significant fluctuation at 3.6 μm with an amplitude of $\sim$ 5%, which could account for this discrepancy. Our NIRSPEC data also exclude any circumstellar emissions from PAH features as observed in Herbig Ae/Be stars (Meeus et al., 2001).

4.5.3 GD 133

For GD 133, we also performed a reduced chi-squared analysis for 5 heavy elements, including C, O, Mg, Si and Ca with an uncertainty of 0.2 dex for C and Mg. Their mass fractions are calculated with respect to the summed mass of O, Mg and Si, the most abundant three elements in GD 133. As shown in Figure 4.14, CR chondrites and mesosiderites match with the abundance pattern observed in GD 133.

A detailed comparison of the composition of the parent body accreted onto GD 133 and solar system objects is shown in Figure 4.16. Compared to CI chondrites, carbon is depleted by at least a factor of 20 in GD 133 while calcium is enhanced by a factor of 3. Magnesium is slightly depleted and [Mg/Ca] = 0.54, which is on the high side of all polluted white dwarfs (Jura & Xu, 2013). Mesosiderites give a better fit to the overall abundance pattern with the similar Ca enhancement and Mg depletion. Xu et al. (2013a) also found that mesosiderites is the best match to the abundance pattern in GD 362 due to the enhancements of Ca, Ti and Al. With constraints from only 5 elements in GD 133, it is hard to derive additional information. There exist several strong Fe II and Mg II lines around 2800 Å and they will provide much more information about the nature of the accreted material.

Until now, all dusty white dwarfs are heavily polluted with mass accretion rates of at least 1×10^8 g s^{-1} (Farihi et al., 2009; Brinkworth et al., 2012). GD 133 has a dust disk, which reprocesses about 0.5% of the incoming star light (Jura et al., 2007a; Farihi et al.,

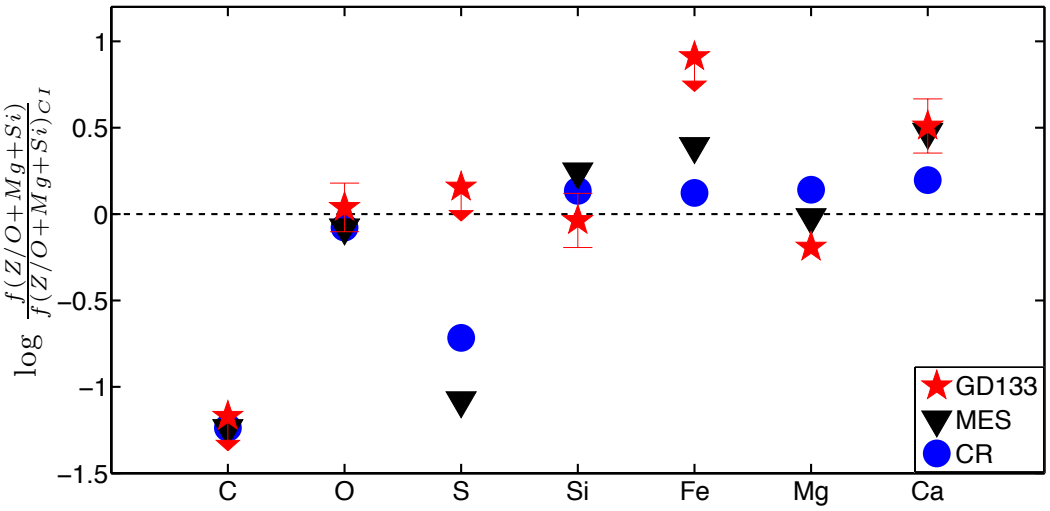

Figure 4.16 Similar to Figure 4.15 except for GD 133 and the mass fraction of an element normalized to the sum of oxygen, magnesium and silicon. There is no error bar associated with magnesium because it is only marginally detected. The compositions of two best match meteorites from the reduced chi-squared analysis, mesosiderite and CR chondrite, are also plotted for comparison.

2010b). Assuming a chondritic iron to silicon ratio, the accretion rate of iron is 5.9 × 10^6 g s^{-1} and the total accretion rate is 3.0 × 10^7 g s^{-1}, the lowest of all dusty white dwarfs. Even with an iron abundance of [Fe/H] = -5.90 (the upper limit listed in Table 4.3), the total accretion rate can only add up to 7.6 × 10^7 g s^{-1}, marginally lower than all other dusty white dwarfs. In a steady state model, Poynting-Robertson drag provides a lower bound of the accretion rate (Rafikov, 2011a; Xu & Jura, 2012):

$$\dot{M} = \frac{16\phi_r}{3}\frac{r_*^3}{r_{in}}\frac{\sigma T_{eff}^4}{c^2} \tag{4.1}$$

ϕ_r is an efficiency coefficient and taken as 1. σ and c are the Stephan-Boltzman constant and the speed of light, respectively. For GD 133, the stellar temperature T_{eff} is listed in Table 4.2 and the stellar radius r_*=0.012$r_\odot$. Depending on the disk inclination, the inner radius of the disk can vary (Jura et al., 2007a). To derive a lower limit of the mass accretion rate, we take the largest possible inner radius r_{in}=23r_* for a nearly face-on disk, and consequently $\dot{M}$ = 2.5 × 10^8 g s^{-1}, about an order of magnitude higher than the most likely inferred value.

The exceptionally low accretion rate in GD 133 provides direct evidence that equation (1) does not always hold, possibly because the accretion process onto the star is not always in a steady state.

There exists additional evidence for time-varying non-steady state accretion. Based on the different accretion rates derived from hydrogen and helium atmosphere white dwarfs, Farihi et al. (2012b) postulated a non-steady state accretion model including a high accretion stage and a low accretion stage. Now with an updated helium model atmosphere and settling times (Xu et al., 2013a), the difference has narrowed but is still present.

4.6 Perspective

So far, there are 10 white dwarfs that have detections of at least O, Mg, Si and Fe in the atmosphere. As presented in Figure 4.17, they are sampled from a variety of stellar temperatures and surface gravity. Five of these stars have a hydrogen-dominated atmosphere and five of them have a helium-dominated atmosphere. Eight stars also have a dust disk. Yet, to zeroth order, the resemblance of their elemental compositions relative to bulk Earth is robust. No carbon rich extrasolar planetesimals, e.g. analogs to comet Halley with 28% carbon (Jessberger et al., 1988) or interplanteary dust particle with $\sim$ 10% carbon (Thomas et al., 1993), are identified in the current sample. The only white dwarf that has accreted objects with a considerable amount of water is GD 61 (# 6 in the plot), which contains 26 % water by mass (Farihi et al., 2013). The general properties of extrasolar planetesimals can be summarized as the following (Jura & Young, 2014), (i) Oxygen, iron, silicon and magnesium always dominate and make up more than 85% of the total mass; (ii) carbon is always depleted relative to the solar abundance; (iii) viewed as an ensemble, water is less than 1% of the total accreted mass but exceptions exist. As shown in Figure 4.17, there are variations among the abundances of different elements but they are only a factor of 2-3, comparable to the errors. To move beyond a zeroth order result, one must determine abundances of as many trace elements as possible, such as the case of GD 362 (Zuckerman et al., 2007; Xu et al., 2013a). Alternatively, one can assess the abundances of a few elements

in an ensemble of stars, e.g. Jura & Xu (2012, 2013).

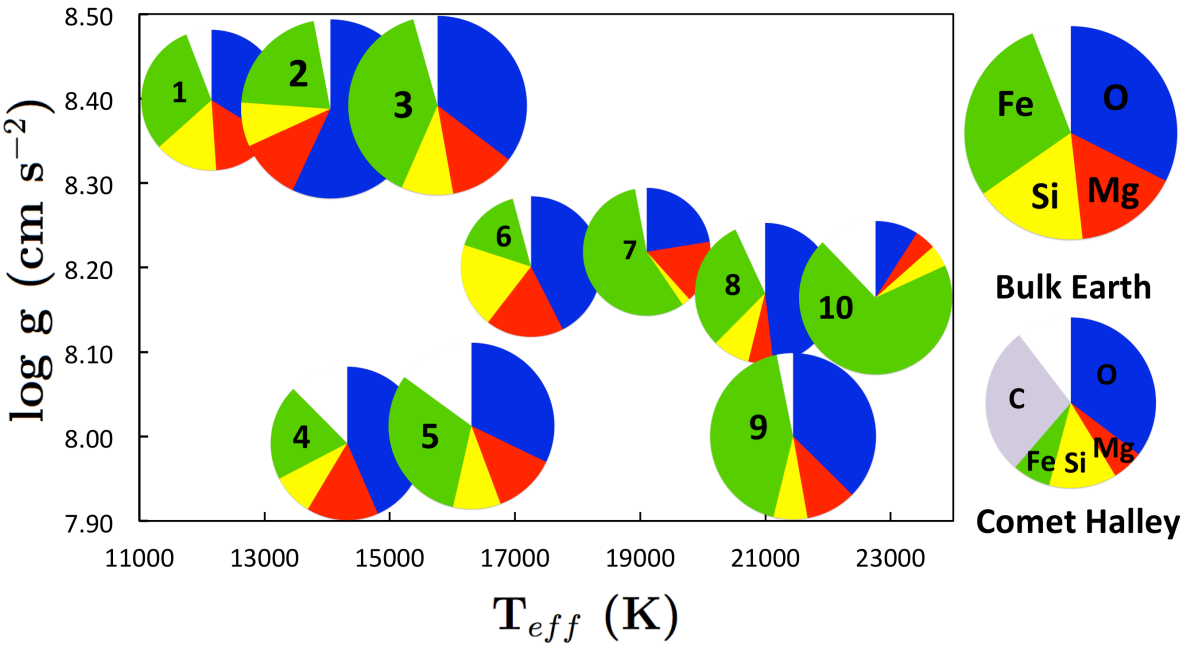

Figure 4.17 A compilation of all polluted white dwarfs with detections of at least O, Mg, Si and Fe; 8 of these stars also have good constraints on the carbon abundance. The abscissa marks white dwarf effective temperatures, corresponding to a cooling age less than 500 Myr; the ordinate is surface gravity, which shows a main sequence mass between 1.8-4.0 $M_{\odot}$ for the current sample. For clarity, some objects are slightly offset in their plotted positions. The abundances have been corrected for the effect of settling and we only show the mass fraction of O, Mg, Si and Fe; the rest are left blank. The size of a pie correlates with the accretion rate (not to scale). We see that O, Mg, Si and Fe are always the dominant elements in a variety of extrasolar planetesimals, resembling bulk Earth. No carbon rich planetesimals similar to comet Halley have been identified so far. The white dwarfs are ordered with increasing stellar temperatures. References: Hydrogen dominated white dwarfs: 1: G29-38 (this paper), 7: PG 1015+161, 8: WD 1226+110, 9: WD 1929+012, 10: WD 0843+516 (Gänsicke et al., 2012); helium dominated white dwarfs: 2: WD J0738+1835 (Dufour et al., 2012), 3: HS 2253+8023 (Klein et al., 2011), 4: G241-6, 5: GD 40 (Jura et al., 2012), 6: GD 61 (Farihi et al., 2011, 2013). All white dwarfs except # 3 and 4 have a dust disk. Bulk Earth: Allègre et al. (2001). Comet Halley: Jessberger et al. (1988)

4.7 Conclusions

In this paper, we report optical and ultraviolet spectroscopic studies of two externally-polluted hydrogen dominated white dwarfs, G29-38 and GD 133. For G29-38, with the

exception of carbon and sulfur, the derived elemental abundances agree reasonably well with the values obtained from fitting the infrared spectrum of the dust disk. Both stars have accreted objects that show a pattern of volatile depletion and refractory enhancement. The parent body accreted onto G29-38 has experienced post-nebular processing and can be best explained by a blend of chrondritic material and a refractory-enhanced object. The total mass accretion rate in GD 133 is significantly lower than all other dusty white dwarfs, suggesting non-steady state accretion. In a sample of ten stars, we find that the elemental compositions of extrasolar planetesimals are similar to bulk Earth regardless of their evolutionary history.

CHAPTER 5

Discovery of Molecular Hydrogen in White Dwarf Atmospheres

Reproduced by permission of the AAS (Xu, S., Jura, M., Koester, D., Klein, B., & Zuckerman, B., 2013, Astrophysical Journal Letters, 766, L18).

5.1 Introduction

An important discovery from the International Ultraviolet Explorer (IUE) was two broad absorption features at 1400 Å and 1600 Å in hydrogen-dominated (DA) white dwarfs cooler than 20,000 K and 13,500 K, respectively (Greenstein & Oke, 1979; Wegner, 1982). Subsequently, these features were explained by Koester et al. (1985) and Nelan & Wegner (1985) as Ly α satellite lines from collisions among H-H (1600 Å) and H-H^+ (1400 Å). These quasi-molecular absorption lines help to constrain stellar temperature and surface gravity for DA white dwarfs (Allard & Koester, 1992). G29-38, GD 133 and GD 31, the targets described in this letter, all show these quasi-molecular absorption features when observed with the IUE [Holm et al. (1985); Kepler & Nelan (1993), IUE archive]. Here, we report first detections of true molecular hydrogen in these three white dwarfs, by employing the Cosmic Origins Spectrograph (COS) on the Hubble Space Telescope (HST). These three stellar atmospheres are among the hottest stellar environments where photospheric molecular hydrogen has ever been detected.

5.2 Data

G29-38 and GD 133 were observed as part of program 12290 during HST cycle 18, which focuses on using externally polluted white dwarfs to assess the volatile abundances of accreted extrasolar planetesimals [see Jura (2003); Zuckerman et al. (2007); Klein et al. (2010); Dufour et al. (2012); Jura et al. (2012); Gänsicke et al. (2012) and references within]. G29-38 and GD 133 were chosen because they show a high degree of atmospheric pollution from optical studies (Koester et al., 1997, 2005b) and display excess infrared radiation (Zuckerman & Becklin, 1987; Reach et al., 2005, 2009; Jura et al., 2007a). As part of our program to study Hyades white dwarfs (Zuckerman et al., 2013), ultraviolet data for GD 31 were retrieved from the HST archive of the SNAPSHOT program 12169 (PI: B. Gänsicke).

For G29-38 and GD 133, the COS set-up was similar to that employed for GD 40 and G241-6, as previously reported in Jura et al. (2012). The G130M grating was used with central wavelength 1300 Å and wavelength coverage of 1142 -1288 Å (strip B) and 1298 -1443 Å (strip A). The spectral resolution was $\sim$ 20,000. Total exposure times, from combining 4 separate exposures for G29-38 and 5 for GD 133, were 9032 sec and 13,460 sec, respectively. The signal-to-noise ratio is at least 8 for strip B and 15 for strip A for both stars. The raw data were processed under the pipeline CALCOS 2.18.5. Because G29-38 is a ZZ Ceti star with multiple pulsation modes (Thompson et al., 2008), which lead to considerable changes in flux levels and continuum shape in each individual exposure, CALCOS processing cannot fully correct for these factors. Instead, we fitted the continuum of each CALCOS-extracted spectrum with a low-order spline3 polynomial and combined the normalized spectra with IRAF. We did not find any noticeable differences in line strength in each exposure. GD 133 is also a ZZ Ceti but the pulsation amplitude is much lower (Silvotti et al., 2006) and we simply adopt the pipeline reduced spectra. For GD 31, the G130M configuration has a central wavelength of 1291 Å, as described in Gänsicke et al. (2012). The total exposure time was 1200 sec and the signal-to-noise ratio is $\sim$ 7 for strip A. We also used the output from the CALCOS pipeline for GD 31.

Apart from the absorption lines from heavy elements in G29-38 and GD 133, which will

be discussed in Xu et al. (2013b), we see numerous quasi-periodic features, as illustrated in Figure 1. They are ubiquitous between 1310 Å and 1443 Å, almost the entire strip A. Clearly, these features are real and not instrumental artifacts, such as fixed pattern noise, for the following reasons. Unlike GD 40 and G241-6 (Jura et al., 2012), two other white dwarfs observed in the same program with the same instrumental set-up, these features were only present in the spectra of G29-38 and GD 133. Furthermore, they are at the same wavelength in each separate exposure. Although initially puzzled, after comparing with the ultraviolet spectrum of the Sun (Sandlin et al., 1986), we realized the absorption wavelengths exactly match those of molecular hydrogen. All the recognizable features correspond to Lyman band transitions from ν''= 2, 3, 4, 5 to ν' = 0 and Werner band transitions from ν''=2, 3 to ν' = 0 (Abgrall et al., 1993a,b). It turns out that we have accidentally found H_2 in white dwarf atmospheres! We present the strongest Lyman band H_2 lines in Table 5.1; they are all appreciably stronger than the Werner bands in our observed wavelength interval.

We serendipitously identified molecular hydrogen in a third star, GD 31, which may be a high-mass escaping member of the Hyades cluster (Zuckerman et al., 2013). The data are noisier but clearly four absorption features are seen; these correspond to the strongest H_2 Lyman band lines and their blends in G29-38, at the correct wavelengths, as presented in Table 5.1 and Figure 5.1.

5.3 Discussion

According to the Saha equation, molecular hydrogen is most concentrated in low temperature, high density environments. Previously, ro-vibrational lines from H_2 have been detected in cool stellar atmospheres in the infrared (Spinrad, 1964) and in the Sun's ultraviolet emission spectrum (Jordan et al., 1978; Sandlin et al., 1986). Our ultraviolet detection of photospheric H_2 introduces a new aspect to stellar physics. With stellar parameters of T_* = 11,820 K, log g=8.40 for G29-38 (Xu et al., 2013b) and T_*=12,121 K, log g = 8.005 for GD 133 (Koester et al., 2009), we computed white dwarf model atmospheres (Koester, 2010) and calculated the number density of molecular hydrogen relative to atomic hydrogen,

Table 5.1 The Strongest Identified Lyman Band H_2 Lines

λ (cm^{-1})[a]	λ (Å)	Transition[b]	G29-38 EW (mÅ)	GD 133 EW (mÅ)	GD 31 EW (mÅ)
74344.49	1345.1	0-4 R(5)	170[c]	107[c]	87[c]
74339.87	1345.2	0-3 P(11)	170[c]	107[c]	87[c]
73936.94	1352.5	0-4 P(5)	76	66	...
73719.80	1356.5	0-4 R(7)	121[c]	103[c]	63[c]
73714.96	1356.6	0-3 P(12)	121[c]	103[c]	63[c]
73185.32	1366.4	0-4 P(7)	180	70	59
73064.05	1368.7	0-3 P(13)	45	35	35
71225.99	1404.0	0-4 P(11)	76	45	...
71187.04	1404.8	0-5 R(5)	97	83	...
70992.76	1408.6	0-3 P(16)	112[c]	90[c]	...
70889.48	1410.6	0-4 R(13)	112[c]	90[c]	...
70076.46	1427.0	0-4 P(13)	75	53	...

[a] From Abgrall et al. (1993a).
[b] We follow the notational conventions in Meyer et al. (2001).
[c] This line is blended and the reported number is the total EW for both lines together.
Note. For G29-38 and GD 133, the EW uncertainty is dominated by the choice of continuum interval because the whole region shows numerous H_2 lines and there is no clean continuum as shown in Figure 5.1. Typically, the EW uncertainty is within 10%. For GD 31, the data are much noisier and the EW uncertainty is typically 25 %.

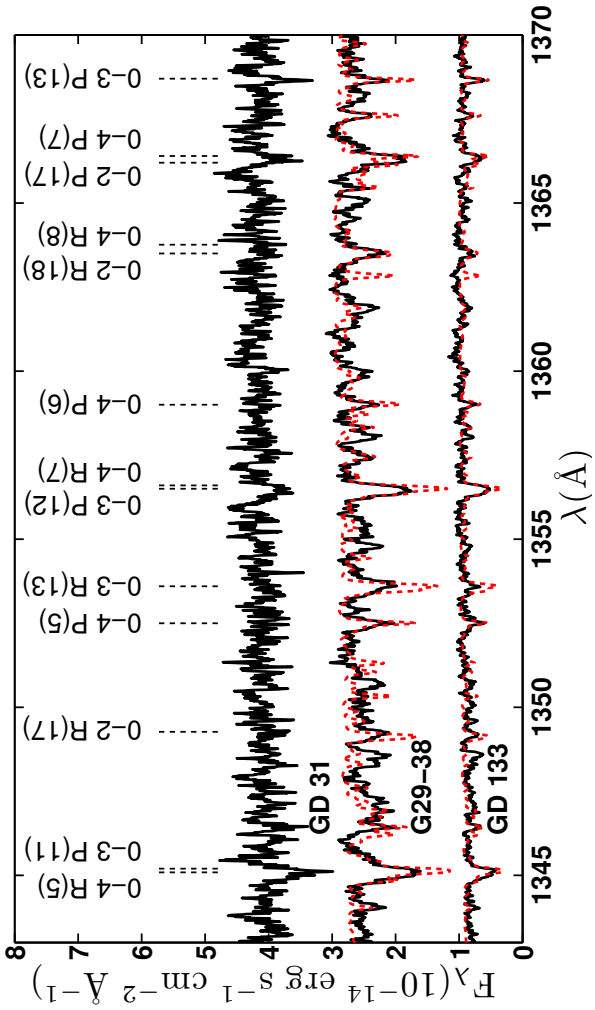

Figure 5.1 Portion of the Lyman band absorptions of molecular hydrogen in G29-38, GD 133 and GD 31 at the red wing of the H-H$^+$ quasi-molecular feature. The spectra are smoothed with a 5 point boxcar and shifted by 39 km s^{-1}, 58 km s^{-1} and 89 km s^{-1} for G29-38, GD 133 and GD 31 respectively, to be in the heliocentric reference frame (Xu et al., 2013b; Zuckerman et al., 2013). For clarity, the spectrum for GD 133 is offset by 0.5 $\times$ 10^{-14} erg s^{-1} cm^{-2} Å^{-1} and for GD 31 by 1.5 $\times$ 10^{-14} erg s^{-1} cm^{-2} Å^{-1}. The red dashed lines are our computed model spectra. Statistically, the models reproduce the data but the fit to individual lines is not ideal. For G29-38 and GD 133, the entire spectrum in strip A (1298-1443 Å) shows numerous ro-vibrational lines of H_2. The strongest absorption features around 1345 Å, 1357 Å, 1366 Å and 1369 Å are also seen in GD 31.

$n(H_2)/n(H)$, as shown in Figure 5.1. At maximum, molecular hydrogen is still $10^{-4.7}$ and $10^{-5.1}$ less than the amount of atomic hydrogen in G29-38 and GD 133, respectively. These computed ratios are comparable to, but at the higher end of the concentration of trace elements in heavily polluted white dwarfs (Jura et al., 2012). Because molecular hydrogen is distributed over a large number of ro-vibrational levels, each individual line is relatively weak. As discussed in Zuckerman et al. (2013), H_2 is used to resolve a major temperature puzzle for GD 31. Due to its high gravity, the equivalent widths (EWs) of 4 detected H_2 lines in GD 31 (T=13,700 K, log g=8.67) are comparable to those in GD 133; there is a substantial amount of molecular hydrogen in the atmosphere of GD 31.

As shown in Figure 1, we computed the model spectra for G29-38 and GD 133 following Koester (2010) with all the line data obtained from the Kurucz webpage[1] (Kurucz, 1995) and the H_2 partition function from Irwin (1981). In a statistical sense, the model well represents the data and reproduces most molecular hydrogen features. However, the fit to individual lines is rather poor due to the lack of accurate broadening parameters. The Z Astrophysical Plasma Properties (ZAPP) Collaboration is actively involved in creating white dwarf photospheres in the lab and determining line broadening parameters (Falcon et al., 2012). Our understanding of the COS ultraviolet observations can be substantially improved with accurate physical parameters for the H_2 lines.

Another aspect of this discovery is that by constraining the abundance of the HD molecule, we can place a limit on the D/H ratio. It is generally believed that all deuterium is primordial from the Big Bang nucleosynthesis and destroyed in stellar interiors (Epstein et al., 1976). Any amount, if present, in the white dwarf atmosphere must come from some external source, likely relic planetesimals. The values are not very constraining for the targets presented here. But if cooler stars can be observed with COS with a sufficiently high signal-to-noise ratio, then more meaningful upper limits or actual detections of the HD molecule in white dwarf atmospheres may be anticipated.

In white dwarfs cooler than 12,000 K, H_2 is present but usually there is not enough ultraviolet flux to make observations in a time-efficient manner. The environment in hotter

[1] http://kurucz.harvard.edu/linelists.html

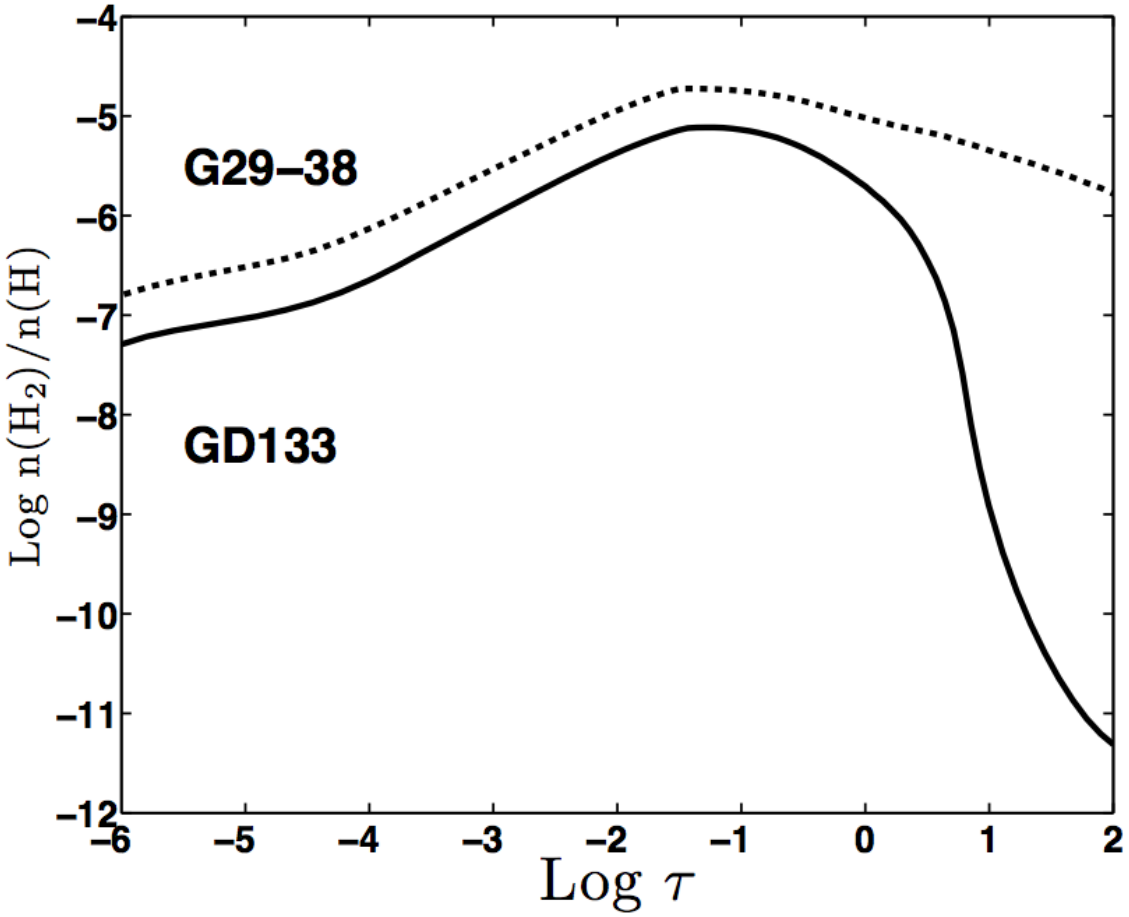

Figure 5.2 Ratio of number densities of molecular hydrogen compared to atomic hydrogen at different optical depths in G29-38 and GD 133. For G29-38, this ratio peaks at log $n(H_2)/n(H)$ = -4.7, where τ = 0.04, T = 9900 K and $\rho = 3.1 \times 10^{-7}$ g cm^{-3}. For GD 133, the maximum of log $n(H_2)/n(H)$ is -5.1, which occurs at τ = 0.05, T=10,200 K and $\rho = 1.5 \times 10^{-7}$ g cm^{-3}.

stars is typically more hostile for molecular hydrogen but high pressure may still enable detection of H_2.

5.4 Conclusions

With the HST, molecular hydrogen was detected for the first time in white dwarf atmospheres. The three stars, G29-38, GD 133 and GD 31, have temperatures between 11,800 K and 13,700 K. H_2 can be used as an independent constraint to white dwarf atmospheric conditions. This opens a door to many future explorations.

Bibliography

Abgrall, H., Roueff, E., Launay, F., Roncin, J. Y., & Subtil, J. L. 1993a, A&AS, 101, 273

—. 1993b, A&AS, 101, 323

Alexander, C. M. O. ., Fogel, M., Yabuta, H., & Cody, G. D. 2007, , 71, 4380

Allard, N. F. & Koester, D. 1992, A&A, 258, 464

Allègre, C., Manhès, G., & Lewin, E. 2001, Earth and Planetary Science Letters, 185, 49

Anderson, D. 2007, New Theory of the Earth (Cambridge: Cambridge Univ. Press)

Barber, S. D., Patterson, A. J., Kilic, M., Leggett, S. K., Dufour, P., Bloom, J. S., & Starr, D. L. 2012, ApJ, 760, 26

Becklin, E. E., Farihi, J., Jura, M., Song, I., Weinberger, A. J., & Zuckerman, B. 2005, ApJL, 632, L119

Benz, W., Slattery, W. L., & Cameron, A. G. W. 1988, Icarus, 74, 516

Bergeron, P., Wesemael, F., Dufour, P., & et al. 2011, ApJ, 737, 28

Bohlin, R. C., Gordon, K. D., Rieke, G. H., & et al. 2011, AJ, 141, 173

Bonsor, A., Mustill, A. J., & Wyatt, M. C. 2011, MNRAS, 414, 930

Bonsor, A. & Wyatt, M. 2010, MNRAS, 409, 1631

Brinkworth, C. S., Gänsicke, B. T., Girven, J. M., Hoard, D. W., Marsh, T. R., Parsons, S. G., & Koester, D. 2012, ApJ, 750, 86

Brinkworth, C. S., Gänsicke, B. T., Marsh, T. R., Hoard, D. W., & Tappert, C. 2009, ApJ, 696, 1402

Carr, J. S. & Najita, J. R. 2008, Science, 319, 1504

Chen, Y.-H. & Li, Y. 2013, ArXiv e-prints

Chu, Y., Gruendl, R. A., Bilíkovà, J., Riddle, A., & Su, K. 2010, ArXiv e-prints

Chu, Y.-H., Su, K. Y. L., Bilikova, J., Gruendl, R. A., De Marco, O., Guerrero, M. A., Updike, A. C., Volk, K., & Rauch, T. 2011, ArXiv e-prints

Chyba, C. F. 1990, Nature, 343, 129

Deal, M., Deheuvels, S., Vauclair, G., Vauclair, S., & Wachlin, F. C. 2013, A&A, 557, L12

Debes, J. H., Hoard, D. W., Kilic, M., Wachter, S., Leisawitz, D. T., Cohen, M., Kirkpatrick, J. D., & Griffith, R. L. 2011, ApJ, 729, 4

Debes, J. H., Kilic, M., Faedi, F., Shkolnik, E. L., Lopez-Morales, M., Weinberger, A. J., Slesnick, C., & West, R. G. 2012a, ApJ, 754, 59

Debes, J. H. & López-Morales, M. 2008, ApJL, 677, L43

Debes, J. H. & Sigurdsson, S. 2002, ApJ, 572, 556

Debes, J. H., Walsh, K. J., & Stark, C. 2012b, ApJ, 747, 148

Desharnais, S., Wesemael, F., Chayer, P., Kruk, J. W., & Saffer, R. A. 2008, ApJ, 672, 540

Dong, R., Wang, Y., Lin, D. N. C., & Liu, X.-W. 2010, ApJ, 715, 1036

Drahus, M., Jewitt, D., Guilbert-Lepoutre, A., Waniak, W., Hoge, J., Lis, D. C., Yoshida, H., Peng, R., & Sievers, A. 2011, ApJL, 734, L4+

Dufour, P., Bergeron, P., Liebert, J., Harris, H. C., Knapp, G. R., Anderson, S. F., Hall, P. B., Strauss, M. A., Collinge, M. J., & Edwards, M. C. 2007, ApJ, 663, 1291

Dufour, P., Bergeron, P., Schmidt, G. D., Liebert, J., Harris, H. C., Knapp, G. R., Anderson, S. F., & Schneider, D. P. 2006, ApJ, 651, 1112

Dufour, P., Kilic, M., Fontaine, G., Bergeron, P., Lachapelle, F., Kleinman, S. J., & Leggett, S. K. 2010, ApJ, 719, 803

Dufour, P., Kilic, M., Fontaine, G., Bergeron, P., Melis, C., & Bochanski, J. 2012, ApJ, 749, 6

Dupuis, J., Fontaine, G., Pelletier, C., & Wesemael, F. 1993, ApJS, 84, 73

Eisenstein, D. J., Liebert, J., Harris, H. C., & et al. 2006, ApJS, 167, 40

Epstein, R. I., Lattimer, J. M., & Schramm, D. N. 1976, Nature, 263, 198

Falcon, R. E., Rochau, G. A., Bailey, J. E., Ellis, J. L., Carlson, A. L., Gomez, T. A., Montgomery, M. H., Winget, D. E., Chen, E. Y., Gomez, M. R., & Nash, T. J. 2012, ArXiv e-prints

Farihi, J., Barstow, M. A., Redfield, S., Dufour, P., & Hambly, N. C. 2010a, MNRAS, 404, 2123

Farihi, J., Becklin, E. E., & Zuckerman, B. 2005, ApJS, 161, 394

—. 2008a, ApJ, 681, 1470

Farihi, J., Brinkworth, C. S., Gänsicke, B. T., Marsh, T. R., Girven, J., Hoard, D. W., Klein, B., & Koester, D. 2011, ApJL, 728, L8

Farihi, J., Gänsicke, B. T., & Koester, D. 2013, ArXiv e-prints

Farihi, J., Gänsicke, B. T., Steele, P. R., Girven, J., Burleigh, M. R., Breedt, E., & Koester, D. 2012a, MNRAS, 421, 1635

Farihi, J., Gänsicke, B. T., Wyatt, M. C., Girven, J., Pringle, J. E., & King, A. R. 2012b, MNRAS, 424, 464

Farihi, J., Jura, M., Lee, J., & Zuckerman, B. 2010b, ApJ, 714, 1386

Farihi, J., Jura, M., & Zuckerman, B. 2009, ApJ, 694, 805

Farihi, J., Zuckerman, B., & Becklin, E. E. 2008b, ApJ, 674, 431

Fazio et al. 2004, ApJS, 154, 10

Gänsicke, B. T. 2011, in American Institute of Physics Conference Series, Vol. 1331, American Institute of Physics Conference Series, ed. S. Schuh, H. Drechsel, & U. Heber, 211–214

Gänsicke, B. T., Koester, D., Farihi, J., Girven, J., Parsons, S. G., & Breedt, E. 2012, MNRAS, 424, 333

Gänsicke, B. T., Koester, D., Marsh, T. R., Rebassa-Mansergas, A., & Southworth, J. 2008, MNRAS, 391, L103

Gänsicke, B. T., Marsh, T. R., & Southworth, J. 2007, MNRAS, 380, L35

Gänsicke, B. T., Marsh, T. R., Southworth, J., & Rebassa-Mansergas, A. 2006, Science, 314, 1908

Giammichele, N., Bergeron, P., & Dufour, P. 2012, ApJS, 199, 29

Gianninas, A., Bergeron, P., & Ruiz, M. T. 2011, ApJ, 743, 138

Girven, J., Brinkworth, C. S., Farihi, J., Gänsicke, B. T., Hoard, D. W., Marsh, T. R., & Koester, D. 2012, ApJ, 749, 154

Girven, J., Gänsicke, B. T., Steeghs, D., & Koester, D. 2011, MNRAS, 417, 1210

Goodrich, C. A. 1992, Meteoritics, 27, 327

Grady, M. M. & Wright, I. P. 2003, , 106, 231

Greenstein, J. L. & Oke, J. B. 1979, ApJL, 229, L141

Hoard, D. W., Wachter, S., Sturch, L. K., & et al. 2007, AJ, 134, 26

Holberg, J. B. & Bergeron, P. 2006, AJ, 132, 1221

Holberg, J. B., Bergeron, P., & Gianninas, A. 2008, AJ, 135, 1239

Holm, A. V., Panek, R. J., Schiffer, III, F. H., Bond, H. E., Kemper, E., & Grauer, A. D. 1985, ApJ, 289, 774

Hummer, D. G. & Mihalas, D. 1988, ApJ, 331, 794

Irwin, A. W. 1981, ApJS, 45, 621

Jessberger, E. K., Christoforidis, A., & Kissel, J. 1988, Nature, 332, 691

Jordan, C., Brueckner, G. E., Bartoe, J.-D. F., Sandlin, G. D., & Vanhoosier, M. E. 1978, ApJ, 226, 687

Jura, M. 2003, ApJL, 584, L91

—. 2008, AJ, 135, 1785

—. 2013, ArXiv e-prints

Jura, M., Farihi, J., & Zuckerman, B. 2007a, ApJ, 663, 1285

—. 2009a, AJ, 137, 3191

Jura, M., Farihi, J., Zuckerman, B., & Becklin, E. E. 2007b, AJ, 133, 1927

Jura, M., Muno, M. P., Farihi, J., & Zuckerman, B. 2009b, ApJ, 699, 1473

Jura, M. & Xu, S. 2010, AJ, 140, 1129

—. 2012, AJ, 143, 6

—. 2013, AJ, 145, 30

Jura, M., Xu, S., Klein, B., Koester, D., & Zuckerman, B. 2012, ApJ, 750, 69

Jura, M. & Young, E. D. 2014, Ann. Rev. Earth Planet. Sci. in press, 42

Kelleher, D. & Podobedova, L. 2008, JPCRD, 37, 267

Kepler, S. O. & Nelan, E. P. 1993, AJ, 105, 608

Kilic, M., Farihi, J., Nitta, A., & Leggett, S. K. 2008a, AJ, 136, 111

Kilic, M., Kowalski, P. M., Reach, W. T., & von Hippel, T. 2009, ApJ, 696, 2094

Kilic, M., Thorstensen, J. R., & Koester, D. 2008b, ApJL, 689, L45

Kilic, M., von Hippel, T., Leggett, S. K., & Winget, D. E. 2005, ApJL, 632, L115

—. 2006, ApJ, 646, 474

Klein, B., Jura, M., Koester, D., & Zuckerman, B. 2011, ApJ, 741, 64

Klein, B., Jura, M., Koester, D., Zuckerman, B., & Melis, C. 2010, ApJ, 709, 950

Kleinman, S. J., Kepler, S. O., Koester, D., & et al. 2013, ApJS, 204, 5

Koester, D. 2009, A&A, 498, 517

—. 2010, , 81, 921

Koester, D., Gänsicke, B., Girven, J., & Farihi, J. 2012, ArXiv e-prints 1206:6036

Koester, D., Girven, J., Gänsicke, B. T., & Dufour, P. 2011, A&A, 530, A114+

Koester, D. & Kompa, E. 2007, A&A, 473, 239

Koester, D., Provencal, J., & Shipman, H. L. 1997, A&A, 320, L57

Koester, D., Rollenhagen, K., Napiwotzki, R., Voss, B., Christlieb, N., Homeier, D., & Reimers, D. 2005a, A&A, 432, 1025

—. 2005b, A&A, 432, 1025

Koester, D., Voss, B., Napiwotzki, R., Christlieb, N., Homeier, D., Lisker, T., Reimers, D., & Heber, U. 2009, A&A, 505, 441

Koester, D., Weidemann, V., Zeidler-K.T., E. M., & Vauclair, G. 1985, A&A, 142, L5

Koester, D. & Wilken, D. 2006, A&A, 453, 1051

Krasinsky, G. A., Pitjeva, E. V., Vasilyev, M. V., & Yagudina, E. I. 2002, Icarus, 158, 98

Kriss, G. A. 2011, Improved Medium Resolution Line Spread Functions for COS FUV Spectra, Tech. rep.

Kupka, F., Piskunov, N., Ryabchikova, T. A., Stempels, H. C., & Weiss, W. W. 1999, A&AS, 138, 119

Kurucz, R. L. 1995, in Astronomical Society of the Pacific Conference Series, Vol. 78, Astrophysical Applications of Powerful New Databases, ed. S. J. Adelman & W. L. Wiese, 205

Larimer, J. W. 1988, Meteorites and the Early Solar System (University of Arizona Press), 19–52

Lehner, N., Jenkins, E. B., Gry, C., Moos, H. W., Chayer, P., & Lacour, S. 2003, ApJ, 595, 858

Liebert, J., Bergeron, P., & Holberg, J. B. 2005, ApJS, 156, 47

Lodders, K. 2003, ApJ, 591, 1220

Martin, D. C., Fanson, J., Schiminovich, D., & et al. 2005, ApJL, 619, L1

Marty, B. 2012, Earth and Planetary Science Letters, 313, 56

McLean, I. S., Becklin, E. E., Bendiksen, O., & et al. 1998, in Society of Photo-Optical Instrumentation Engineers (SPIE) Conference Series, ed. A. M. Fowler, Vol. 3354, 566–578

McLean, I. S., Graham, J. R., Becklin, E. E., Figer, D. F., & et al. 2000, in Society of Photo-Optical Instrumentation Engineers (SPIE) Conference Series, ed. M. Iye & A. F. Moorwood, Vol. 4008, 1048–1055

McLean, I. S., McGovern, M. R., Burgasser, A. J., Kirkpatrick, J. D., Prato, L., & Kim, S. S. 2003, ApJ, 596, 561

McSween, H. Y. 1985, Reviews of Geophysics, 23, 391

McSween, H. Y. & Huss, G. R. 2010, Cosmochemistry (Cambridge: Cambridge Univ. Press)

Meeus, G., Waters, L. B. F. M., Bouwman, J., van den Ancker, M. E., Waelkens, C., & Malfait, K. 2001, A&A, 365, 476

Melis, C., Dufour, P., Farihi, J., Bochanski, J., Burgasser, A. J., Parsons, S. G., Gänsicke, B. T., Koester, D., & Swift, B. J. 2012, ApJL, 751, L4

Melis, C., Farihi, J., Dufour, P., Zuckerman, B., Burgasser, A. J., Bergeron, P., Bochanski, J., & Simcoe, R. 2011, ApJ, 732, 90

Melis, C., Jura, M., Albert, L., Klein, B., & Zuckerman, B. 2010, ApJ, 722, 1078

Meyer, D. M., Lauroesch, J. T., Sofia, U. J., Draine, B. T., & Bertoldi, F. 2001, ApJL, 553, L59

Morlok, A., Koike, C., Tomeoka, K., Mason, A., Lisse, C., Anand, M., & Grady, M. 2012, Icarus, 219, 48

Morton, D. C. 1975, ApJ, 197, 85

Mullally, F., Kilic, M., Reach, W. T., Kuchner, M. J., von Hippel, T., Burrows, A., & Winget, D. E. 2007, ApJS, 171, 206

Nelan, E. P. & Wegner, G. 1985, ApJL, 289, L31

Nesvorný, D., Jenniskens, P., Levison, H. F., Bottke, W. F., Vokrouhlický, D., & Gounelle, M. 2010, ApJ, 713, 816

Nittler, L. R., McCoy, T. J., Clark, P. E., Murphy, M. E., Trombka, J. I., & Jarosewich, E. 2004, Antarctic Meteorite Research, 17, 231

O'Neill, H. S. C. & Palme, H. 2008, Royal Society of London Philosophical Transactions Series A, 366, 4205

Paquette, C., Pelletier, C., Fontaine, G., & Michaud, G. 1986, ApJS, 61, 197

Pelletier, C., Fontaine, G., Wesemael, F., Michaud, G., & Wegner, G. 1986, ApJ, 307, 242

Poglitsch, A., Waelkens, C., Geis, N., & et al. 2010, A&A, 518, L2

Rafikov, R. R. 2011a, ApJL, 732, L3+

—. 2011b, MNRAS, 416, L55

Reach, W. T., Lisse, C., von Hippel, T., & Mullally, F. 2009, ApJ, 693, 697

Reach, W. T., Megeath, S. T., Cohen, M., & et al. 2005, PASP, 117, 978

Redfield, S. & Linsky, J. L. 2008, ApJ, 673, 283

Reid, I. N., Liebert, J., & Schmidt, G. D. 2001, ApJL, 550, L61

Sandlin, G. D., Bartoe, J.-D. F., Brueckner, G. E., Tousey, R., & Vanhoosier, M. E. 1986, ApJS, 61, 801

Scott, E. R. D., Haack, H., & Love, S. G. 2001, Meteoritics and Planetary Science, 36, 869

Silvotti, R., Pavlov, M., Fontaine, G., Marsh, T., & Dhillon, V. 2006, , 77, 486

Spinrad, H. 1964, ApJ, 140, 1639

Steele, P. R., Burleigh, M. R., Dobbie, P. D., Jameson, R. F., Barstow, M. A., & Satterthwaite, R. P. 2011, MNRAS, 416, 2768

Thomas, K. L., Blanford, G. E., Keller, L. P., Klock, W., & McKay, D. S. 1993, , 57, 1551

Thompson, S. E., Montgomery, M. H., von Hippel, T., & et al. 2010, ApJ, 714, 296

Thompson, S. E., van Kerkwijk, M. H., & Clemens, J. C. 2008, MNRAS, 389, 93

Tokunaga, A. T., Becklin, E. E., & Zuckerman, B. 1990, ApJL, 358, L21

Tremblay, P.-E. & Bergeron, P. 2009, ApJ, 696, 1755

Tremblay, P.-E., Bergeron, P., Kalirai, J. S., & Gianninas, A. 2010, ApJ, 712, 1345

van Altena, W. F., Lee, J. T., & Hoffleit, E. D. 2001, VizieR Online Data Catalog, 1238, 0

Vauclair, S. & Théado, S. 2012, ApJ, 753, 49

Vennes, S., Kawka, A., & Németh, P. 2010, MNRAS, 404, L40

—. 2011, MNRAS, 413, 2545

Veras, D., Mustill, A. J., Bonsor, A., & Wyatt, M. C. 2013, MNRAS, 431, 1686

Vogt, S. S., Allen, S. L., Bigelow, B. C., & et al. 1994, in Society of Photo-Optical Instrumentation Engineers (SPIE) Conference Series, Vol. 2198, Society of Photo-Optical Instrumentation Engineers (SPIE) Conference Series, ed. D. L. Crawford & E. R. Craine, 362

von Hippel, T., Kuchner, M. J., Kilic, M., Mullally, F., & Reach, W. T. 2007, ApJ, 662, 544

von Hippel, T. & Thompson, S. E. 2007, ApJ, 661, 477

Voss, B., Koester, D., Napiwotzki, R., Christlieb, N., & Reimers, D. 2007, A&A, 470, 1079

Warren, P. H., Ulff-Møller, F., Huber, H., & Kallemeyn, G. W. 2006, , 70, 2104

Wasson, J. T. & Kallemeyn, G. W. 1988, Royal Society of London Philosophical Transactions Series A, 325, 535

Wegner, G. 1982, ApJL, 261, L87

Werner et al. 2004, ApJS, 154, 1

Williams, K. A., Bolte, M., & Koester, D. 2009, ApJ, 693, 355

Wolff, B., Koester, D., & Liebert, J. 2002, A&A, 385, 995

Xu, S. & Jura, M. 2012, ApJ, 745, 88

Xu, S., Jura, M., Klein, B., Koester, D., & Zuckerman, B. 2013a, ApJ, 766, 132

Xu, S., Jura, M., Koester, D., Klein, B., & Zuckerman, B. 2013b, ApJL, 766, L18

—. 2014, ApJ, 783, 79

Zacharias, N., Monet, D. G., Levine, S. E., Urban, S. E., Gaume, R., & Wycoff, G. L. 2005, VizieR Online Data Catalog, 1297, 0

Zuckerman, B. & Becklin, E. E. 1987, Nature, 330, 138

Zuckerman, B., Koester, D., Dufour, P., Melis, C., Klein, B., & Jura, M. 2011, ApJ, 739, 101

Zuckerman, B., Koester, D., Melis, C., Hansen, B. M., & Jura, M. 2007, ApJ, 671, 872

Zuckerman, B., Koester, D., Reid, I. N., & Hünsch, M. 2003, ApJ, 596, 477

Zuckerman, B., Melis, C., Klein, B., Koester, D., & Jura, M. 2010, ApJ, 722, 725

Zuckerman, B., Xu, S., Klein, B., & Jura, M. 2013, ApJ, 770, 140